



---

**Disposable, Autonomic, Energy-Converting Ion Channel Sensor Materials**

**David Sept**  
**UNIVERSITY OF MICHIGAN**

---

**02/07/2018**  
**Annual Report**

**DISTRIBUTION A: Distribution approved for public release.**

**Air Force Research Laboratory**  
**AF Office Of Scientific Research (AFOSR)/ RTB2**  
**Arlington, Virginia 22203**  
**Air Force Materiel Command**

DISTRIBUTION A: Distribution approved for public release.

<b>REPORT DOCUMENTATION PAGE</b>				<i>Form Approved</i> OMB No. 0704-0188	
<p>The public reporting burden for this collection of information is estimated to average 1 hour per response, including the time for reviewing instructions, searching existing data sources, gathering and maintaining the data needed, and completing and reviewing the collection of information. Send comments regarding this burden estimate or any other aspect of this collection of information, including suggestions for reducing the burden, to Department of Defense, Executive Services, Directorate (0704-0188). Respondents should be aware that notwithstanding any other provision of law, no person shall be subject to any penalty for failing to comply with a collection of information if it does not display a currently valid OMB control number.</p> <p>PLEASE DO NOT RETURN YOUR FORM TO THE ABOVE ORGANIZATION.</p>					
<b>1. REPORT DATE (DD-MM-YYYY)</b> 15-02-2018		<b>2. REPORT TYPE</b> Annual Report		<b>3. DATES COVERED (From - To)</b> 01 Sep 2012 to 31 Oct 2018	
<b>4. TITLE AND SUBTITLE</b> Disposable, Autonomic, Energy-Converting Ion Channel Sensor Materials				<b>5a. CONTRACT NUMBER</b>	
				<b>5b. GRANT NUMBER</b> FA9550-12-1-0435	
				<b>5c. PROGRAM ELEMENT NUMBER</b> 61102F	
<b>6. AUTHOR(S)</b> David Sept, Jerry Yang, Max Shtein, Nathan Gianneschi				<b>5d. PROJECT NUMBER</b>	
				<b>5e. TASK NUMBER</b>	
				<b>5f. WORK UNIT NUMBER</b>	
<b>7. PERFORMING ORGANIZATION NAME(S) AND ADDRESS(ES)</b> UNIVERSITY OF MICHIGAN 503 THOMPSON ST ANN ARBOR, MI 48109-1340 US				<b>8. PERFORMING ORGANIZATION REPORT NUMBER</b>	
<b>9. SPONSORING/MONITORING AGENCY NAME(S) AND ADDRESS(ES)</b> AF Office of Scientific Research 875 N. Randolph St. Room 3112 Arlington, VA 22203				<b>10. SPONSOR/MONITOR'S ACRONYM(S)</b> AFRL/AFOSR RTB2	
				<b>11. SPONSOR/MONITOR'S REPORT NUMBER(S)</b> AFRL-AFOSR-VA-TR-2018-0068	
<b>12. DISTRIBUTION/AVAILABILITY STATEMENT</b> A DISTRIBUTION UNLIMITED: PB Public Release					
<b>13. SUPPLEMENTARY NOTES</b>					
<b>14. ABSTRACT</b> <p>The objective of this 5-year project was to develop autonomous, ion channel-based biosensors, and achieving this goal required both invention and innovation on multiple, parallel fronts. First, we needed to design, synthesize and characterize a novel class of biomembrane forming materials. The tetraether lipids resulting from our work were inspired by naturally occurring Archaeal lipids and we show how they have many unique biophysical and biochemical properties. Second, we needed develop new cell penetrating peptides that would work with these materials, and then improve existing methods to measure membrane leakage in a more quantitative and reproducible manner. The third innovation was to build devices that could provide either chemiluminescent or photovoltaic readouts in response to our (bio)chemical signals. Lastly, using kirigami and origami-inspired techniques, we developed a hydrogel-based battery that produces electricity in a fashion similar to the electric eel. These batteries are biocompatible, transparent and rechargeable, and they are poised to inspire a completely new class of devices. Taken together, these findings represent significant advances in several areas and they will impact future research in materials science, chemistry, biochemistry and biophysics.</p>					
<b>15. SUBJECT TERMS</b> ion channel, membrane, sensor					
<b>16. SECURITY CLASSIFICATION OF:</b>			<b>17. LIMITATION OF ABSTRACT</b>	<b>18. NUMBER OF PAGES</b>	<b>19a. NAME OF RESPONSIBLE PERSON</b> BIN-SALAMON, SOFI
<b>a. REPORT</b>	<b>b. ABSTRACT</b>	<b>c. THIS PAGE</b>			
Unclassified	Unclassified	Unclassified	UU		

Standard Form 298 (Rev. 8/98)  
Prescribed by ANSI Std. Z39.18

DISTRIBUTION A: Distribution approved for public release.

				<b>19b. TELEPHONE NUMBER</b> <i>(Include area code)</i> 703-696-8411
--	--	--	--	---

Grants.gov#: 11 16 15 68  
Grants Agreement Award#: FA9550-12-1-0435

## ANNUAL REPORT

### Disposable, Autonomic, Energy-Converting Ion Channel Sensor Materials

BAA-AFOSR-2012-0001 – Topic #2:

AUTONOMIC MATERIAL SYSTEMS UTILIZING BIOMOLECULAR TRANSDUCTION

Submitted to  
Air Force Office of Scientific Research

By  
The University of Michigan, Ann Arbor  
The University of California, San Diego  
Adolphe Merkle Institute, University of Fribourg

Principal Investigator:  
**David Sept**, Biomedical Engineering and Center for Computational  
Medicine and Bioinformatics (University of Michigan)  
Tel: (734) 615-9587 e-mail: [dsept@umich.edu](mailto:dsept@umich.edu)

Co-PIs:  
**Michael Mayer**, Adolphe Merkle Institute (University of Fribourg),  
[michael.mayer@unifr.ch](mailto:michael.mayer@unifr.ch)  
**Jerry Yang**, Chemistry and Biochemistry (University of California), [jerryyang@ucsd.edu](mailto:jerryyang@ucsd.edu)  
**Max Shtein**, Materials Science and Engineering (University of Michigan),  
[mshtein@umich.edu](mailto:mshtein@umich.edu)  
**Nathan Gianneschi**, Chemistry and Biochemistry (University of California),  
[ngianneschi@ucsd.edu](mailto:ngianneschi@ucsd.edu)

Research Topic Chief:  
**Dr. Sofi Bin-Salamon**, Intermin Program Manager for Natural Materials and Systems,  
AFOSR/RTB2, (703) 696-8411, [afosr.nature@us.af.mil](mailto:afosr.nature@us.af.mil)

January 31, 2018

<b>1. Abstract</b>	<b>4</b>
<b>2. Objectives for the full funding period</b>	<b>6</b>
<b>3. Design and synthesis of Archaea-inspired lipids for the development of leak-proof capsules</b>	<b>7</b>
3.1. Effects of tethering of lipid tails on membrane leakage at elevated temperatures	8
3.2. Effects of tethering of lipid tails on membrane leakage at room temperature	9
3.3. Effect of rings on membrane permeability of Archaea-inspired lipid membranes	12
3.4. Effect of headgroups on membrane permeability across Archaea-inspired tetraether lipid membranes	13
3.5. Encapsulation and leakage of small organic molecules from liposomes comprised of tetraether lipids	14
3.5.1. Effect of the electrical properties of small molecules on their encapsulation and retention from liposomes comprised of tetraether lipids	14
3.5.2. Effect of structural elements of small molecules on their encapsulation and retention from liposomes comprised of tetraether lipids	16
3.6. Cholesterol integrated chimeric Archaea-inspired tetraether lipid	17
3.7. Stimuli-responsive hybrid tetraether liposomes	19
3.8. Fusogenic properties of biomimetic membranes of Archaea-inspired lipids	21
3.9. Application of archaea-inspired lipids as fluid nanopore coatings	22
<b>4. Synthesis and evaluation of gramicidin A nanopores for the detection of small molecules</b>	<b>24</b>
4.1. An engineered melittin variant forms well-defined pores	26
4.2. Another pore-forming peptide, Ceratotoxin A, displays alamethicin-like activity	28
4.3. DNA-programmed assembly for formation of preferentially-sized pores	30
4.4. Further work on Ceratotoxin A	31
<b>5. Hydrogel-based reverse-electrodialytic battery systems based on the electric organ of <i>Electrophorus electricus</i></b>	<b>39</b>
5.1. Fluidic implementation produces small voltages	40
5.2. Printed implementation generates up to 110 volts	41
5.3. <i>Miura-ori</i> fold provides 40-fold improvement in power characteristics	41
5.4. External power supply can recharge artificial electric organ	43
5.5. Outlook	44
<b>6. Molecular Dynamics Simulations of Archaea-Inspired Lipids</b>	<b>46</b>

6.1. Simulation Details	46
6.2. Self-Diffusion of Lipids	46
6.3. Area per Lipid Headgroup	48
6.4. Membrane Thickness	49
6.5. Membrane Mechanics	51
6.6. Lipid Order Parameters	52
6.7. Simulations of unlinked, tethered and cyclic lipids	54
6.8. Tethered lipids and lipid folding	60
6.9. Effects of rings on membrane biophysics	63
6.10. Simulation Studies of the GcGTPC-CH Lipid	66
<b>7. Self-powered, photovoltaic-based ion sensing</b>	<b>73</b>
7.1. Dye-sensitized photovoltaic device-based platform	73
7.1.1. Motivation	73
7.1.2. Concept	73
7.1.3. Main Results & Conclusions	74
7.1.4. Electrical Characterization	75
7.1.5. Electrochemical Impedance Measurements	75
7.1.6. SEM/EDX Measurements	76
7.2. Chemiluminescence (CL) based sensing	77
7.2.1. Motivation:	77
7.2.2. CL assay for Fluoride detection:	77
7.2.3. Detection setup & Sensing protocol:	78
7.2.4. Main Results & Conclusions:	80
7.2.5. Summary:	84
7.3. Improving photodetector quantum efficiency	84
7.4. Kirigami- and Origami-inspired structures for autonomous signal transduction	85
7.5. Electric Organ of Eel	87
7.6. Biomimetic phototrophic and phototactic surfaces	89
7.7. Circular kirigami-based springs & tunable antennas	92
7.8. Significance and follow-on work:	97
<b>8. Suported personnel</b>	<b>99</b>
<b>9. Collaborations</b>	<b>100</b>
<b>10. Publications</b>	<b>101</b>

## 1. Abstract

The overall aim of this 5-year project was to develop autonomic, biosensor materials. Achieving this goal required a significant level of innovation and invention on several fronts.

*Hybrid-lipid synthesis and characterization.* Our work involved the synthesis of a large series of membrane-forming materials inspired from natural Archaea lipids. The unusual structural features of the lipids found in these extremophile organisms help reduce membrane permeability under harsh conditions. We explored methods to combine strategies from both Archaea and Eukaryota to generate hybrid lipid structures to further increase membrane robustness and reduce membrane leakage compared to our previous generation of lipids. We found that these hybrid lipids have superior capability to encapsulate and retain small ions and small molecules compared to commercially available lipid materials. We have also begun to explore the capability to incorporate functional biomolecules into our synthetic membranes and have begun to explore the capability to deliver molecules to cells with or without the presence of an external stimulus.

*Chemical modification and characterization of pore-forming peptides.* In keeping with our interest in developing ion channels for sensing and signal amplification, we investigated the electrophysiological characteristics of the large, stable pores formed by the natural peptide ceratotoxin A and the synthetic peptide known as MelP5, which we compared to its source compound, melittin, a component of bee venom. We used planar lipid bilayer recordings to examine the activity of these compounds on the single-pore level. We plan to use modified CtxA for targeted cell killing.

*Archaea-liposome permeability studies using tethered liposome platform.* We have implemented a platform to tether liposomes to a glass surface and interrogate their internal pH using fluorescence microscopy. Here we adapt our proton permeability assay to the tethered liposome platform and show plans to perform temperature-dependent proton permeability studies on synthetic archaea-inspired lipid membranes.

*Hydrogel-based origami-enabled reverse-electrodialytic battery systems based on the electric organ of *Electrophorus Electricus*.* We sought to develop a means of simultaneously assembling series of tetrameric hydrogel reverse-electrodialytic battery systems in a geometry that minimized electrical resistance. The lowest-resistance geometry for such a system is a stack of thin films, so we investigated the use of folding substrates with a *Miura-ori* pattern as a means of simultaneously and scalably stacking thin hydrogel films in a sequence. We were able to use printing to pattern the gel components of a battery onto substrates with pre-perforated 45-degree *Miura-ori* fold lines to develop a system with robust self-registration. We used an 80-degree fold with through-substrate ionic conduction to assemble uninterrupted stacks of thin films, improving the power output of the battery by a factor of 40 compared to lateral conduction. Reducing the thickness of the films resulted in improved power output; the thinnest films supportable on a *Miura-ori* substrate had a power density of 30 mW m<sup>-2</sup> per cell. Finally, we demonstrate a “contact-lens” morphology: a thin gel trilayer which is soft, transparent, and generates an open-circuit voltage of 80 mV.

*Biophysical characterization of our cholesterol-hybrid lipid.* Our previous year's report presented results for a new lipid (GcGTPC-CH), a tetraether lipid with covalently linked cholesterol molecules. We have now completed molecular simulations of GcGTPC-CH membranes and they reveal a number of unique biophysical properties, including a high lateral isothermal compressibility, very slow rate of self-diffusion, and a hydrophobic core that is nearly inaccessible to water molecules. These unique properties are linked to the low permeability of these membranes, but the exact relationship is still a subject of ongoing work.

*Droplet-Interface Bilayers for Autonomic Sensing of Biomarkers:* We have considered droplet-interface bilayers (DIBs) as a platform to achieve the original aims of the grant proposal: to use engineered ion channels to autonomically sense biomarkers and other molecules within samples. We have established a set of conditions for the formation of stable DIBs in well plates and developed a system that visually reports the gramicidin-mediated equilibration of a pre-established pH gradient across these bilayers using a pH-sensitive dye. We will soon begin attempting to detect small molecules using established switchable ion channels in our DIB setup.



## 2. Objectives for the full funding period

The **overall goal for the entire funding period** of this project is to design *bio-inspired*, *autonomic*, *efficient* and *robust* sensor materials that will work in *resource-poor* environments and *do not require an external power source*. Design goals of these sensor materials are: autonomous operation (inspired by phototrophic, chemotrophic, and lithotrophic organisms), strong amplification (inspired by electric eels), simple and modular design (basic components inspired by living organisms), built-in redundancy (both with regard to sensing and readout), and versatility (can be adapted for a wide range of antigens).

Below is the timeline provided in the initial proposal. Several of the objectives were completed ahead of schedule and this allowed us to expand the scope of parts of our research.

	2012	2013				2014				2015				2016				2017		
	Q4	Q1	Q2	Q3	Q4	Q1	Q2	Q3	Q4	Q1	Q2	Q3	Q4	Q1	Q2	Q3	Q4	Q1	Q2	Q3
4.2.A Synthesis of Robust Lipids																				
4.2.B Formation of Capsules																				
4.2.C Synthesis of Ion Channel-based Sensors																				
4.2.D Characterization of Sensors in Phospholipids																				
4.2.E Characterization of Sensors in Novel Capsules																				
4.2.F Integration on Disposable Test Strips																				
4.2.G Fabrication of Electrodes																				
4.2.H Integration on Miniature Electrodes																				
4.2.I Integration into Autonomous Materials																				

### 3. Design and synthesis of Archaea-inspired lipids for the development of leak-proof capsules

Tetraether lipids, unique membrane lipids of several archaea species, are characterized by a number of features that make them interesting candidates for preparing stable and leak-proof capsules. Compare to bilayer forming lipids, tetraether lipids span the entire membrane structure (**Figure 1**). The resulting monolayer membrane is more stable and less leaky for small molecules than a common bilayer membrane.<sup>1</sup> Furthermore, tetraether lipids contain ether bonds (instead of ester bonds) rendering them less prone to hydrolytic attacks.<sup>2</sup> A particularly attractive point concerns the increasing proportion of cyclopentane rings in thermoacidophilic lipids with increasing environmental temperature.<sup>1,3</sup> The presence of cyclopentane rings presumably can be used to fine-tune the rigidity of the membrane in direct response to the growth temperature of the organisms. The role of the cyclopentane residues in membrane properties was previously modeled *in silico* by Chong et al., predicting that increasing the number of rings significantly changes the packing arrangement of lipids leading to improved maintenance of proton gradients between extracellular and intracellular compartments over a wide range of growth temperatures.<sup>4</sup> It has also been revealed that Archaea have adjusted their membrane lipids to cope with cold conditions in the ocean by the formation of an internal cyclohexane ring mixed with four cyclopentane rings (**Figure 1**).<sup>5</sup>

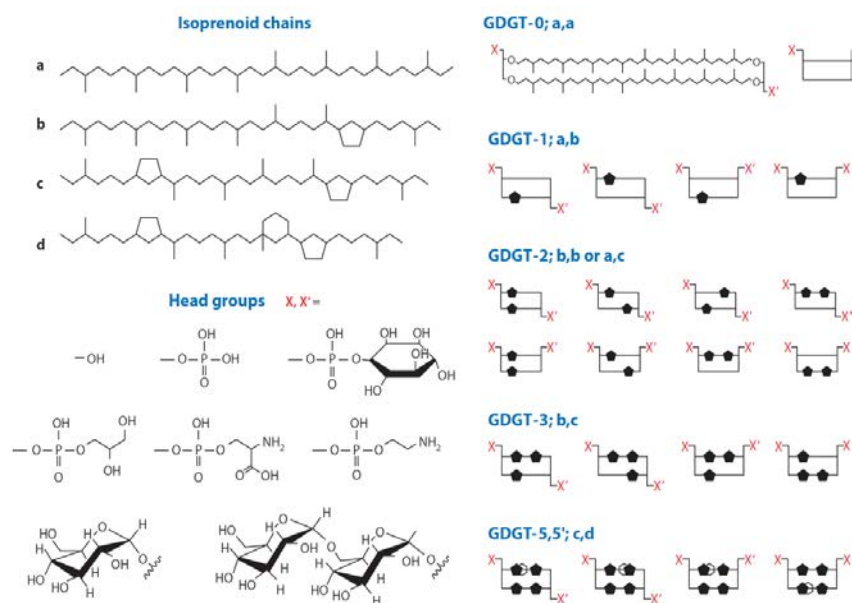


**Figure 1.** Tetraether lipids with varying hydrophobic core and polar lipid headgroups found in archaeal membranes.<sup>5</sup>

For the design of robust membranes with low permeability for ions or small molecules, our main objective was to understand the effects of Archaea-inspired lipid structures on membrane thermal stability and permeability. Thus, we designed and synthesized series of synthetic

tetraether lipids incorporating different hydrophobic cores (length, type and number of rings) and head groups.

### 3.1. Effects of tethering of lipid tails on membrane leakage at elevated temperatures

One interesting feature of membranes from thermophilic archaea is their increased fraction of tethered lipids—that is, fully membrane spanning lipids containing two polar head groups with covalently linked lipid tails—as a function of increasing temperature (**Figure 1**).<sup>6</sup> This adaptation has led to speculation that molecular tethering of lipids plays a role in regulating flexibility and fluidity of archaea membranes at elevated temperatures. However, due to the complexity of mixtures from natural lipids present in membrane extracts and the lack of available synthetic tethered lipids, there are few reported studies that examine the effect of lipid tethering on membrane function at elevated temperatures. For instance, previous studies show that tethering of synthetic lipids decreases membrane leakage of small molecules and ions at high temperatures compared to untethered lipids.<sup>7</sup> Most of these reports, however, examine leakage from lipid mixtures or do not report information on lipid characteristics (such as phase transition temperatures, distribution of size of liposomes, or lamellarity), making it difficult to provide an evidence-based mechanistic understanding of the relationship between the structure of tethered lipids and membrane leakage profiles at different temperatures. We obtained results from the temperature-dependent liposome leakage experiments of three synthetic lipids (**Figure 2a**) together with molecular dynamics simulations to provide insight into the effect of tethering on membrane leakage at temperatures ranging from 22-70 °C.

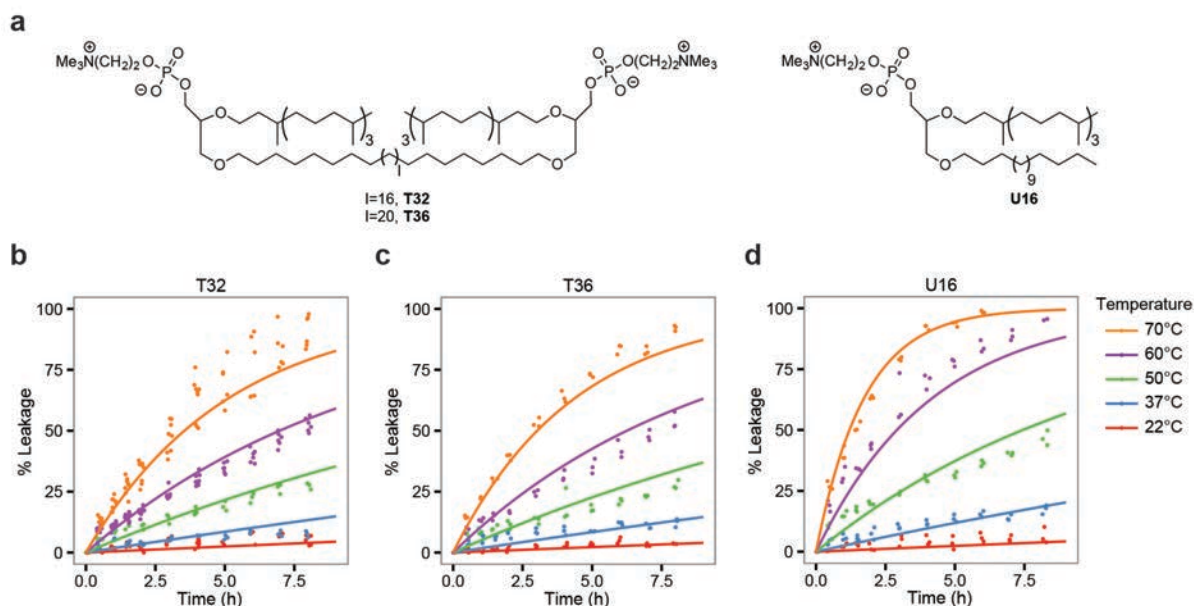


**Figure 2.** Chemical structures of lipids (a) and kinetic release of encapsulated carboxyfluorescein (CF) leakage from liposomes (b-d). Temperature dependent CF-release profile from liposomes prepared from T32 (b), T36 (c) and U16 (d).

**Fig. 2b-d** shows the efflux of CF from small liposomes comprised of each of the 3 pure lipids as a function of temperature. While liposomes from all 3 lipids exhibited increasing rates of CF leakage as a function of increasing temperature, liposomes comprised of T32 and T36 showed a reduced dependence of temperature on leakage compared to U16. The only difference between any of these leakage experiments was the structure of the lipids, demonstrating that the presence of the tether in the lipid influences the temperature dependence of CF leakage. The experimental data and MD simulations showed that lipid tethering significantly increases the entropic barrier for permeation, which is a result of increased ordering of lipid tails and increased packing of the lipids in tethered versus untethered lipid membranes. While MD simulations did not support a correlation between lipid tail tethering and membrane flexibility (as estimated by bending stiffness) as proposed by others, both experimental results from FRAP experiments and from MD simulations of long range diffusion of lipid membranes support a significant effect of lipid tethering on fluidity of the membrane.

This study reveals a fundamental design principle for maintaining membrane integrity at elevated temperatures. Namely, in order to render membranes resistant to leakage at elevated temperatures, it is important for the energetic barrier for molecular leakage to be strongly dependent on entropy of activation. Tethering is one strategy towards achieving this goal. A manuscript regarding this work is currently in preparation.

### **3.2. Effects of tethering of lipid tails on membrane leakage at room temperature**

As the extremophiles that express tethered lipids often live in acidic environments, it has commonly been hypothesized that tethered lipids slow passive proton permeation in these microbes, allowing them to maintain a near-neutral internal pH using active proton efflux mechanisms.<sup>1,2</sup> In order to tease out relationships between lipid structure and proton/hydroxide permeability, we adapted a ratiometric fluorescence-based assay previously reported by Paula and coworkers to monitor the equilibration of pH gradients across homogeneous liposome membranes.<sup>3</sup> We tested lipids from **Figure 2a** as well as the commercially-available lipids shown in **Figure 3a** by measuring the fluorescence signal over time emitted by a pH-sensitive dye encapsulated in liposomes after a pH “jump” of 0.5 pH units was imposed on the exterior solution. We fit the resulting traces (**Figure 3b**) with an equation derived from Fick’s law in order to extract values for the proton/hydroxide permeability of the membranes (**Figure 3c**).

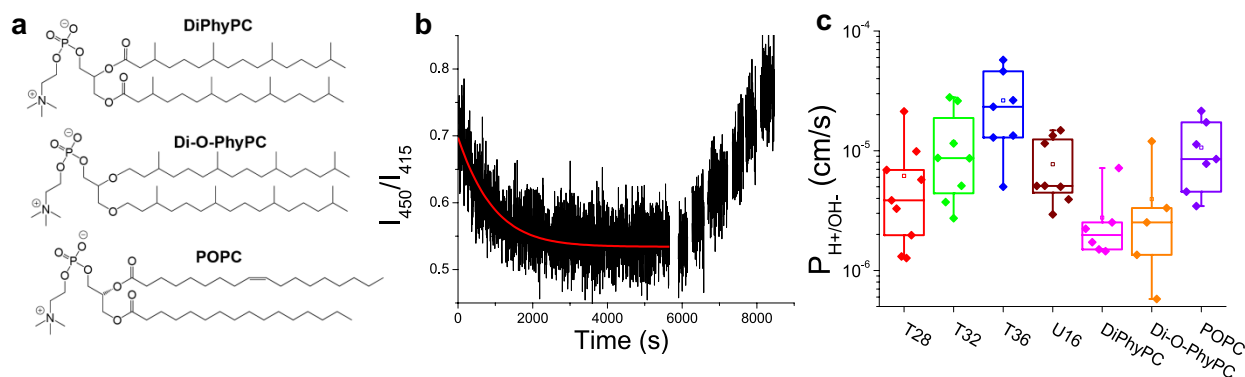


**Figure 3.** Chemical structures of lipids (a), Example trace of fluorescence ratio over time during pH equilibration followed by internal calibration (b), and proton/hydroxyl permeability values obtained from fitting fluorescence ratio traces (c).

We found that lipids containing two tails with repeating isoprenoid methyl branches (DiPhyPC and Di-O-PhyPC, **Figure 2a**) formed membranes that were less permeable to protons than a lipid containing only one isoprenoid tail (U16, **Figure 3c**). The lipid in the T series with the longest transmembrane tether (T36, **Figure 2a**) formed membranes that were the most permeable to protons, while the lipid with the shortest tether (T28) formed the least permeable membranes of the series. The presence of a transmembrane tether (T32 vs. U16) did not impact the proton permeability.

The latter two results are initially counterintuitive. In particular, thick lipid membranes are typically less permeable to any species than thin ones, and T32 membranes were found to be thicker than T28 membranes by atomic force microscopy and molecular dynamics simulations. However, molecular dynamics simulations of large (20 x 20 nm) patch of membrane in water over 50 ns revealed that water molecules spontaneously penetrate into the hydrophobic region of lipid membranes in a manner consistent with this trend between lipids. As most current models of proton/hydroxide permeation across lipid membranes involve the formation of short-lived clusters of water molecules within the membrane,<sup>3-7</sup> we examined trends in the frequency of such simulated penetration events. We found that the number of times that at least three molecules were observed in the membrane's hydrophobic region correlated strongly with the measured average proton/hydroxide permeability values (**Figure 4a**,  $r = 0.99$ ), as did the number of times that two or more water molecules were observed within 5 Å of each other, defined as a "cluster" (**Figure 4b, 4c**,  $r = 0.88$ ).

The finding that transmembrane tethering did not impact proton permeability ran counter to our initial hypothesis but was also indicated by the simulation results, indicating that these metrics may be useful for as an *in silico* test for designing membrane compositions. Additionally, the experiments in this study were carried out at room temperature. Prior literature<sup>8</sup> indicates that liposome membranes composed of lipid extracts from extremophile membranes containing tethered lipids are less permeable than “normal” eukaryotic lipid extracts at high temperatures, but not at room temperature; the results from Section 1.1 suggest that this effect may also be at play in this series of synthetic lipids, as well.

This work has been published in *Biophys. J.*, 2016, **110** (11), 2430-2440.

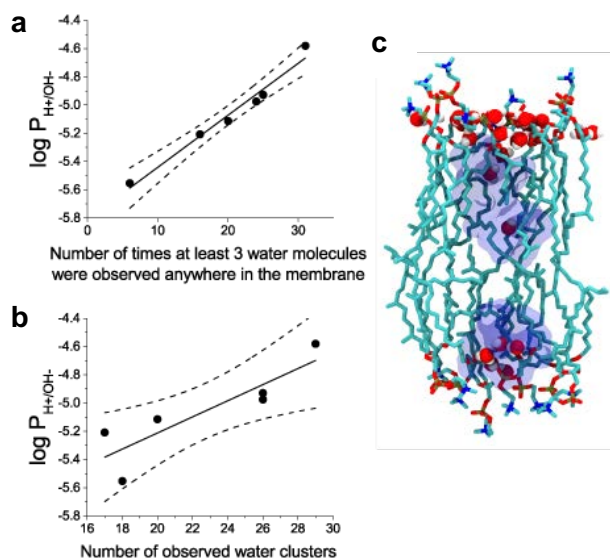


**Figure 4.** Correlation plots of the logarithm of the proton/hydroxide permeability as a function of the number of times at least three water molecules were observed in the hydrophobic region anywhere in the lipid membrane (a) and as a function of the number of observed water clusters, defined as two water molecules observed within 5 Å of one another (b). A snapshot from a simulation of a T28 membrane showing the penetration of water molecules into the hydrophobic region (c).

### 3.3. Effect of rings on membrane permeability of Archaea-inspired lipid membranes

We designed the series of synthetic lipids shown in **Figure 5** to evaluate the effects of two important structural elements found in many Archaea lipids on membrane permeability for small ions: 1) the effect of tethering of alkyl tails to create bolaform amphiphiles capable of spanning the length of the membranes, and 2) the effect of incorporation of cyclopentane or cyclohexane rings within the tethered lipid chain.

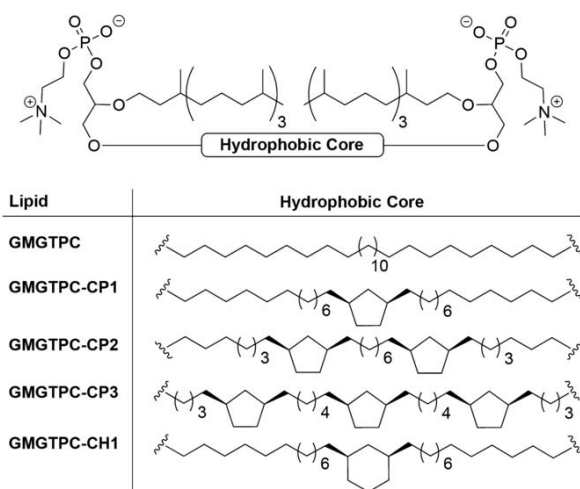


**Figure 5.** Structures of synthesized tetraether Archaea-inspired lipids

In order to evaluate the relative permeability of membranes formed from these different lipids, we developed a modified pH equilibration assay that was previously reported by Kakinuma and coworkers.<sup>8</sup> In this assay, we encapsulated CF within the liposomes with an initial internal liposomal pH of 7.2. The liposomes were then incubated in a buffered solution with an external pH of 5.8, and the change in fluorescence intensity of CF was monitored over time as the internal liposome pH equilibrated to pH 5.8.

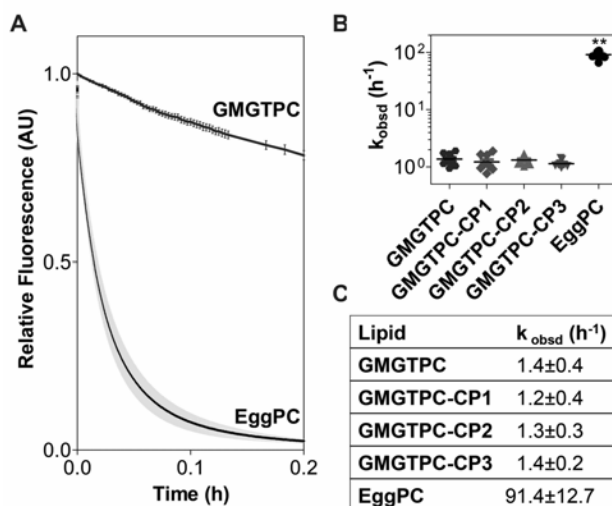


**Figure 6.** Observed rate of pH equilibration from liposomes formed from EggPC or synthetic lipids. A) The change in CF fluorescence intensity from CF-encapsulated GMGTPC or EggPC liposomes versus time. B) Comparison of the observed initial rates of decreased CF fluorescence intensity from CF-encapsulated liposomes composed of different lipids. C) Average detected initial rates of pH equilibration in liposomes composed of different lipids. Standard errors of the mean are provided based on nine measurements each. Statistical analyses were performed using a paired t-test. \*\* indicate a  $p$ -value  $< 0.01$ .



We found that membranes formed from pure tetraether lipids leaked small ions at a rate that was ~2 orders of magnitude slower than common, bilayer-forming lipids (**Figure 6a-c**). Interestingly, incorporation of cyclopentane rings into the tetraether lipids did not affect membrane leakage, whereas a cyclohexane ring reduced leakage by an additional 40%. These results show that mimicking certain structural features of natural Archaea lipids results in improve membrane integrity, which may help overcome limitations of many current lipid-based technologies. This work has been published in *Angew. Chem. Int. Ed.* **2016**, *55*, 1890.

### 3.4. Effect of headgroups on membrane permeability across Archaea-inspired tetraether lipid membranes

The mixtures of polar lipid headgroups in Archaea membranes are dependent on specific growth conditions.<sup>3</sup> For instance, under acidic conditions, the lipid composition of Archaea will include a higher fraction of headgroups that can facilitate hydrogen bonding between the headgroups on adjacent lipids.<sup>9,10</sup> **Figure 1** shows the structures of common polar lipid headgroups that are found naturally in Archaea.<sup>5,11</sup> The delicate balance in generating a precise mixture of lipids comprised of these different polar headgroups is thought to be essential in maintaining a viable membrane under harsh conditions.<sup>12</sup> previous computational<sup>13</sup> and experimental studies<sup>14</sup> suggest that lipid headgroups affect membrane permeation of water, but have little effect on permeability of small organic molecules across membranes.<sup>15</sup> However, to our knowledge no systematic study on effects of headgroups on small ion permeability has been reported. Thus, we designed and synthesized Archaea-inspired GMGT lipid analogs containing 4 different headgroups found in nature (phosphocholine, PC; phosphoethanolamine, PE; phosphatic acid, PA; phosphoglycerol, PG; **Figure 7a**) and investigated the effect of headgroups on small ion membrane permeability across membranes comprised of these lipids. In order to examine how these results compared to the effect of headgroups on standard bilayer-forming diacylphospholipids, we also examined leakage of small ions from 1-palmitoyl-2-oleoyl-sn-glycerol (PO) lipids.

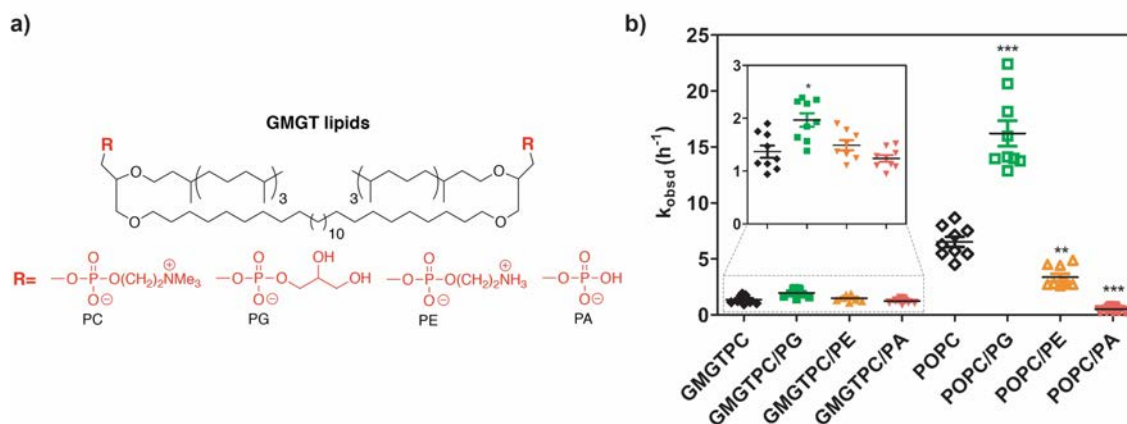


**Figure 7.** a) Structures of synthesized tetraether GMGT lipids incorporating different headgroups (phosphocholine, PC; phosphoethanolamine, PE; phosphatic acid, PA; phosphoglycerol); b) Observed



initial rate of pH equilibration from liposomes formed from GMGT or PO series of lipids. Comparison of the observed initial rates of decreased CF fluorescence intensity from CF-encapsulated liposomes comprised of pure GMGTPC lipid or 1:1 mixtures of GMGTPC with GMGTPG, GMGTPE, or GMGTGA (the inset represents a zoomed in graph of the observed initial rates of leakage from the GMGT lipids); and pure POPC lipid or 1:1 mixtures of POPC with POPG, POPE, or POPA. Statistical significance was determined using a paired Student t-test. \*, \*\*, \*\*\* indicate a p-value of < 0.1, 0.01, 0.001, respectively, relative to the  $k_{\text{obsd}}$  of the analogous PC lipid.

Our results showed that membrane leakage rate across GMGT lipid membranes varied by a factor of  $\leq 1.6$  as a function of headgroup structure (**Figure 7b**). However, the leakage rates of small ions across membranes comprised of commercial bilayer-forming 1-palmitoyl-2-oleoyl-sn-glycerol (PO) lipids varied by as much as 32-fold within the same series of headgroups. These findings suggest that GMGT lipids may offer greater flexibility for tailoring the functionality presented in the lipid headgroups, without significantly compromising membrane permeability. Such versatility in the design of lipid headgroups may open up opportunities to use GMGT lipids in a range of applications including the incorporation of receptor targeting molecules on lipids for development of liposomal cargo<sup>16</sup> or the incorporation of ligands as well as charged headgroups to attract specific analytes or binding partners to the membrane surface for biophysical studies.<sup>17</sup> This work has been published in *Chem. Eur. J.* **2016**, *22*, 8074.

### 3.5. Encapsulation and leakage of small organic molecules from liposomes comprised of tetraether lipids

After showing that membranes formed from pure synthetic tetraether lipids leaked small ions at a rate that was about two orders of magnitude slower than common bilayer-forming lipids, our next goal was to assess whether or not our previous results with small ions could translate to the encapsulation and retention of small hydrophilic molecules in tetraether-based liposomes.

#### 3.5.1. Effect of the electrical properties of small molecules on their encapsulation and retention from liposomes comprised of tetraether lipids

We encapsulated three small hydrophilic molecules displaying different electronic charges at pH 7.4, in GMGTPC liposomes: neutrally charged cytarabine (Ara-C), positively charged vincristine (VCR) and negatively charged methotrexate (MTX) (**Figure 8A**). Passive loading of Ara-C and MTX afforded low but similar small molecule-to-lipid molar ratio for both GMGTPC and EPC. In contrast, the tetraether GMGTPC lipid was superior to the diacyl lipid for active loading of VCR. While both lipids formed liposomes with similar size (and, thus, internal volume), the difference in encapsulation efficiency could be explained by the difference of proton permeability between membranes comprised of pure GMGTPC or EPC.<sup>18</sup> We hypothesize that the reduced permeability of GMGTPC membrane for small ions (e.g.  $\text{H}^+$ ) should help to maintain a pH-gradient across liposome membrane, allowing higher encapsulation efficiency compared to highly proton permeable membranes formed from EPC.

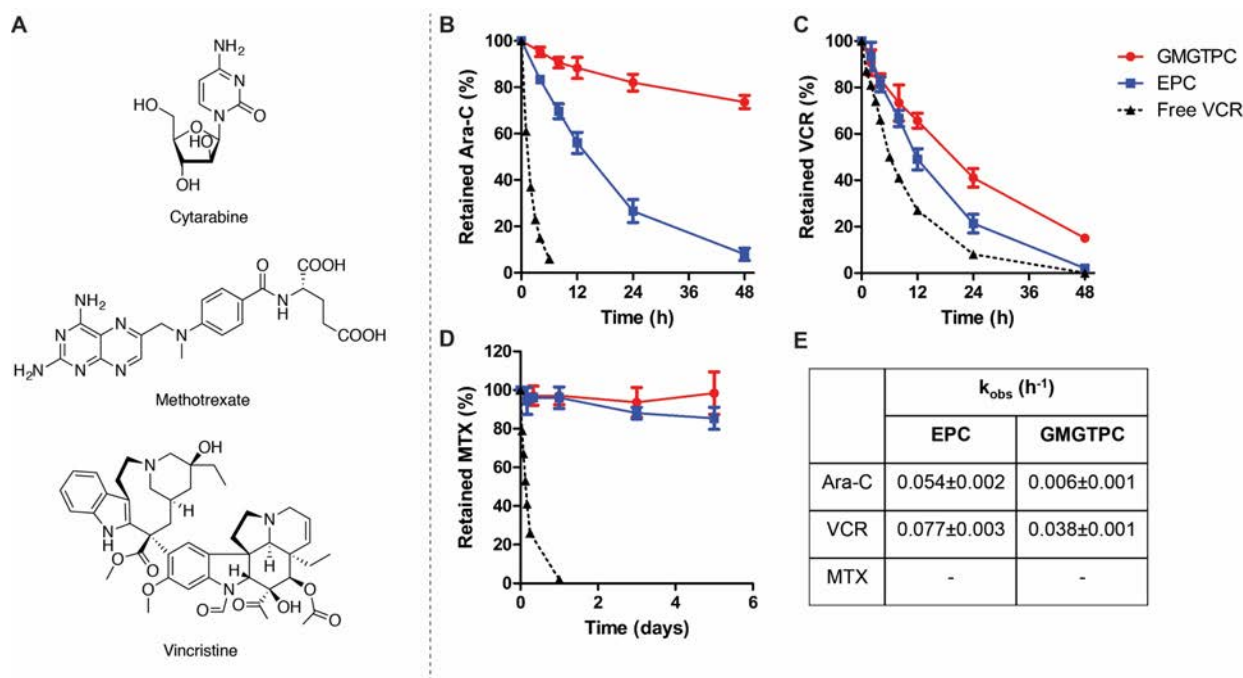


**Figure 8.** Structures and retention profiles of cytarabine (B), vincristine (C) and methotrexate (D) encapsulated in GMGTPC liposomes (red lines) or EPC liposomes (blue lines). Liposome suspensions were dialyzed in 20 kDa cutoff Slide-A-Lyzer mini dialysis units (at 37 °C in HBS) and the remaining encapsulated molecule was measured by HPLC at different time points. Dashed lines represent the transport of the free molecule across the dialysis membrane. (E) Average observed rates of molecule leakage in liposomes made of EPC or GMGTPC. All measurements were recorded in triplicate and are represented as a mean  $\pm$  SEM ( $n = 3$ ).

All three molecules presented important differences for liposomal retention based on their physicochemical properties. For instance, neutrally charged Ara-C (pKa of the anilinium group is 4.2)<sup>19</sup> was more rapidly released from liposomes compared to negatively charged MTX (pKas of the two carboxylate groups are 4.8 and 5.6).<sup>20</sup> The results from small molecule leakage studies shown in **Figure 8b** are in agreement to reports claiming that the membrane permeability of neutral molecules is expected to be orders of magnitude faster than the membrane permeability of charged species.<sup>21</sup> The observed leakage profile of Ara-C from GMGTPC liposomes, in particular, highlights a potential advantage of using GMGTPC liposomes over liposomal formulations comprised of conventional diacyl lipids such as EPC for the encapsulation and retention of neutrally charged molecules. The rate of release of VCR (which has been shown to contain two protonated amine groups in water with pKas of 5.0–5.5 and 7.4)<sup>22</sup> from liposomes is dependent on the ability of the membrane to maintain a transmembrane pH gradient, since only the neutral form of VCR can cross the liposomal. Using folic acid-targeted liposomes, we also demonstrated that GMGTPC liposomes have the potential to deliver and release small organic molecules (calcein, cytarabine and vincristine) to specific cells. This work has been published in *Org. Biomol. Chem.* **2017**, *15*, 2157-2162.

### 3.5.2. Effect of structural elements of small molecules on their encapsulation and retention from liposomes comprised of tetraether lipids

After finding that liposomes made of a pure tetraether lipid exhibited a 9-fold decrease in the rate of leakage of the neutral and hydrophilic molecule Cytarabine compared to liposomes formed from a commercial diacyl lipid,<sup>23</sup> we probed the effects of neutral molecule structure on leakage from liposomes. We restricted this study to seven hydrophilic molecules which are neutrally charged at physiological pH and are pyrimidone-based nucleoside analogues with different sugar derivatives bonded to the base via  $\beta$ -N1-glycosidic bonds (**Figure 9A**). We hypothesized that their incremental differences in structure could help identify chemical elements that are important for good liposomal retention in this class of compounds. To examine how encapsulation and retention of neutral molecules in liposomes made of tetraether lipids differ from liposomes comprised of standard bilayer-forming diacylphospholipids, we also examined leakage of the same molecules from liposomes made of 1-palmitoyl-2-oleoyl-sn-glycerol (POPC) lipids.

Both lipid systems exhibited different leakage profiles according to the structure of the molecules, but liposomes made of tetraether lipids generally showed better retention (up to 4-fold improvement) for the molecules compared with liposomes made from standard bilayer-forming POPC lipids (**Figure 9B-C**). The results suggest that chemical groups on position C2' of the sugar moiety are clearly a driving force for leakage. Removal (as in Deoxycytidine, blue lines) or change of stereochemistry (as in Cytidine, red lines) of the hydroxyl group at this position resulted in faster leakage rates compared to Cytarabine. Even faster leakage of 2'-Fluoro-2'-deoxycytidine and Gemcitabine further supported the importance of a hydroxyl group on position C2' for retention in liposomes. Introduction of one atom (as in 2'-Fluoro-2'-deoxycytidine, pink lines) or two atoms (as in Gemcitabine, green lines) of fluorine on position C2' led in both cases to higher membrane permeability of these compounds compared to Cytarabine, with complete leakage reached within 24 hours. Finally, changes in the pyrimidone moiety or changing the methylene to a sulfur atom at position C3' of the sugar also had significant effects on leakage. In the case of Lamivudine (orange lines), liposomal encapsulated molecules showed only slight slower leakage in the dialysis assay as the free molecules, indicating rapid release of this molecule from the liposomes. Removal of the amino group in the pyrimidone moiety (as in Zebularine) also resulted in nearly complete leakage of the molecule during liposome preparation, suggesting that the structure of both the sugar and the nucleobase are important for retention of this class of molecule in liposomes.

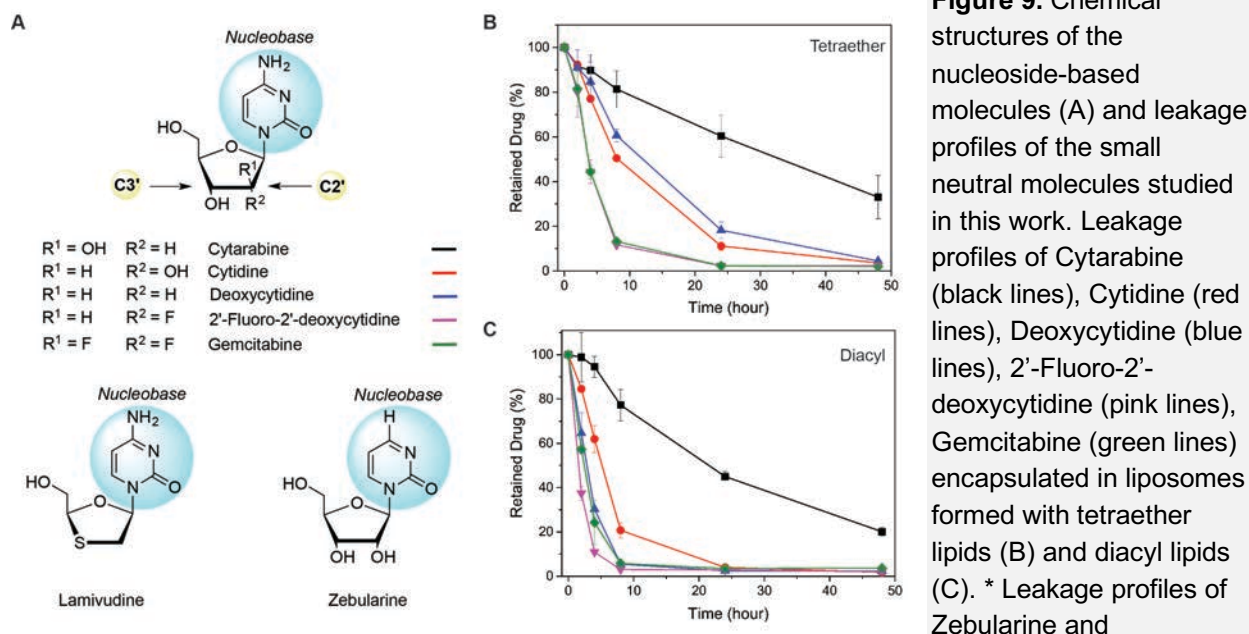


**Figure 9.** Chemical structures of the nucleoside-based molecules (A) and leakage profiles of the small neutral molecules studied in this work. Leakage profiles of Cytarabine (black lines), Cytidine (red lines), Deoxycytidine (blue lines), 2'-Fluoro-2'-deoxycytidine (pink lines), Gemcitabine (green lines) encapsulated in liposomes formed with tetraether lipids (B) and diacyl lipids (C). \* Leakage profiles of Zebularine and

Lamivudine in Graph B and Graph C are not shown due to the observed fast leakage in the dialysis assay used to assess retention of molecules. All measurements were recorded in triplicate and are represented as a mean  $\pm$  SEM ( $n = 3$ ).

Further kinetic studies revealed that molecular parameters typically used to assess lipophilicity (tPSA, SASA, and SA) were not sufficient to predict the relative membrane permeability of the nucleoside-based molecules.<sup>24</sup> This work, thus, reveals that certain chemical features of pyrimidone-based molecules such as fluorine atoms and hydrogen bond donor groups can strongly influence membrane permeability. It remains to be seen whether liposomal retention of other classes of molecules will also be heavily influenced by specific chemical features that can override general lipophilic properties. This work has been published in *Bioorg. Med. Chem. Lett.* **2017**, 27 (18), 4319-4322.

### 3.6. Cholesterol integrated chimeric Archaea-inspired tetraether lipid

Traditionally, cholesterol have been added to lipid mixtures to improve permeability properties towards small molecules/ion.<sup>25</sup> The addition of cholesterol is believed to increase packing by integrating in between adjacent lipid neighbors (**Figure 10a**).<sup>26</sup> However, cholesterol that is added during formulation has been observed to leak out of membranes resulting in leakage of cargo.<sup>27</sup> To solve the problem of membrane destabilization caused by cholesterol leakage, while maintaining the lower permeability properties, researchers have covalently connected cholesterol to the glycerol backbone<sup>28</sup>. Inspired by these previous work, we sought to improve our GMGT lipid scaffold by synthetically introducing a covalently attached cholesterol to the glycerol backbone of the GMGT lipid namely, cyclohexane integrated glycerol cholesterol glycerol tetraether phosphocholine lipid (GcGTPC-CH) (**Figure 10a**).

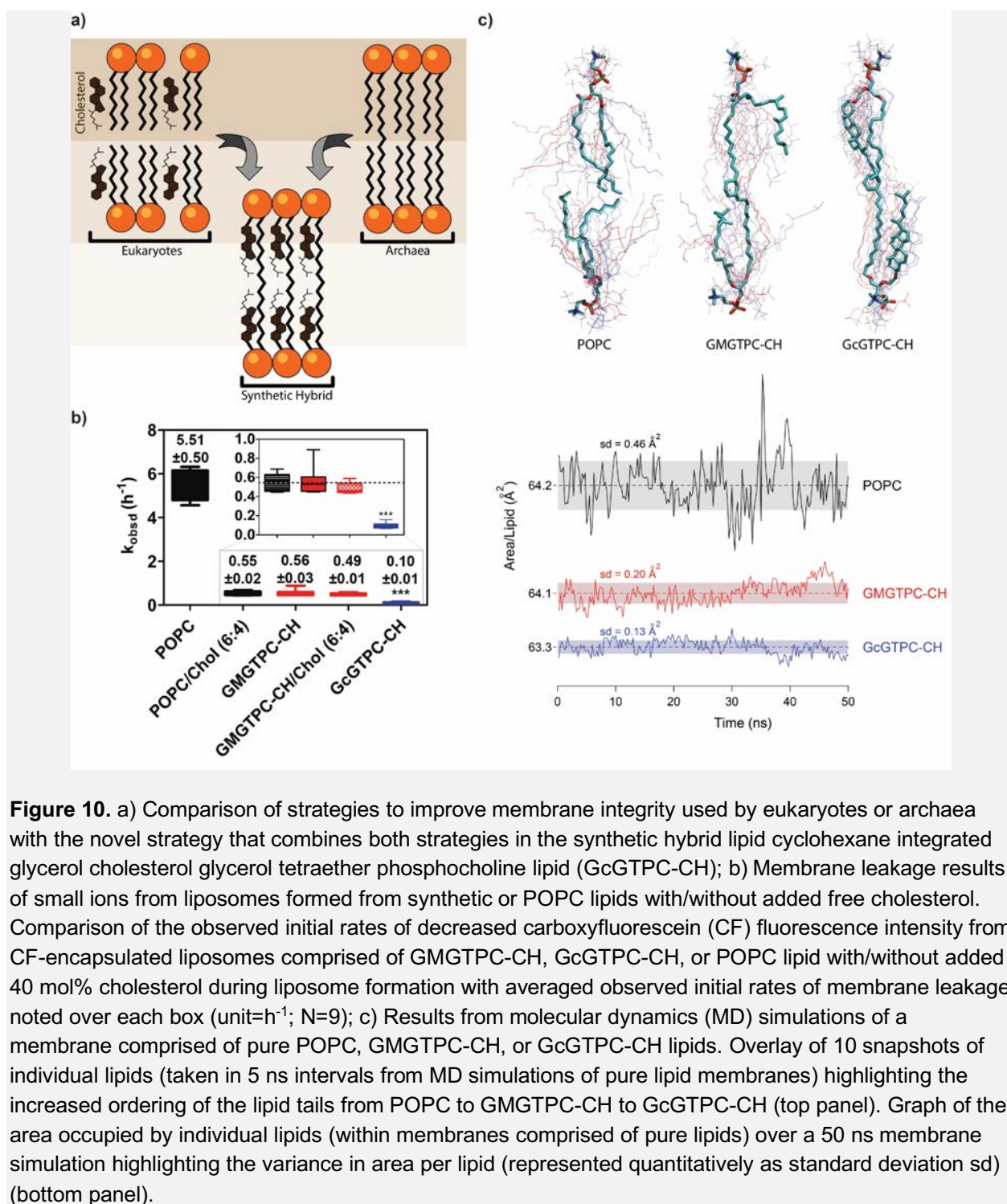


**Figure 10.** a) Comparison of strategies to improve membrane integrity used by eukaryotes or archaea with the novel strategy that combines both strategies in the synthetic hybrid lipid cyclohexane integrated glycerol cholesterol glycerol tetraether phosphocholine lipid (GcGTPC-CH); b) Membrane leakage results of small ions from liposomes formed from synthetic or POPC lipids with/without added free cholesterol. Comparison of the observed initial rates of decreased carboxyfluorescein (CF) fluorescence intensity from CF-encapsulated liposomes comprised of GMGTPC-CH, GcGTPC-CH, or POPC lipid with/without added 40 mol% cholesterol during liposome formation with averaged observed initial rates of membrane leakage noted over each box (unit= $h^{-1}$ ; N=9); c) Results from molecular dynamics (MD) simulations of a membrane comprised of pure POPC, GMGTPC-CH, or GcGTPC-CH lipids. Overlay of 10 snapshots of individual lipids (taken in 5 ns intervals from MD simulations of pure lipid membranes) highlighting the increased ordering of the lipid tails from POPC to GMGTPC-CH to GcGTPC-CH (top panel). Graph of the area occupied by individual lipids (within membranes comprised of pure lipids) over a 50 ns membrane simulation highlighting the variance in area per lipid (represented quantitatively as standard deviation sd) (bottom panel).

Our results showed that membranes formed from pure GcGTPC-CH lipids exhibit a 50-fold reduction in membrane permeability to small ions when compared with membranes comprised of a typical diacyl lipid, POPC, and a five-fold reduction in membrane permeability compared to

a previously reported archaea-inspired tetraether lipid, GMGTPC-CH, that lacks a covalently attached cholesterol group (**Figure 10b**).<sup>18</sup> We also demonstrated that pure GcGTPC-CH liposomes exhibited a ~30-fold reduction in leakage of a neutrally charged molecule, gemcitabine, compared to POPC liposomes with 40 mol% added cholesterol, and a ~10-fold reduction in leakage of the small molecule compared to GMGTPC-CH/chol liposomes. MD simulations provided some mechanistic insights that both tethering of lipid tails and incorporation of covalently attached cholesterol significantly increases the order of the lipid tails, which decreases the variance in area per lipid and tightens lipid packing (**Figure 10c**). These MD simulations also predict that the GcGTPC-CH lipids would exhibit the lowest penetration of water molecules of all 3 lipids examined, which is in agreement with the experimental results of reduced permeability of small ion and molecules across GcGTPC-CH lipid membranes. Although GcGTPC-CH lipid membranes exhibit remarkably low permeability and exceptional stability in solution (with or without serum), we also showed that these synthetic membranes retain properties that are typically found in natural membranes, such as the capability to incorporate functional biomolecules (here, ion channels formed from gramicidin A) and act as substrates for membrane-active enzymes (here, phospholipase-D). We also presented initial results on the cellular uptake of GcGTPC-CH liposomes containing encapsulated small molecule cargo. Our results support the concept that integrating covalently attached cholesterol groups to a tethered tetraether lipid, which combines lipid design strategies exploited by eukaryotes and archaea, leads to membranes with significantly improved stability and reduced permeability compared membranes formed from common bilayer-forming lipid formulations. This work has been published in *Chem. Eur. J.*, **2017**, *23*, 6757-6762.

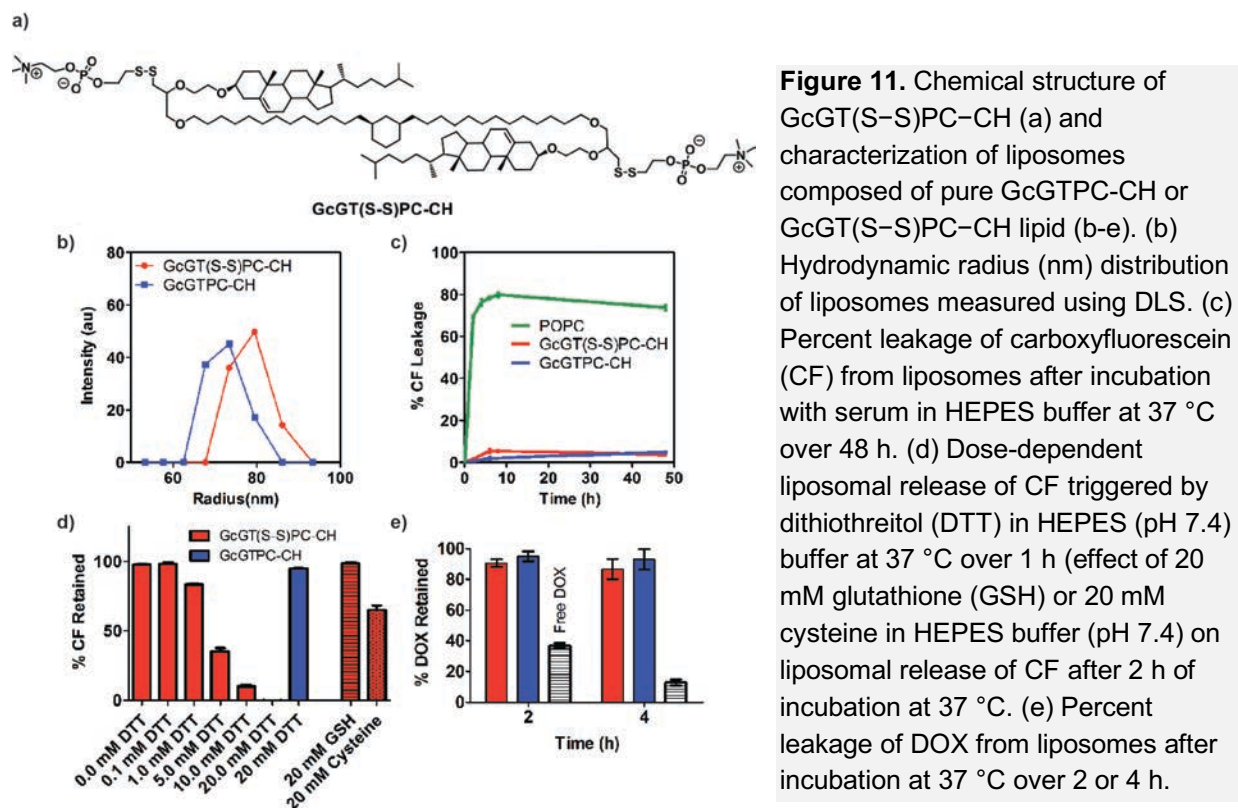
### 3.7. Stimuli-responsive hybrid tetraether liposomes

By incorporating design elements inspired from two different strategies used by nature to improve membrane robustness through modifications of membrane composition and lipid structure, we developed a unique lipid GcGTPC-CH, that showed ~50 times reduction of small ion membrane permeability and ~35 times increased retention of a neutral small molecule (gemcitabine) after 48 hours when compared with liposomes made from commercial diacyl lipids.<sup>29</sup> However, despite the enhanced stability and reduced permeability of GcGTPC-CH liposomes, the liposomes lacked the capability for accelerated release of intraliposomal content in response to an external stimulus, which could be advantageous for material-based technologies.

In order to incorporate stimuli-responsive functionality into GcGTPC-CH lipids, here we chose to integrate a disulfide linker near the polar headgroups of the lipid (**Figure 11a**) with the hypothesis that the relatively small addition of the disulfide outside of the hydrophobic core would not perturb membrane packing of the lipid,<sup>30</sup> whereas cleavable linkers that typically involve an addition of bulky aromatic groups or heteroatoms could affect lipid organization within the membrane.<sup>31–33</sup> Incorporation of the disulfides near the polar lipid headgroups, rather than



within the hydrophobic portion of the lipid, would also presumably facilitate access of free thiols to the disulfide bond for triggered response of the lipid.



After confirming GcGT(S-S)PC-CH lipids formed stable liposomes in aqueous buffer (**Figure 11b**), we next probed whether the addition of disulfide bonds to the lipid scaffold affected liposomal stability in serum containing buffer by using a self-quenching leakage assay of encapsulated carboxyfluorescein (CF).<sup>34</sup> Results showed that the addition of disulfide bonds to the lipid scaffold in GcGT(S-S)PC-CH did not affect stability in serum when compared to liposomes made with GcGTPC-CH (a similar lipid that does not contain disulfide bonds) (**Figure 11c**). In contrast, liposomes made with the conventional diacyl lipid POPC had released ~80% of CF within 2 hours, suggesting liposomal membrane destabilization in the presence of serum. As expected, a dose dependent leakage of CF was observed when a reducing agent DTT, was added to the liposomal suspension (**Figure 11d**). The release of the liposomal cargo is probably caused by the destabilization of the liposomes after cleavage of the polar lipid headgroup from the glycerol lipid backbone.

Liposomes made from pure disulfide-containing lipids can also be actively loaded with positively charged molecules such as doxorubicin (DOX) and can be used to release DOX upon addition of DTT (**Figure 11e**). These disulfide-containing liposomes loaded with DOX showed biocompatibility and superior release of DOX in living cells. This work represents a first step towards development of stimuli-responsive tetraether lipids, which may offer important

advantages of improved stability and reduced passive leakage of weakly basic and charged small molecules compared with current liposomal formulations used in bioenvironments. This work has been published in *Bioconjugate Chem.*, **2017**, 28 (8), 2041-2045.

### 3.8. Fusogenic properties of biomimetic membranes of Archaea-inspired lipids

Unique structural features of bipolar lipids (i.e. rings, headgroups, lipid tethering and ether bonds) are believed to be responsible for the important chemical and mechanical stabilities of Archaeal membranes. In addition of being less leaky than usual bilayer membranes, Archaeosomes have been reported to be nonfusogenic.<sup>3</sup> Therefore with the presence of tethered lipids, the formation of fusion intermediates is subject to higher energy barriers and greater geometrical constraints than in usual bilayer membranes.<sup>35</sup> However, fusion events have still been observed for certain lipid compositions by exposure to the combination of acidic pH, calcium and glycosidase.<sup>36,37</sup> Since most of Archaeal membranes are composed of a mixture of tetraether and diether lipids, it is believed that the fusogenic activity of Archaeosomes comes from the diether component. Therefore, we decided to explore whether liposomal membranes made of pure tetraether Archaea-inspired lipids can undergo fusion events.

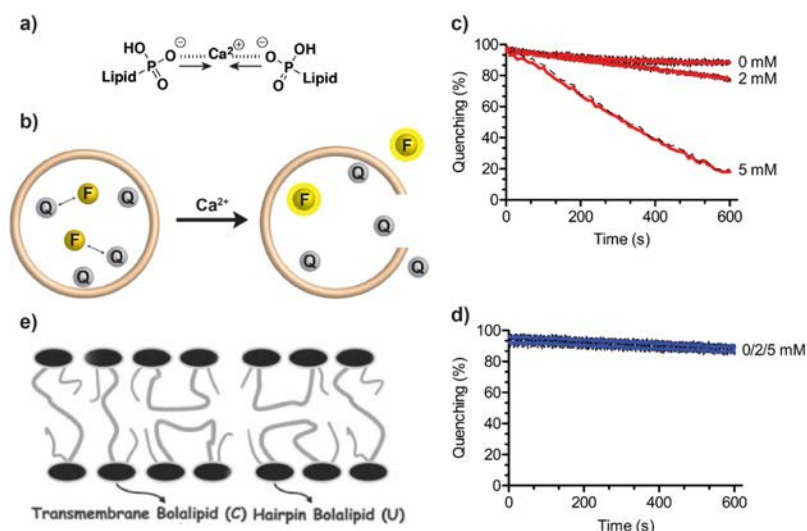


**Figure 12.** a) Schematic illustration of membrane fusion mediated by calcium ions through electrostatic attraction between two PA-lipids; b) Scheme of the content release assay based on the collisional quenching of the polyanionic fluorophore ANTS (F) by the cationic quencher DPX (Q); c-d) Liposomes consisted of Egg-PA (c) or GMGTPA (d) containing both ANTS (20 mM) and DPX (45 mM) were mixed and content release was monitored with 0, 2 and 5 mM Ca<sup>2+</sup> concentrations. All experiments were carried at room

temperature in TES buffer with 50  $\mu$ M of total lipid concentration. Error bars: s.d. (N=3); e) Schematic representation of tetraether lipids with transmembrane (C) and hairpin (U) conformations.

For the purpose of our work, we focused our attention on divalent cation-induced phosphatidic acid (PA) membrane fusion. While the negative charges of phosphate head group prevent aggregation by electrostatic repulsion in absence of divalent ions, Ca<sup>2+</sup> or Mg<sup>2+</sup> are known to promote membrane fusion through electrostatic attraction (**Figure 12a**). Thus, we have compared the membrane fusogenic properties of our previously made bipolar GMGTPA lipid with the commercial bilayer lipid Egg-PA by monitoring the mixing of membrane lipids and aqueous liposomal contents using.<sup>38</sup> It is noteworthy to mention that all experiments have been



conducted with small liposomes (diameter<100 nm) since particle size plays a crucial role in the rate of fusion. Indeed, small liposomes are more prone to fusion than larger liposomes due to stress coming from the high membrane curvature.

Our experiments showed that calcium-triggered liposomal lipid mixing and mixing content were observed for both tetraether and diacyl lipids. Using two different assays, we have shown that liposomes of tetraether lipids do undergo completely fusion but with a slower rate than bilayer membrane. In contrast to aggregation, liposome fusion is mostly accompanied by dramatic leakage resulting from membrane disruption and/or deformation (**Figure 12b**). This phenomenon has been observed for many bilayer systems displaying triggered fusion events (e.g. peptide, H<sup>+</sup>, Ca<sup>2+</sup>) (**Figure 12c**).<sup>39,40</sup> However we found that fusion with liposomes of GMGTPA undergo a non-leaky fusion process without membrane disruption and deformation (**Figure 12d**). Deuterated lipid analogs were synthesized and solid-state <sup>2</sup>H NMR spectroscopy experiments conducted to probe membrane structure and dynamics. We found that our synthetic tetraether lipids can adopt two configurations: a transmembrane configuration (C-shape) and an hairpin configuration (U-shape) (**Figure 12e**). We hypothesize that the observed fusion process for membrane of GMGTPA could be the result of bilayer microdomains formed by U-shape self-organized bipolar lipids. Our work not only gains insight in the stability of liposome of synthetic tetraether lipids, but also helps in the development of delivery vehicles with liposomes as the platform. A manuscript regarding this work is currently in preparation.

### 3.9. Application of archaea-inspired lipids as fluid nanopore coatings

One of the Mayer group's core competencies is protein analysis via single-molecule resistive-pulse sensing using lipid membrane-coated nanopores.<sup>1</sup> In much of our research, proteins are conjugated to lipid membranes to slow their translocation through the nanopore, lengthening the resistive pulses and allowing the acquisition of enough data to determine parameters such as protein shape.<sup>2</sup> As archaea-inspired tethered lipids diffuse much more slowly than untethered lipids,<sup>3</sup> we became interested in using them to coat nanopores.

We conducted a screening of a number of coating compositions, including DiPhyPC, Di-O-PhyPC, POPC membranes containing various proportions of cholesterol, a mixture of DOPC, DOPE, and LysoPC intended to more effectively coat rough or highly curved surfaces, and various proportions of tethered archaea-inspired lipids mixed with POPC. We found that tethered lipids easily formed stable coatings and allowed us to achieve the lowest lateral diffusion coefficients of any coating composition, even when they comprised only 50% of the total lipid mixture (**Figure 13**). Coating the pores with archaea-inspired lipids also increased the noise observed in the recording by a factor of only 1.2 on average, a favorable value compared to most other lipid compositions. A manuscript regarding this work is currently in preparation.

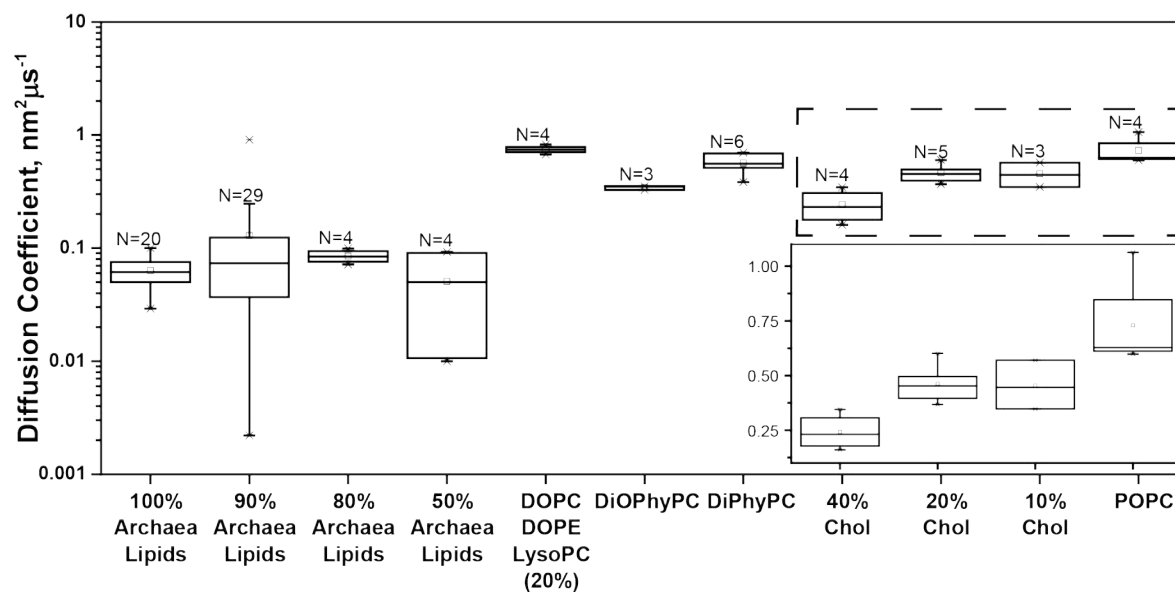


**Figure 13.** The lateral diffusion coefficient of various lipid compositions as measured by fluorescence recovery after photobleaching.

#### 4. Synthesis and evaluation of gramicidin A nanopores for the detection of small molecules

Methods to detect small molecular analytes (< 600-700 molecular weight<sup>41</sup>) have found important use in applications including the development of new pharmaceuticals,<sup>42</sup> the elucidation of complex pathways in biological systems,<sup>43,44</sup> and the detection of biological warfare agents.<sup>45</sup> For example, methods to monitor the presence of small molecules involved in bacterial signaling pathways, biofilm formation, virulence,<sup>46</sup> or related to diseases such as heart failure, cancer, neurodegenerative disorders<sup>47,48</sup> could provide valuable insight into understanding their function in a biological system.<sup>49</sup> Additionally, the detection of small molecule analytes could serve a vital role to identify biological species (i.e. bacteria, viruses, or spores) in potential contaminated areas (i.e., air, water, food, or even human).<sup>50,51</sup> While ELISA<sup>52,53</sup>, electrochemical<sup>43,54,55</sup>, and surface spectroscopy-based<sup>56,57</sup> methods have been developed to detect the presence of small molecules in various types of samples, new sensing platforms are still needed to improve sensitivity, selectivity, portability, and cost.

To date, very few examples utilizing the insertion of transmembrane ion channels into lipid bilayers have been reported for the detection of small molecules, with most examples employing the use of natural nanopores formed by  $\alpha$ -hemolysin as the channel sensing element for detection of, e.g., cocaine,<sup>58</sup> antibiotics,<sup>59</sup> ATP-binding aptamers,<sup>60</sup> and second messenger inositol ( $IP_3$ ).<sup>61,62</sup> We<sup>63,64</sup> and others<sup>65–67</sup> have previously reported the use of gramicidin A (gA) peptides to detect molecular analytes in solution through modulation of macroscopic transmembrane current flux or through sensitized photoinactivation<sup>68</sup> of gA channels. As opposed to permanently open nanopore channels like  $\alpha$ -hemolysin,<sup>69,70</sup> gA partitions strongly into bilayers<sup>71,72</sup> and reversibly dimerizes to form transient nanopores. The frequency and conductance of gA channel events depends on various environmental parameters, and can be quantified using single channel recordings.<sup>63,73</sup> Furthermore, gA is commercially available in gram scale quantities and synthetic modifications can be made to the C-terminus while retaining its ion channel properties.<sup>74–79</sup> Gramicidin A can, therefore, be readily customized for detection of a variety of specific analytes.<sup>74,80–82</sup>

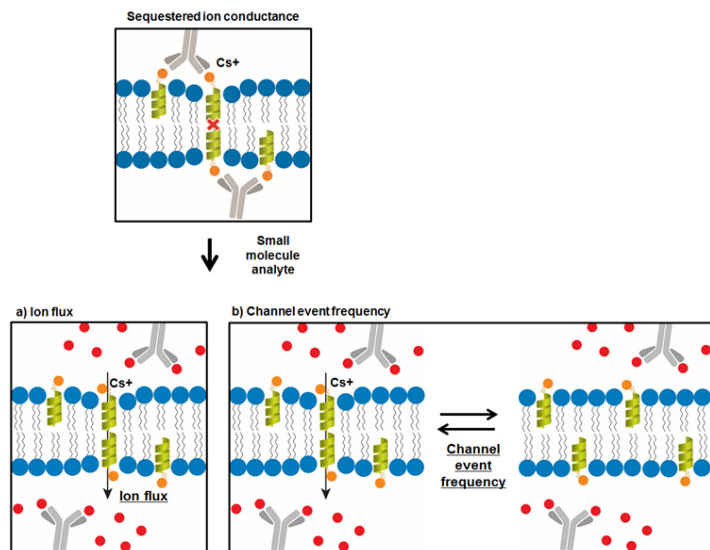


**Figure 14.** Schematic for the detection of small molecule analytes using engineered ion channel-forming peptides derived from gramicidin A (gA). Introduction of an antibody that binds to small molecules attached covalently to gA sequesters ion flux across a membrane. Upon introduction of a small molecule that competes with the gA derivative for binding to the antibody, two channel properties can be measured: a) the total ion flux (i.e., the total transported charge per time interval); and b) the frequency of observed single channel events; the magnitude of both of these channel properties is dependent on the

concentration of gramicidin derivatives able to form conducting ion channels.

We built upon these studies and report a novel method for the sensitive detection of small molecule analytes based on monitoring the frequency of single ion channel events from modified gramicidin channels. We exploit antibody-antigen interactions to suppress the ion channel activity of a derivative of gA that is modified with the antigen (i.e., the target small molecule analyte) at its C-terminus (**Figure 14**). Introduction of a sample of the free analyte in solution to a standard bilayer setup containing the gA-antibody complex restores ion channel activity upon competition of the analyte with the gA derivative for binding to the antibody. Detection of the analyte is accomplished using two methods: 1) measuring the total flux of charge transported across the membrane, or 2) measuring the frequency of single ion channel events as a function of concentration of analyte. This ion channel-based platform offers several advantages for the detection of small molecules compared to methods that are not based on ion channels: 1) this system utilizes the amplification characteristics of ion flux through a modified single ion channel to achieve high sensitivity,<sup>65,80,83,84</sup> 2) this approach employs high affinity antibody-antigen interactions to tailor detection towards a targeted small molecule analyte, 3) the ion channel-based platform requires small volumes (uL to mL) and quantities (picomolar to nanomolar concentrations) of ion channel peptides to achieve low cost,<sup>85</sup> and iv) the bilayer sensor setup is amenable to miniaturization making it possible to incorporate this small molecule detection assay into portable devices.<sup>86–91</sup>

We found that monitoring the frequency of gA channel events makes it possible to detect picomolar concentrations of small molecule in solution. In part, due to the digital on/off nature of frequency-based analysis, this approach is  $10^3$  times more sensitive than measuring macroscopic membrane ion flux through gA channels as a basis for detection. This novel methodology, therefore, significantly improves the limit of detection of nanopore-based sensors for small molecule analytes, which has the potential for incorporation into miniaturized and low cost devices that could complement current established assays. This work has been published in *Anal. Chem.*, **2017**, *in press*.

#### 4.1. An engineered melittin variant forms well-defined pores

In addition to gramicidin A, we also have sought to develop self-assembled oligomeric ion channels based on natural peptides to form large, stable pores in lipid membranes for improved signal amplification. New pore-forming peptides that yield large, stable nanopores are also potentially attractive for resistive-pulse sensing applications (potentially enabling the analysis of macromolecules larger than the inner diameter of  $\alpha$ -hemolysin or other known pore-formers) as well as targeted cell killing.

In 2014, Wiedman *et al.* reported the synthesis of a combinatorial library of pore-forming peptides based on melittin, the active ingredient of bee venom. Of this library, a peptide called MelP5 (**Figure 15**) emerged as a molecule that caused large increases in the conductivity of lipid membranes, as well as allowing the transit of macromolecules,<sup>1</sup> making it an attractive molecule for further investigation.

##### Melittin:

NH<sub>2</sub> – Gly – Ile – Gly – Ala – Val – Leu – Lys – Val – Leu – Thr – Thr – Gly – Leu – Pro – Ala – Leu – Ile – Ser – Trp – Ile – Lys – Arg – Lys – Arg – Gln – Gln – CONH<sub>2</sub>

##### MelP5:

NH<sub>2</sub> – Gly – Ile – Gly – Ala – Val – Leu – Lys – Val – Leu – **Ala** – Thr – Gly – Leu – Pro – Ala – Leu – Ile – Ser – Trp – Ile – Lys – **Ala** – **Ala** – **Gln** – Gln – **Leu** – CONH<sub>2</sub>

**Figure 15.** The primary sequences of melittin and MelP5. Altered amino acid residues are highlighted in red.

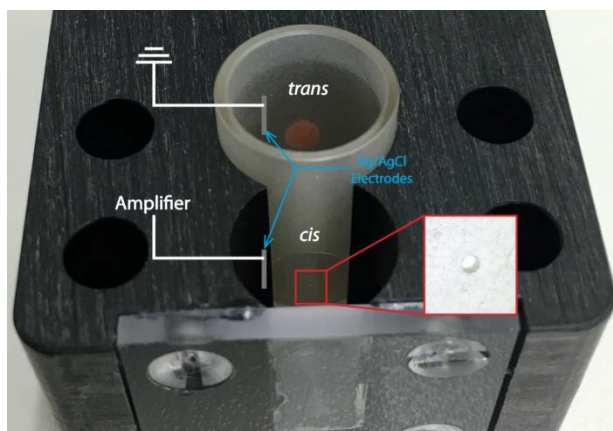


**Figure 16.** Experimental setup for MelP5 experiments. *Cis* and *trans* chambers were connected via a 150  $\mu$ m aperture, across which the membrane was painted. Voltage was applied to the *cis* compartment; the *trans* compartment was connected to ground.

We conducted the first electrophysiological analysis of single MelP5 pores in lipid membranes composed of 3:1 POPC:cholesterol that were painted across a small aperture (**Figure 16**) as described by Mueller *et al.*<sup>2</sup> We found that while melittin is capable of only poorly-defined disruptions of the membrane (**Figure 17a**), MelP5 can form ion channels with not only these random fluctuations (**Figure 17b**) but also discrete conductance values according to the “barrel-stave” model (**Figure 17c**). Additionally, MelP5 was found to be active at lower concentrations

(Figure 17a,b) and lower transmembrane voltages (Figure 17d,e) than melittin. Fits of conductance data according to models first described by Hall *et al.*<sup>3</sup> and Latorre and Alvarez<sup>4</sup> in the context of alamethicin pores yielded the estimate that melittin pores consist of 3 to 9 monomers on average, whereas Melp5 pores consist of 10 to 12 monomers on average.

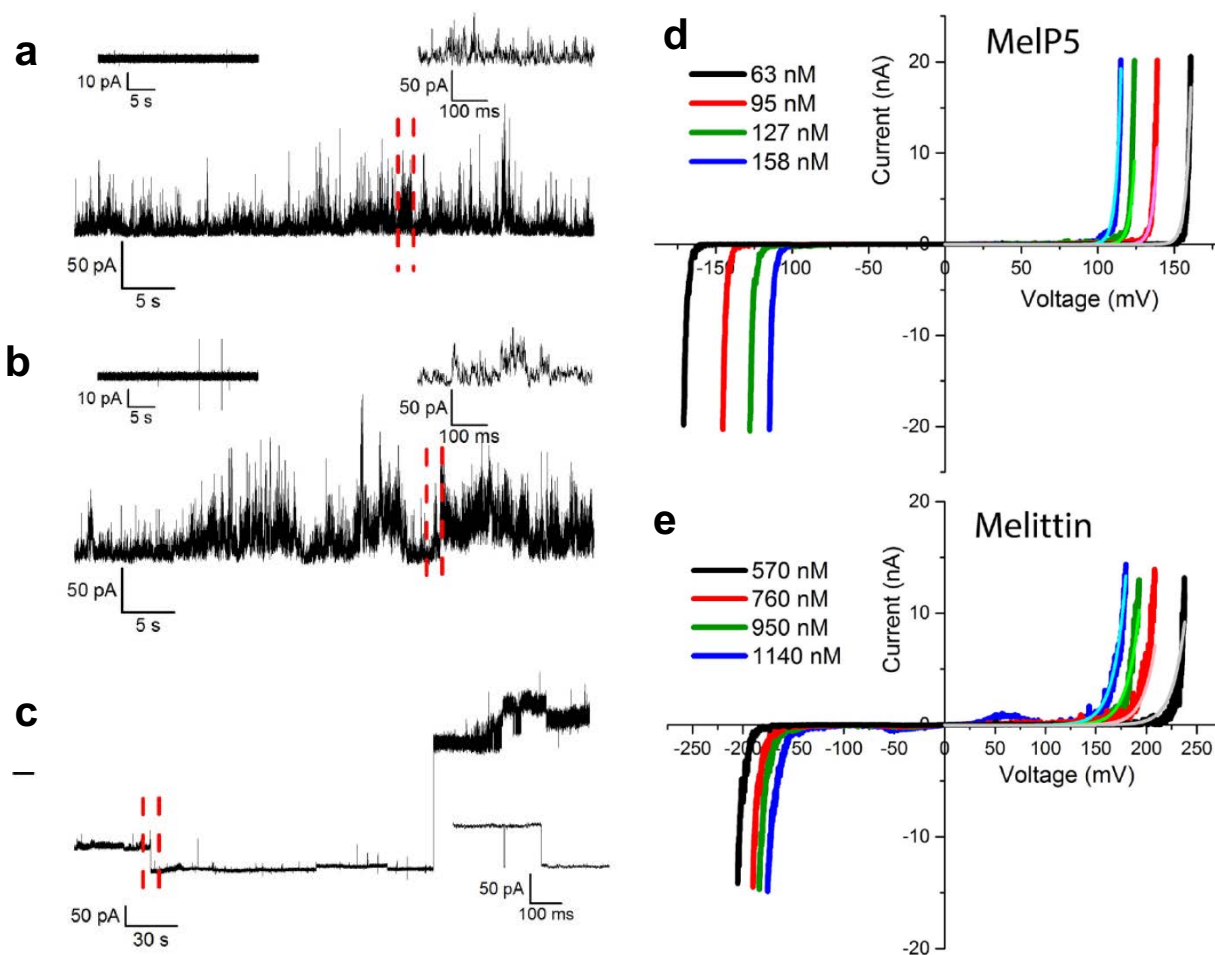


**Figure 17.** Comparison of pore formation by melittin and Melp5 in planar lipid bilayers composed of 3:1 POPC:cholesterol at an applied potential difference of +100 mV. (a) Current trace after the addition of melittin at a final concentration of 230 nM. (b) Current trace after the addition of Melp5 at a final concentration of 20 nM showing random, melittin-like activity. (c) Current trace after the addition of Melp5 at a final concentration of 80 nM showing defined conductance steps. (d) I-V curves of Melp5 at various concentrations. (e) I-V curves of melittin at various concentrations.

Finally, we modified the Melp5 peptide to include a dibenzocyclooctyne (DBCO) group at the C-terminus, allowing it to participate in “click” chemistry with lipids in the membrane bearing headgroups that contain azide moieties. In membranes composed of 99 mol% DiPhyPC and 1 mol% distearoylphosphoethanolamine lipids connected to an azide group via a PEG(2000) linker, the concentration of DBCO-modified Melp5 required to see activity at an applied voltage of 100 mV was only 1.9 nM, an order of magnitude lower than without “click” chemistry. Additionally, the “clicked” pores had a conductance that was invariant with applied voltage

(**Figure 18a**) and stable over long periods of time (**Figure 18b-d**), pointing to the utility of click chemistry in the formation of single stable pores in lipid membranes.

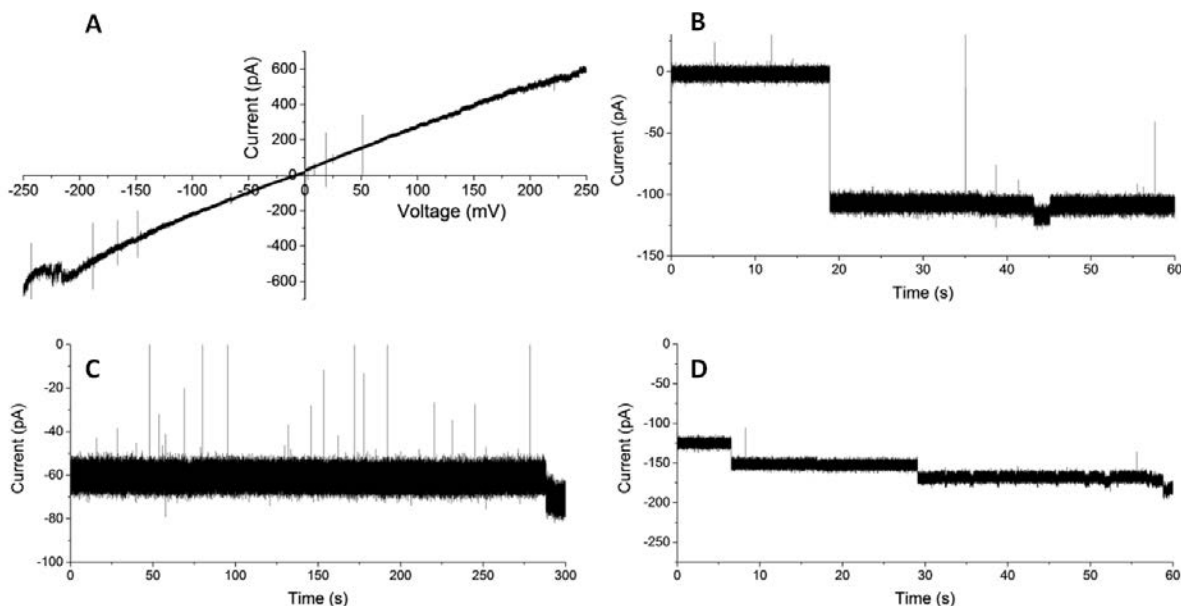


**Figure 18.** I-V curve (a) and current traces (b-d) of MeIP5-DBCO pores in an azide-laden DiPhyPC membrane. (a) Linear I-V curve shows a conductance invariant with applied voltage. (b) Current trace at 200 mV showing multiple pore insertions. (c,d) Current traces at -100 mV.

A manuscript regarding this work has been published in *BBA Biomembranes*, **2017**, 1859(10), 2051-2057.

#### 4.2. Another pore-forming peptide, Ceratotoxin A, displays alamethicin-like activity

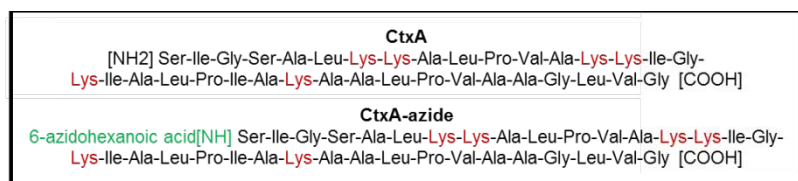


**Figure 19:** Sequences of the native CtxA peptide and its azide-modified variant.

In search of a molecule that more reliably formed pores of the barrel-stave type for easy attribution of current levels to oligomers of known size, we examined the activity of ceratotoxin A (CtxA), a 36-amino acid peptide that forms

alamethicin-like channels [1]. First, we looked at its pore-forming behavior in the presence of a lipid membrane by performing planar lipid bilayer recordings. We then attached an azide group to the peptide's N-terminus, which does not cross the membrane during pore formation.

**Figure 20** shows that, like native CtxA, CtxA-azide induces the well-defined step-wise current fluctuations expected from barrel-stave pore formation [2, 3]. The conductance values of each open state of the two peptides are very similar, confirming that the modification we made to this peptide did not affect its pore-forming capabilities. Next, we examined whether the in-situ conjugation of the CtxA-azide molecules to DBCO-bearing lipid head groups would occur spontaneously.



We studied and compared different characteristics of control and linkage experiments, such as the voltage- and concentration-dependence of pore formation and the conductance values of the open states of pores formed in the bilayer. For experiments where linkage between the peptide and the lipids is not possible (control experiments), we did not observe significant difference in the above-mentioned characteristics. In presence of membranes doped with 10 mol% of lipids carrying a DBCO moiety on their head group (linkage experiments), the click reaction between the DBCO and the azide of the modified peptide is possible [4]. Under these conditions, we show that CtxA-azide is able to produce well-defined activity even at 1 nM peptide concentration while the controls show no pore formation at the same concentration. Taken together, these results present evidence that this click reaction occurs at very low concentrations. We were initially concerned that the click reaction may not occur at all or only with reaction times beyond the lifetime of the bilayers as Cu-free click reactions are usually carried out at  $\mu\text{M}$  to  $\text{mM}$  concentrations [5-8].

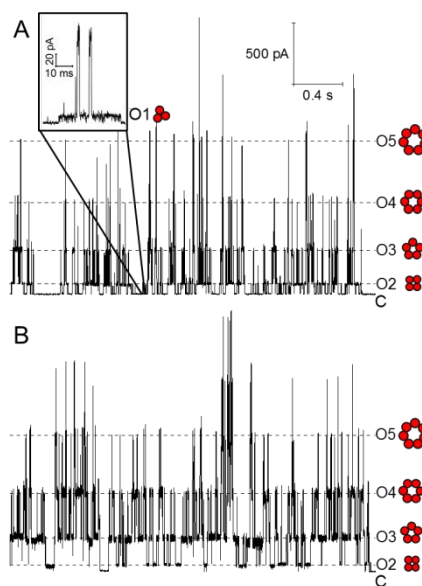


**Figure 20:** Comparison of pore formation by (A) CtxA and (B) CtxA-azide, showing well-defined activity. Peptide concentrations were (A) 20 nM and (B) 10 nM and the voltage was +180 mV.

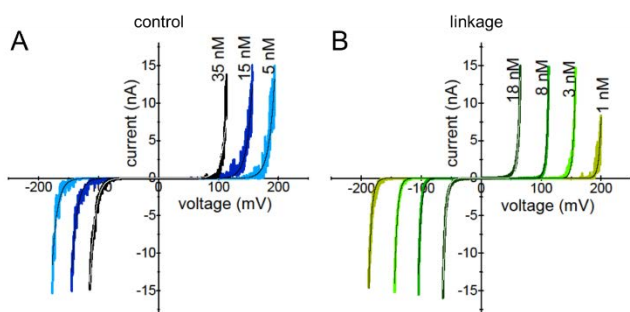


**Figure 21:** Comparison of the macroscopic currents measured as a function of applied voltage ramps (1 mV/s) for representative (A) control and (B) linkage experiments.

To investigate whether linkage of the peptide to the lipid membrane had an influence on the voltage dependency and the average number of monomers per pore of both peptides, we performed macroscopic conductance experiments in which multiple conducting pores are incorporated into the bilayer at the same time (**Figure 21**) [3]. The concentration-dependence of pore formation is different between linked and unlinked peptides, as a peptide concentration of 35 nM in the control experiment produces approximately the same curve as a peptide concentration of 8 nM in the linkage experiment. We found that the mean aggregation number  $n$  is similar between linkage ( $6.00 \pm 0.12$ ) and control experiments ( $5.82 \pm 0.02$ ), suggesting that the linkage does not influence the average number of peptides in a pore. We observe, however, a difference for the voltage dependence factor  $V_e$ , for which we found  $9.50 \pm 0.22$  mV for the control experiments and  $4.91 \pm 0.54$  mV for the linkage experiments. These values confirm that CtxA-azide has a stronger voltage dependency when linked to the bilayer, meaning that the energy that is needed to incorporate the peptide



into the bilayer is lower when the peptide is linked to the bilayer. We also concluded from these curves that CtxA-azide, when linked to a lipid bilayer is over 10 times more potent than the unlinked peptide. A manuscript regarding this work is currently in preparation.

#### 4.3. DNA-programmed assembly for formation of preferentially-sized pores

Following the promising results we obtained with the linkage of the CtxA peptide to a bilayer, we chose to again modify the CtxA peptide by adding an ssDNA to its N-terminus. As illustrated in **Figure 22**, the DNA strand covalently attached on the N-terminal side of the peptide is

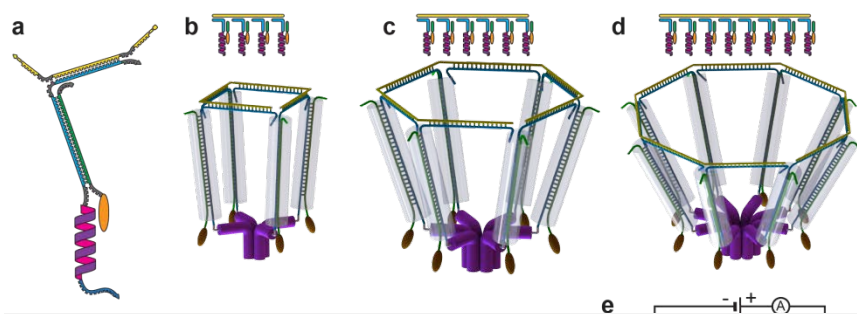


**Figure 22** Schematic representation of DNA-assembled peptide pores with programmable pore size. (a) CtxA-ssDNA (purple/blue) bound to a template strand (orange) and a spacer strand (green) bearing a cholesterol moiety. (b), (c) and (d) Schemes and projections of possible special arrangements of (b) a tetrameric, (c) a hexameric or (d) an octameric pore. (e) Scheme representing the experimental setup we use for measuring the insertions of these assemblies in planar lipid bilayers.

composed of two regions: a template-binding region and a spacer region. The latter region can hybridize to an additional DNA strand carrying a cholesterol moiety to localize it to the membrane surface (CtxA-dsDNA-chol) [9, 10]. By adding cholesterol, we lowered the concentration required for pore formation by a factor of 10 to 20. Adding a nucleic acid template with four, six or

eight hybridization sites for the peptide monomers led to the preferential formation of the corresponding assemblies (**Figure 23**). We also observed smaller assemblies that we attributed to templates that were not fully occupied. DNA templating decreased the concentration required to observe pore formation by an additional factor of ~10.

To optimize the system, we recently started to isolate our molecular assemblies using size exclusion chromatography [11]. The first results we obtained confirmed removal of free monomers (i.e. monomers not attached to a template), but we had to apply voltages above 250 mV to observe insertion of the assemblies in the membrane, compared to insertion voltages as low as 120 mV before purification. This behavior could be due to the presence of the fluorescent

dye that we added to the assemblies to detect them more precisely during the purification [12]. We are currently testing this hypothesis by purifying the same samples but devoid of any fluorescent dye. Another explanation could be that the free monomers are helping the larger assemblies to insert into the membrane.

Besides optimizing the templated assemblies of the peptides, another goal is to turn these peptides that form short-lived channels in membranes into long-lived pores that would be well suited for applications such as resistive pulse sensing or cell killing. To this end, we additionally modified the CtxA-ssDNA compounds on the C-terminal side of the peptide with an azide group. This group later reacts with a short nucleic acid consisting of 12 thymine bases bearing a DBCO moiety through a click reaction mechanism. This reaction yields a CtxA peptide covalently attached on both ends to a DNA strand (**Figure 19**). We hypothesized that this hydrophilic DNA segment might trap CtxA in a transmembrane conformation once the C-terminal section crosses the membrane. We found that this modification increases the typical lifetime of pores by ~3 orders of magnitude, from hundreds of milliseconds in the case of native CtxA to many minutes in the case of the DNA-CtxA-T<sub>12</sub> (**Figure 24**). A manuscript regarding this work is currently in preparation.

#### 4.4. Further work on Ceratotoxin A

As an alternative strategy to trigger the formation of ion channels, we assembled CtxA monomers using a streptavidin protein as a template [13, 14]. We used an azide-modified version of CtxA and reacted it with a DBCO-biotin. Addition of streptavidin resulted in an instantaneous increase in the current. We attribute this effect to streptavidin's four biotin binding sites, leading to the assembly of theoretically up to four monomers assembled together. The pore formation gradually increased over the course of two hours. As a control experiment, we then added a large excess of free biotin (~150-fold compared to CtxA-biotin) and, within 5 min, observed the expected decrease of the measured

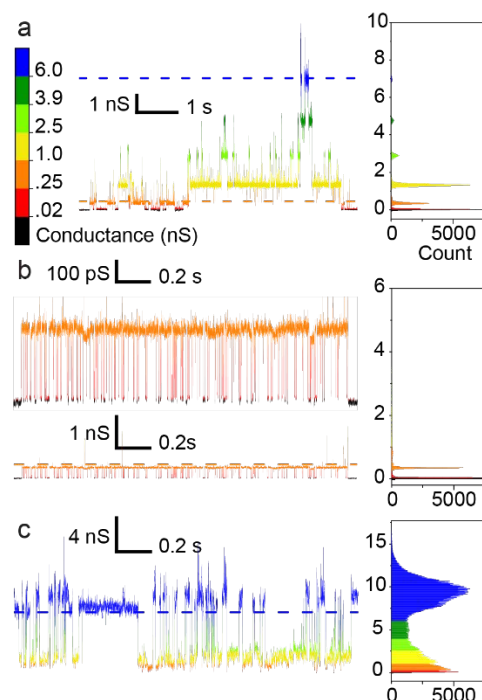


**Figure 23:** Current traces and corresponding histograms of template-assisted pore formation, in presence of (a) no template, (b) template 4-mer or (c) template 8-mer.

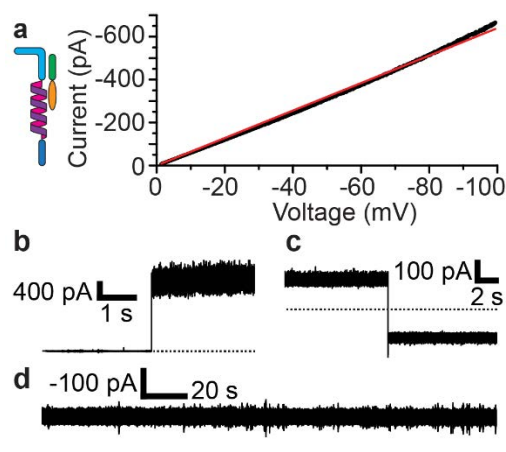


**Figure 24** Long-lived pore by DNA-double modified CtxA peptide. (a) Current-voltage relationship of a long-lived single channel. (b) Apparent single-step insertion of a single pore that remains in the membrane after reversal of the voltage polarity (c). (d) A 5-min current trace showing the presence of a pore formed by DNA-double modified CtxA monomers.

current to a level similar to the one observed before the addition of streptavidin. This strategy is a simple example of switchably templating monomers using an unmodified protein.

We observed another interesting result using a CtxA peptide covalently attached to an azide group on its N-terminal side and to a thiol group on the C-terminal side. We repeatedly observed pore formation at peptide concentrations as low as 30-50 pM. A low voltage was also sufficient (140 mV), which could indicate that this concentration could be further reduced when applying the voltage typically applied for native CtxA (180 mV). This concentration is almost 1000-fold lower than the concentration required to observe pore formation by native CtxA and may be due to the formation of dimers through disulfide bridges; we will test this hypothesis.

The next steps are to form larger assemblies using a 12-mer template as well as trying to form more well-defined and longer-lived pores in lipid membrane. One strategy will be the addition of a complementary polyA strand to the *trans* side of the membrane (*i.e.* the opposite side from where the CtxA peptide is added). Once we achieve this, we will try to observe the transport of macromolecules across templated pores as opposed to non-templated pores, as well as seeking pore-formers (peptides, proteins, toxins, etc) that might incorporate into membranes without requiring a transmembrane potential for insertion.

## References

- (1) Valentine, D. L. Adaptations to Energy Stress Dictate the Ecology and Evolution of the Archaea. *Nat. Rev. Microbiol.* **2007**, 5, 316–323.
- (2) Koga, Y. Thermal Adaptation of the Archaeal and Bacterial Lipid Membranes. *Archaea* **2012**, 2012, 1–6.
- (3) Chong, P. L. G.; Ayesa, U.; Prakash Daswani, V.; Hur, E. C. On Physical Properties of Tetraether Lipid Membranes: Effects of Cyclopentane Rings. *Archaea* **2012**, 2012.
- (4) Gabriel, J. L.; Lee Gau Chong, P. Molecular Modeling of Archaeobacterial Bipolar Tetraether Lipid Membranes. *Chem. Phys. Lipids* **2000**, 105 (2), 193–200.
- (5) Pearson, A.; Ingalls, A. E. Assessing the Use of Archaeal Lipids as Marine Environmental Proxies. *Annu. Rev. Earth Planet. Sci.* **2013**, 41 (1), 359–384.
- (6) Boyd, E. S.; Hamilton, T. L.; Wang, J.; He, L.; Zhang, C. L. The Role of Tetraether Lipid Composition in the Adaptation of Thermophilic Archaea to Acidity. *Front. Microbiol.* **2013**, 4 (April), 1–15.
- (7) Arakawa, K.; Eguchi, T.; Kakinuma, K. Highly Thermostable Liposome from 72-Membered Macrocyclic Tetraether Lipid: Importance of 72-Membered Lipid for Archaea to Thrive under Hyperthermal Environments. *Chem. Lett.* **2001**, No. 5, 440–441.
- (8) Arakawa, K.; Eguchi, T.; Kakinuma, K. 36-Membered Macrocyclic Diether Lipid Is Advantageous for Archaea to Thrive under the Extreme Thermal Environments. *Bull. Chem. Soc. Jpn.* **2001**, 74 (2), 347–356.
- (9) Shimada, H.; Nemoto, N.; Shida, Y.; Oshima, T.; Yamagishi, A. Effects of pH and Temperature on the Composition of Polar Lipids in *Thermoplasma Acidophilum* HO-62. *J. Bacteriol.* **2008**, 190 (15), 5404–5411.

- (10) Chong, P. L. G. Archaeobacterial Bipolar Tetraether Lipids: Physico-Chemical and Membrane Properties. *Chem. Phys. Lipids* **2010**, 163 (3), 253–265.
- (11) Koga, Y.; Morii, H. Biosynthesis of Ether-Type Polar Lipids in Archaea and Evolutionary Considerations. *Microbiol. Mol. Biol. Rev.* **2007**, 71 (1), 97–120.
- (12) Yamauchi, K.; Kinoshita, M. Highly Stable Lipid Membranes from Archaeobacterial Extremophiles. *Prog. Polym. Sci.* 1993, pp 763–804.
- (13) Mathai, J. C.; Tristram-Nagle, S.; Nagle, J. F.; Zeidel, M. L. Structural Determinants of Water Permeability through the Lipid Membrane. *J. Gen. Physiol.* **2007**, 131 (1), 69–76.
- (14) Jansen, M.; Blume, A. A Comparative Study of Diffusive and Osmotic Water Permeation across Bilayers Composed of Phospholipids with Different Head Groups and Fatty Acyl Chains. *Biophys. J.* **1995**, 68 (3), 997–1008.
- (15) Spooner, M. J.; Gale, P. A. Anion Transport across Varying Lipid Membranes – the Effect of Lipophilicity. *Chem. Commun.* **2015**, 51 (51), 4883–4886.
- (16) Allen, T. M.; Cullis, P. R. Liposomal Drug Delivery Systems: From Concept to Clinical Applications. *Adv. Drug Deliv. Rev.* **2013**, 65 (1), 36–48.
- (17) Yusko, E. C.; Johnson, J. M.; Majd, S.; Prangkio, P.; Rollings, R. C.; Li, J.; Yang, J.; Mayer, M. Controlling Protein Translocation through Nanopores with Bio-Inspired Fluid Walls. *Nat. Nanotechnol.* **2011**, 6 (4), 253–260.
- (18) Koyanagi, T.; Leriche, G.; Onofrei, D.; Holland, G. P.; Mayer, M.; Yang, J. Cyclohexane Rings Reduce Membrane Permeability to Small Ions in Archaea-Inspired Tetraether Lipids. *Angew. Chem., Int. Ed. Engl.* **2016**, 55 (5), 1890–1893.
- (19) Kovalova, L.; McCardell, C. S.; Hollender, J. Challenge of High Polarity and Low Concentrations in Analysis of Cytostatics and Metabolites in Wastewater by Hydrophilic Interaction Chromatography/tandem Mass Spectrometry. *J. Chromatogr. A* **2009**, 1216 (7), 1100–1108.
- (20) Cavallito, J. C.; Nichol, C. A.; Brenckman, W. D.; Deangelis, R. L.; Stickney, D. R.; Simmons, W. S.; Sigel, C. W. Lipid-Soluble Inhibitors of Dihydrofolate Reductase. I. Kinetics, Tissue Distribution, and Extent of Metabolism of Pyrimethamine, Metoprine, and Etoprine in the Rat, Dog, and Man. *Drug Metab. Dispos.* **1978**, 6 (3), 329–337.
- (21) Lasic, D. D. Liposomes: From Physics to Applications. Elsevier 1993, p Chap 2.
- (22) Waterhouse, D. N.; Madden, T. D.; Cullis, P. R.; Bally, M. B.; Mayer, L. D.; Webb, M. S. Preparation, Characterization, and Biological Analysis of Liposomal Formulations of Vincristine. *Method Enzym.* **2005**, 391 (SPEC. ISS.), 40–57.
- (23) Leriche, G.; Cifelli, J. L.; Sibucão, K. C.; Patterson, J. P.; Koyanagi, T.; Gianneschi, N. C.; Yang, J. Characterization of Drug Encapsulation and Retention in Archaea-Inspired Tetraether Liposomes. *Org. Biomol. Chem.* **2017**, 15 (10), 2157–2162.
- (24) Lipinski, C. A.; Lombardo, F.; Dominy, B. W.; Feeney, P. J. Experimental and Computational Approaches to Estimate Solubility and Permeability in Drug Discovery and Development Settings. *Adv. Drug Del. Rev.* **1997**, 23, 3–25.
- (25) Papahadjopoulos, D.; Nir, S.; Oki, S. Permeability Properties of Phospholipid Membranes: Effect of Cholesterol and Temperature. *Biochim. Biophys. Acta - Biomembr.* **1972**, 266 (3), 561–583.

- (26) Haines, T. H. Do Sterols Reduce Proton and Sodium Leaks through Lipid Bilayers? *Prog. Lipid Res.* **2001**, *40* (4), 299–324.
- (27) Sułkowski, W. W.; Pentak, D.; Nowak, K.; Sułkowska, A. The Influence of Temperature, Cholesterol Content and pH on Liposome Stability. *J. Mol. Struct.* **2005**, *744–747*, 737–747.
- (28) Huang, Z.; Szoka Jr., F. C. Sterol-Modified Phospholipids: Cholesterol and Phospholipid Chimeras with Improved Biomembrane Properties. *J. Am. Chem. Soc.* **2008**, *130* (46), 15702–15712.
- (29) Koyanagi, T.; Cao, K. J.; Leriche, G.; Onofrei, D.; Holland, G. P.; Mayer, M.; Sept, D.; Yang, J. Hybrid Lipids Inspired by Extremophiles and Eukaryotes Afford Serum-Stable Membranes with Low Leakage. *Chem. Eur. J.* **2017**, *23* (28), 6757–6762.
- (30) Koyanagi, T.; Leriche, G.; Yep, A.; Onofrei, D.; Holland, G. P.; Mayer, M.; Yang, J. Effect of Headgroups on Small-Ion Permeability across Archaea-Inspired Tetraether Lipid Membranes. *Chem. Eur. J.* **2016**, *22* (24), 8074–8077.
- (31) De Gracia Lux, C.; Joshi-Barr, S.; Nguyen, T.; Mahmoud, E.; Schopf, E.; Fomina, N.; Almutairi, A. Biocompatible Polymeric Nanoparticles Degrade and Release Cargo in Response to Biologically Relevant Levels of Hydrogen Peroxide. *J. Am. Chem. Soc.* **2012**, *134* (38), 15758–15764.
- (32) Barbeau, J.; Belmadi, N.; Montier, T.; Le Gall, T.; Dalençon, S.; Lemiègre, L.; Benvegnu, T. Synthesis of a Novel Archaeal Tetraether-Type Lipid Containing a Diorthoester Group as a Helper Lipid for Gene Delivery. *Tetrahedron Lett.* **2016**, *57* (27–28), 2976–2980.
- (33) Mueller, A.; Bondurant, B.; O'Brien, D. F. Visible-Light-Stimulated Destabilization of PEG-Liposomes. *Macromolecules* **2000**, *33* (13), 4799–4804.
- (34) Weinstein, J.; Yoshikami, S.; Henkart, P.; Blumenthal, R.; Hagins, W. Liposome-Cell Interaction: Transfer and Intracellular Release of a Trapped Fluorescent Marker. *Science* **1977**, *195* (4277), 489–492.
- (35) Gliozzi, A.; Relini, A.; Chong, P. L. G. Structure and Permeability Properties of Biomimetic Membranes of Bolaform Archaeal Tetraether Lipids. *J. Membr. Sci.* **2002**, *206* (1–2), 131–147.
- (36) Relini, A.; Cassinadri, D.; Fan, Q.; Gulik, A.; Mirghani, Z.; De Rosa, M.; Gliozzi, A. Effect of Physical Constraints on the Mechanisms of Membrane Fusion: Bolaform Lipid Vesicles as Model Systems. *Biophys. J.* **1996**, *71* (4), 1789–1795.
- (37) Relini, A.; Cassinadri, D.; Mirghani, Z.; Brandt, O.; Gambacorta, A.; Trincone, A.; De Rosa, M.; Gliozzi, A. Calcium-Induced Interaction and Fusion of Archaeobacterial Lipid Vesicles: A Fluorescence Study. *Biochim. Biophys. Acta - Biomembr.* **1994**, *1194* (1), 17–24.
- (38) Düzgüneş, N.; Faneca, H.; Lima, M. C. Methods to Monitor Liposome Fusion, Permeability, and Interaction with Cells. *Methods Mol Biol.* **2010**, *606*, 209–232.
- (39) Xia, Y.; Sun, J.; Liang, D. Aggregation, Fusion, and Leakage of Liposomes Induced by Peptides. *Langmuir* **2014**, *30* (25), 7334–7342.
- (40) Ellens, H.; Bentz, J.; Szoka, F. C. H<sup>+</sup>- and Ca<sup>2+</sup>-Induced Fusion and Destabilization of Liposomes. *Biochemistry* **1985**, *24*, 3099–3106.
- (41) Thompson, L. A.; Ellman, J. A. Synthesis and Applications of Small Molecule Libraries. *Chem. Rev.* **1996**, *96*, 555–600.
- (42) Zhang, J.; Yang, P. L.; Gray, N. S. Targeting Cancer with Small Molecule Kinase Inhibitors. *Nat. Rev. Cancer*

2009, 9, 28–39.

- (43) Wang, W. U.; Chen, C.; Lin, K.; Fang, Y.; Lieber, C. M. Label-Free Detection of Small-Molecule-Protein Interactions by Using Nanowire Nanosensors. *Proc. Natl. Acad. Sci. U. S. A.* **2005**, *102*, 3208–3212.
- (44) Strausberg, R. L. From Knowing to Controlling: A Path from Genomics to Drugs Using Small Molecule Probes. *Science* **2003**, *300*, 294–295.
- (45) Rao, S. S.; Mohan, K. V. K.; Atreya, C. D. Detection Technologies for Bacillus Anthracis: Prospects and Challenges. *J. Microbiol. Methods* **2010**, *82*, 1–10.
- (46) Camilli, A.; Bassler, B. L. Bacterial Small-Molecule Signaling Pathways. *Science* **2006**, *311*, 1113–1116.
- (47) Kenakin, T.; Christopoulos, A. Signalling Bias in New Drug Discovery: Detection, Quantification and Therapeutic Impact. *Nat. Rev. Drug. Discov.* **2013**, *12*, 205–216.
- (48) Holliger, P.; Hudson, P. J. Engineered Antibody Fragments and the Rise of Single Domains. *Nat. Biotech.* **2005**, *23*, 1126–1136.
- (49) Mayer, M.; Semetey, V.; Gitlin, I.; Yang, J.; Whitesides, G. M. Using Ion Channel-Forming Peptides to Quantify Protein-Ligand Interactions. *J. Am. Chem. Soc.* **2008**, *130*, 1453–1465.
- (50) Gooding, J. J. Biosensor Technology for Detecting Biological Warfare Agents: Recent Progress and Future Trends. *Anal. Chim. Acta* **2006**, *559*, 137–151.
- (51) Fitch, J. P.; Raber, E.; Imbro, D. R. Technology Challenges in Responding to Biological or Chemical Attacks in the Civilian Sector. *Science* **2003**, *302*, 1350–1354.
- (52) Schon, M.; Bong, A. B.; Drewniok, C.; Herz, J.; Geilen, C. C.; Reifemberger, J.; Benninghoff, B.; Slade, H. B.; Gollnick, H.; Schon, M. P. Tumor-Selective Induction of Apoptosis and the Small-Molecule Immune Response Modifier Imiquimod. *J. Natl. Cancer Inst.* **2003**, *95*, 1138–1149.
- (53) Li, D.; Ying, Y.; Wu, J.; Niessner, R.; Knopp, D. Comparison of Monomeric and Polymeric Horseradish Peroxidase as Labels in Competitive ELISA for Small Molecule Detection. *Microchim. Acta* **2013**, *180*, 711–717.
- (54) Baker, B. R.; Lai, R. Y.; Wood, M. S.; Doctor, E. H.; Heeger, A. J.; Plaxco, K. W. An Electronic, Aptamer-Based Small-Molecule Sensor for the Rapid, Label-Free Detection of Cocaine in Adulterated Samples and Biological Fluids. *J. Am. Chem. Soc.* **2006**, *128*, 3138–3139.
- (55) Lai, L. M. H.; Goon, I. Y.; Chuah, K.; Lim, M.; Braet, F.; Amal, R.; Gooding, J. J. The Biochemiresistor: An Ultrasensitive Biosensor for Small Organic Molecules. *Angew. Chem., Int. Ed.* **2012**, *51*, 6456–6459.
- (56) Shankaran, D. R.; Gobi, K. V.; Miura, N. Recent Advancements in Surface Plasmon Resonance Immunosensors for Detection of Small Molecules of Biomedical, Food and Environmental Interest. *Sensors Actuators, B Chem.* **2007**, *121*, 158–177.
- (57) Matsui, J.; Akamatsu, K.; Hara, N.; Miyoshi, D.; Nawafune, H.; Tamaki, K.; Sugimoto, N. SPR Sensor Chip for Detection of Small Molecules Using Molecularly Imprinted Polymer with Embedded Gold Nanoparticles. *Anal. Chem.* **2005**, *77*, 4282–4285.
- (58) Kawano, R.; Osaki, T.; Sasaki, H.; Takinoue, M.; Yoshizawa, S.; Takeuchi, S. Rapid Detection of a Cocaine-Binding Aptamer Using Biological Nanopores on a Chip. *J. Am. Chem. Soc.* **2011**, *133*, 8474–8477.
- (59) Asandei, A.; Apetrei, A.; Luchian, T. Uni-Molecular Detection and Quantification of Selected  $\beta$ -Lactam

- Antibiotics with a Hybrid  $\alpha$ -Hemolysin Protein Pore. *J. Mol. Recognit.* **2011**, *24*, 199–207.
- (60) Ying, Y.-L.; Wang, H.-Y.; Sutherland, T. C.; Long, Y.-T. Monitoring of an ATP-Binding Aptamer and Its Conformational Changes Using an  $\alpha$ -Hemolysin Nanopore. *Small* **2011**, *7*, 87–94.
  - (61) Kang, X.; Cheley, S.; Rice-Ficht, A. C.; Bayley, H. A Storable Encapsulated Bilayer Chip Containing a Single Protein Nanopore. *J. Am. Chem. Soc.* **2007**, *129*, 4701–4705.
  - (62) Cheley, S.; Gu, L.-Q.; Bayley, H. Stochastic Sensing of Nanomolar Inositol 1,4,5-Trisphosphate with an Engineered Pore. *Chem. Biol.* **2002**, *9* (7), 829–838.
  - (63) Macrae, M. X.; Blake, S.; Jiang, X.; Capone, R.; Estes, D. J.; Mayer, M.; Yang, J. A Semi-Synthetic Ion Channel Platform for Detection of Phosphatase and Protease Activity. *ACS Nano* **2009**, *3*, 3567–3580.
  - (64) Majd, S.; Yusko, E. C.; Yang, J.; Sept, D.; Mayer, M. A Model for the Interfacial Kinetics of Phospholipase D Activity on Long-Chain Lipids. *Biophys. J.* **2013**, *105*, 146–153.
  - (65) Futaki, S.; Zhang, Y.; Kiwada, T.; Nakase, I.; Yagami, T.; Oiki, S.; Sugiura, Y. Gramicidin-Based Channel Systems for the Detection of Protein-Ligand Interaction. *Bioorg. Med. Chem.* **2004**, *12*, 1343–1350.
  - (66) Antonenko, Y. N.; Rokitskaya, T. I.; Kotova, E. A.; Reznik, G. O.; Sano, T.; Cantor, C. R. Effect of Streptavidins with Varying Biotin Binding Affinities on the Properties of Biotinylated Gramicidin Channels. *Biochemistry* **2004**, *43*, 4575–4582.
  - (67) Borisenko, V.; Zhang, Z.; Woolley, G. A. Gramicidin Derivatives as Membrane-Based pH Sensors. *Biochim. Biophys. Acta - Biomembr.* **2002**, *1558*, 26–33.
  - (68) Rokitskaya, T. I.; Macrae, M. X.; Blake, S.; Egorova, N. S.; Kotova, E. a; Yang, J.; Antonenko, Y. N. Mechanistic Insight into Gramicidin-Based Detection of Protein-Ligand Interactions via Sensitized Photoinactivation. *J. Phys. Condens. Matter* **2010**, *22*, 454118.
  - (69) Astier, Y.; Braha, O.; Bayley, H. Toward Single Molecule DNA Sequencing: Direct Identification of Ribonucleoside and Deoxyribonucleoside 5'-Monophosphates by Using an Engineered Protein Nanopore Equipped with a Molecular Adapter. *J. Am. Chem. Soc.* **2006**, *128*, 1705–1710.
  - (70) Wang, G.; Wang, L.; Han, Y.; Zhou, S.; Guan, X. Nanopore Stochastic Detection: Diversity, Sensitivity, and beyond. *Acc. Chem. Res.* **2013**, *46*, 2867–2877.
  - (71) Hladky, S. B.; Haydon, D. A. Ion Transfer across Lipid Membranes in the Presence of Gramicidin A. I. Studies of the Unit Conductance Channel. *Biochim. Biophys. Acta - Biomembr.* **1972**, *274*, 294–312.
  - (72) Finkelstein, A.; Andersen, O. S. The Gramicidin a Channel: A Review of Its Permeability Characteristics with Special Reference to the Single-File Aspect of Transport. *J. Membr. Biol.* **1981**, *59*, 155–171.
  - (73) Lundbæk, J. A. Regulation of Membrane Protein Function by Lipid Bilayer Elasticity-a Single Molecule Technology to Measure the Bilayer Properties Experienced by an Embedded Protein. *J. Phys. Condens. Matter* **2006**, *18*, S1305-44.
  - (74) Blake, S.; Capone, R.; Mayer, M.; Yang, J. Chemically Reactive Derivatives of Gramicidin A for Developing Ion Channel-Based Nanopores. *Bioconjug. Chem.* **2008**, *19*, 1614–1624.
  - (75) Bali, D.; King, L.; Kim, S. Syntheses of New Gramicidin a Derivatives. *Aust. J. Chem.* **2003**, *56*, 293–300.
  - (76) Antonenko, Y. N.; S. Gluhov, G.; M. Firsov, A.; D. Pogozeva, I.; Kovalchuk, S. I.; V. Pechnikova, E.; Kotova, E. A.; S. Sokolova, O. Gramicidin A Disassembles Large Conductive Clusters of Its Lysine-Substituted

Derivatives in Lipid Membranes. *Phys. Chem. Chem. Phys.* **2015**, *17*, 17461–17470.

- (77) Fields, G. B.; Fields, C. G.; Petefish, J.; Van Wart, H. E.; Cross, T. A. Solid-Phase Peptide Synthesis and Solid-State NMR Spectroscopy of [Ala3-15N][Val1]gramicidin A. *Proc. Natl. Acad. Sci. U. S. A.* **1988**, *85*, 1384–1388.
- (78) Macrae, M. X.; Blake, S.; Mayer, M.; Yang, J. Nanoscale Ionic Diodes with Tunable and Switchable Rectifying Behavior. *J. Am. Chem. Soc.* **2010**, *132*, 1766–1767.
- (79) Macrae, M. X.; Schlamadinger, D.; Kim, J. E.; Mayer, M.; Yang, J. Using Charge to Control the Functional Properties of Self-Assembled Nanopores in Membranes. *Small* **2011**, *7*, 2016–2020.
- (80) Capone, R.; Blake, S.; Restrepo, M. R.; Yang, J.; Mayer, M. Designing Nanosensors Based on Charged Derivatives of Gramicidin A. *J. Am. Chem. Soc.* **2007**, *129*, 9737–9745.
- (81) Suarez, E.; Emmanuelle, E. D.; Molle, G.; Lazaro, R.; Viallefont, P. Synthesis and Characterization of a New Biotinylated Gramicidin. *J. Pept. Sci.* **1998**, *4*, 371–377.
- (82) Cornell, B. a; Braach-Maksvytis, V. L.; King, L. G.; Osman, P. D.; Raguse, B.; Wieczorek, L.; Pace, R. J. A Biosensor That Uses Ion-Channel Switches. *Nature* **1997**, *387*, 580–583.
- (83) Sakai, N.; Matile, S. Synthetic Ion Channels. *Langmuir* **2013**, *29*, 9031–9040.
- (84) Xin, P.; Zhu, P.; Su, P.; Hou, J. L.; Li, Z. T. Hydrogen-Bonded Helical Hydrazide Oligomers and Polymer That Mimic the Ion Transport of Gramicidin a. *J. Am. Chem. Soc.* **2014**, *136*, 13078–13081.
- (85) Tonooka, T.; Sato, K.; Osaki, T.; Kawano, R.; Takeuchi, S. Lipid Bilayers on a Picoliter Microdroplet Array for Rapid Fluorescence Detection of Membrane Transport. *Small* **2014**, *10*, 3275–3282.
- (86) Bayley, H.; Cremer, P. S. Stochastic Sensors Inspired by Biology. *Nature* **2001**, *413*, 226–230.
- (87) White, R. J.; Ervin, E. N.; Yang, T.; Chen, X.; Daniel, S.; Cremer, P. S.; White, H. S. Single Ion-Channel Recordings Using Glass Nanopore Membranes. *J. Am. Chem. Soc.* **2007**, *129*, 11766–11775.
- (88) Chun, K.-Y.; Son, Y. J.; Han, C.-S. Highly Sensitive and Patchable Pressure Sensors Mimicking Ion-Channel-Engaged Sensory Organs. *ACS Nano* **2016**, *10*, 4550–4558.
- (89) Rosenstein, J. K.; Ramakrishnan, S.; Roseman, J.; Shepard, K. L. Single Ion Channel Recordings with CMOS-Anchored Lipid Membranes. *Nano Lett.* **2013**, *13*, 2682–2686.
- (90) Del Rio Martinez, J. M.; Zaitseva, E.; Petersen, S.; Baaken, G.; Behrends, J. C. Automated Formation of Lipid Membrane Microarrays for Ionic Single-Molecule Sensing with Protein Nanopores. *Small* **2015**, *11* (1), 119–125.
- (91) Funakoshi, K.; Suzuki, H.; Takeuchi, S. Lipid Bilayer Formation by Contacting Monolayers in a Microfluidic Device for Membrane Protein Analysis. *Anal. Chem.* **2006**, *78*, 8169–8174.
- (92) Konings, W. N.; Albers, S.-V.; Koning, S.; Driessen, A. J. M. *Antonie Van Leeuwenhoek* **2002**, *81* (1–4), 61.
- (93) Baker-Austin, C.; Dopson, M. *Trends Microbiol.* **2007**, *15* (4), 165.
- (94) Paula, S.; Volkov, A. G.; Van Hoek, A. N.; Haines, T. H.; Deamer, D. W. *Biophys. J.* **1996**, *70* (1), 339.
- (95) Nichols, J. W.; Deamer, D. W. *Proc. Natl. Acad. Sci. U. S. A.* **1980**, *77* (4), 2038.
- (96) Nagle, J. F. *J. Bioenerg. Biomembr.* **1987**, *19* (5), 413.



- (97) Deamer, D. W.; Nichols, J. W. *J. Membr. Biol.* **1989**, 107 (2), 91.
- (98) Nichols, J. W.; Abercrombie, R. F. *J. Membr. Biol.* **2010**, No. 237, 21.
- (99) Komatsu, H.; Chong, P. L. *Biochemistry (Mosc.)* **1998**, 37 (1), 107.
- (100) Wiedman, G.; Fuselier, T.; He, J.; Searson, P. C.; Hristova, K.; Wimley, W. C. *J. Am. Chem. Soc.* **2014**, 136 (12), 4724.
- (101) Mueller, P.; Rudin, D. O.; Tien, H. T.; Wescott, W. C. *Nature* **1962**, 194 (4832), 979.
- (102) Hall, J. E.; Vodyanoy, I.; Balasubramanian, T. M.; Marshall, G. R. *Biophys. J.* **1984**, 45 (1), 233.
- (103) Latorre, R.; Alvarez, O. *Physiol. Rev.* **1981**, 61 (1), 77.
- (104) N. Saint, L. Marri, D. Marchini, G. Molle, The antibacterial peptide ceratotoxin A displays alamethicin-like behavior in lipid bilayers, *Peptides*, 24 (2003) 1779-1784.
- (105) G. Boheim, Statistical analysis of alamethicin channels in black lipid membranes, *The Journal of Membrane Biology*, 19 (1974) 277-303.
- (106) J.E. Hall, I. Vodyanoy, T.M. Balasubramanian, G.R. Marshall, Alamethicin. A rich model for channel behavior, *Biophysical Journal*, 45 (1984) 233-247.
- (107) J.C. Jewett, E.M. Sletten, C.R. Bertozzi, Rapid Cu-Free Click Chemistry with Readily Synthesized Biarylazacyclooctynones, *Journal of the American Chemical Society*, 132 (2010) 3688-3690.
- (108) J.M. Baskin, J.A. Prescher, S.T. Laughlin, N.J. Agard, P.V. Chang, I.A. Miller, A. Lo, J.A. Codelli, C.R. Bertozzi, Copper-free click chemistry for dynamic in vivo imaging, *Proceedings of the National Academy of Sciences*, 104 (2007) 16793-16797.
- (109) S.T. Laughlin, J.M. Baskin, S.L. Amacher, C.R. Bertozzi, In vivo imaging of membrane-associated glycans in developing zebrafish, *Science*, 320 (2008) 664-667.
- (110) J.A. Codelli, J.M. Baskin, N.J. Agard, C.R. Bertozzi, Second-generation difluorinated cyclooctynes for copper-free click chemistry, *Journal of the American Chemical Society*, 130 (2008) 11486-11493.
- (111) P.V. Chang, J.A. Prescher, E.M. Sletten, J.M. Baskin, I.A. Miller, N.J. Agard, A. Lo, C.R. Bertozzi, Copper-free click chemistry in living animals, *Proceedings of the National Academy of Sciences*, 107 (2010) 1821-1826.
- (112) M. Langecker, V. Arnaut, T.G. Martin, J. List, S. Renner, M. Mayer, H. Dietz, F.C. Simmel, Synthetic lipid membrane channels formed by designed DNA nanostructures, *Science*, 338 (2012) 932-936.
- (113) J.R. Burns, K. Gopfrich, J.W. Wood, V.V. Thacker, E. Stulz, U.F. Keyser, S. Howorka, Lipid-bilayer-spanning DNA nanopores with a bifunctional porphyrin anchor, *Angewandte Chemie (International ed. in English)*, 52 (2013) 12069-12072.
- (114) S. Mori, H.G. Barth, *Size exclusion chromatography*, Springer Science & Business Media, 2013.
- (115) L.D. Hughes, R.J. Rawle, S.G. Boxer, Choose Your Label Wisely: Water-Soluble Fluorophores Often Interact with Lipid Bilayers, *PLOS ONE*, 9 (2014) e87649.
- (116) Y. Zhang, S. Futaki, T. Kiwada, Y. Sugiura, Detection of protein–Ligand interaction on the membranes using C-Terminus biotin-Tagged alamethicin, *Bioorganic & Medicinal Chemistry*, 10 (2002) 2635-2639.
- (117) S. Futaki, Z. Youjun, Y. Sugiura, Detecting a tag on a channel opening: blockage of the biotinylated channels by streptavidin, *Tetrahedron Letters*, 42 (2001) 1563-1565.

## 5. Hydrogel-based reverse-electrodialytic battery systems based on the electric organ of *Electrophorus electricus*

The knifefish *Electrophorus electricus*, commonly known as the electric eel, is able to generate large amounts of electric power to defend itself and shock its prey. The eel is able to do this using its specialized electric organs (**Figure 25a,b**), which feature long stacks of thousands of specialized excitable cells known as *electrocytes*. Each of these excitable cells is able to harness the electrolyte gradient between the potassium-rich cell interior and the sodium-rich extracellular lumen of the organ by using asymmetrically distributed ion channels in order to generate a transient transcellular voltage of around 150 mV at open circuit (**Figure 25b,c**). These small voltages add together in the thousands along the length of the eel's electric organ to produce open-circuit voltages up to 600 V; at short circuit, the eel can draw up to 1 ampere of current.<sup>1</sup> We aimed to develop a scheme that similarly harnessed ion gradients across selective membranes to generate electric power. After examining the eel's physiology, we identified several mechanisms that enable it to generate electrical power in an efficient manner, including simultaneous activation, active recharging, and an optimized geometry. We attempted to implement similar features in our own design of an artificial electric organ.

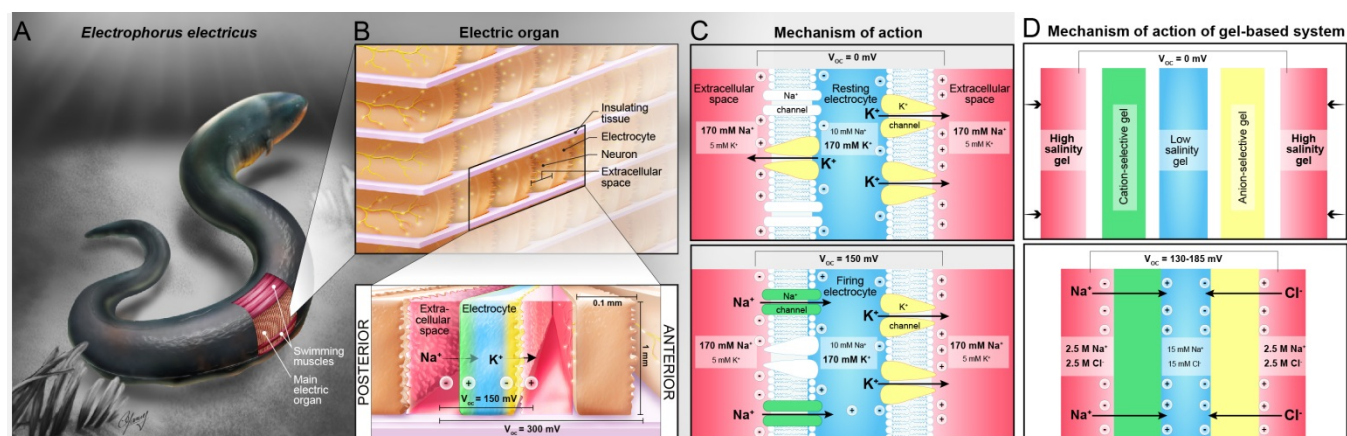


**Figure 25.** Comparison of the mechanism of the electric eel *Electrophorus electricus* and the tetrameric gel cells presented in this work. **a,b**) Electric organs occupying 80% of the length of the eel stack specialized cells known as electrocytes in series and parallel. **c**) The posterior side of each electrocyte depolarizes during a discharge, causing a brief moment in which the potentials across the anterior and posterior membranes are asymmetrical and additive. The resting and action potentials of each membrane are defined by ionic gradients and the selective permeability of the membrane. **d**) Gradients of alternating polarity across alternating cation- and anion-selective membranes also produce additive potentials. When each component of the system is a hydrogel, these potentials can be initiated by mechanical contact.

While our early attempts towards mimicking the eel's physiology focused on using lipid membranes in the form of droplet-interface bilayers to separate ionic reservoirs, we found that these systems were not robust enough to stack thousands of reservoirs and membranes without failure, which would be needed to generate potentials comparable to those of the eel. We therefore moved toward a fully synthetic system made completely of hydrogels, which are

deformable, robust, and able to be manipulated as liquid precursors or “solid” gels. When a high-salinity hydrogel is connected to a low-salinity hydrogel across a charge-selective hydrogel membrane, a small potential forms across the membrane. By stacking an alternating series of high-salinity and low-salinity gels across alternating cation-selective and anion-selective gels in a process akin to reverse electrodialysis,<sup>2,3</sup> we were able to generate an additive potential which increases as more tetrameric gel cells are added in series (**Figure 25d**).<sup>4</sup>

### 5.1. Fluidic implementation produces small voltages

One of our first implementations of the artificial electric organ utilized fluidics to create a series of liquid hydrogel precursor plugs within a tube separated by mineral oil. Once we had filled the tube with the desired number of plugs, we cured it under a UV lamp, which solidified the gel. We then used a fluidic pump to push the gels into mechanical contact, allowing the interstitial oil to escape through a small slit in the tubing. From this implementation, we were able to create series of up to 41 gels, producing a voltage of 1.34 V (**Figure 26a**). We also showed that adding gels in series and in parallel additively increases the voltage and current characteristics, respectively (**Figure 26b,c**). Unfortunately, we found that the fluidic resistance offered by the movement of the gels and the oil through the tubing limited our ability to stack enough gels to reach higher voltages.

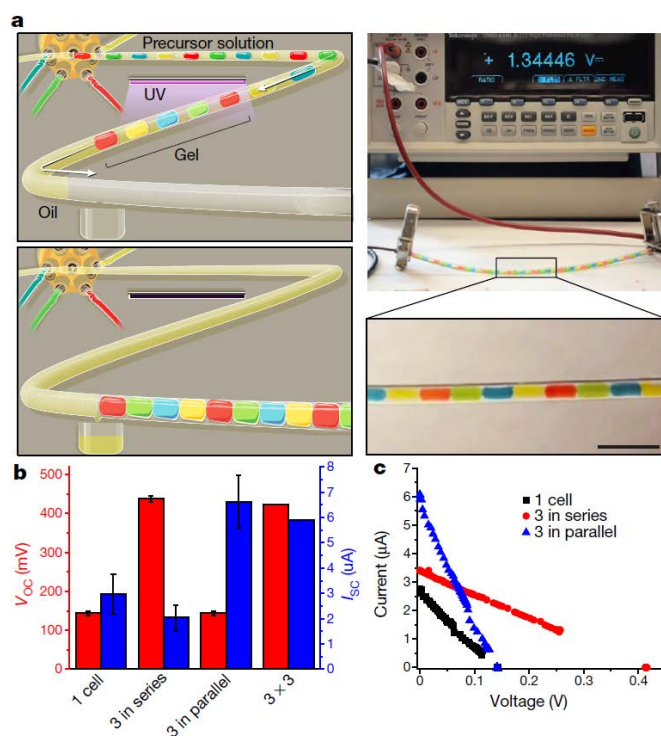
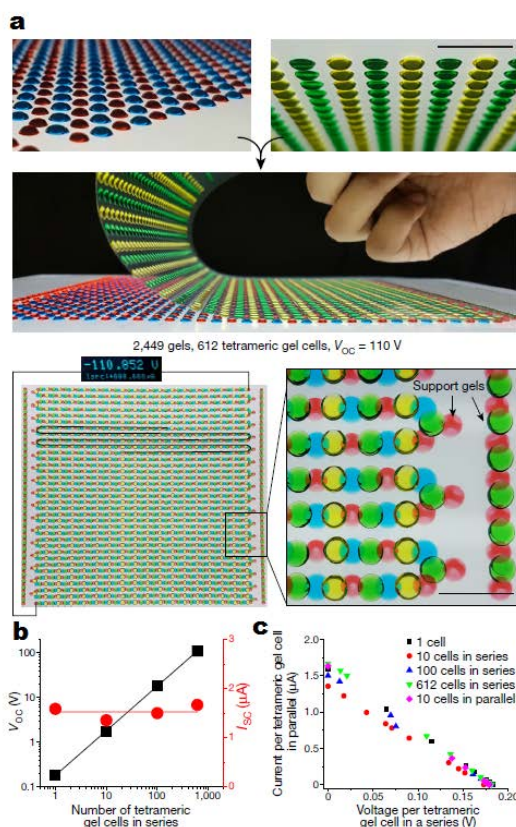


**Figure 26.** Fluidic artificial electric organ. **a)** The left panel shows a schematic of a fluidic artificial electric organ before (top) and after (bottom) contact activation. Aqueous plugs of hydrogel precursor solution were generated in mineral oil, cured with an ultraviolet (UV) lamp, and sequentially brought into mechanical contact after passing a small aperture in the tubing that allowed the interstitial oil to escape. The right panel shows a photograph of a fluidic artificial electric organ with ten tetrameric gel cells (inset; scale bar, 1 cm) generating 1.34 V. **b)** Open-circuit voltage and short-circuit current ( $I_{sc}$ ) characteristics of a fluidic artificial electric organ. Open-circuit voltages (red bars) scale linearly when tetrameric gel cells are added in series; short-circuit currents (blue bars) scale linearly when tetrameric gel cells are added in parallel.

(Error bars show s.d.,  $n = 3$ , except for  $3 \times 3$  in which  $n = 1$ ). **c)** Plot of current and voltage in response to various external loads for one tetrameric gel cell (black squares), three cells in series (red circles), and three cells in parallel (blue triangles).

## 5.2. Printed implementation generates up to 110 volts

To create a larger sequence of gels, we used a printer with microvalves that, when opened, would release a small jet of gel precursor liquid at a target position. We first printed high- and low-salinity gels onto a plastic substrate, then printed cation- and anion-selective gels onto a second substrate in a complementary pattern. Bringing these patterns together created a long, serpentine series of gels. This printer, designed to print biological material in 3D, had very high spatial resolution and produced droplets of consistent size, enabling us to create arrays of thousands of small gels without error. We ultimately created a pathway of 2,449 gels, which



generated 110 V at open circuit (**Figure 27a**). As with the fluidic implementation, we found that voltages and currents added as expected when adding gels in series and in parallel, respectively.

**Figure 27.** Printed artificial electric organ. **a)** Photographs of large complementary arrays of printed hydrogel lenses combining to form a continuous series of 2,449 gels with serpentine geometry. Support gels are used for mechanical stability and do not contribute to the system electrically. Scale bars, 1 cm. **b)** Open-circuit voltage and short-circuit current characteristics of printed artificial electric organs as a function of the number of tetrameric gel cells in a series. **c)** Normalized current-voltage relations of various numbers of tetrameric gel cells added in series or in parallel. The voltage axis is normalized by the number of cells in a series; the current axis is normalized by the number of tetrameric gel cells that are arranged in parallel. All points fall on one curve, as expected for a scalable system.

## 5.3. Miura-ori fold provides 40-fold improvement in power characteristics

While the voltages that we produced with this printed system were quite high, the currents were very low. The high internal resistance of this system was due in large part to very small contact area between gels. To decrease this resistance, we needed a way to stack a series of thin gel films with high contact area. To this end we used an origami fold called the *Miura-ori* fold, which was designed to unfurl solar panels in space.<sup>5</sup> As shown in **Figure 28a**, this fold allowed us to stack a series of thin gel films with high contact area using a single synchronized and self-registered motion. This geometry produced a 40-fold reduction in normalized internal resistance



compared to a series of the same gels connected in a geometry that approximates the printed artificial electric organ (**Figure 28b**). This resistance, however, is still at least two orders of magnitude higher than the resistance of an *Electrophorus* electrocyte (**Table 1**). This discrepancy is partially due to the comparatively high thickness of the gel cells we developed, but the high internal resistance of the artificial electric organ is also at least partially attributable to the low-salinity gel, which provides the dominant resistance of the system. Using ion-selective (as opposed to broadly charge-selective) membranes enables the electric eel to maintain a high ionic strength and conductivity throughout its organs while leveraging steep electrolyte gradients. The development of ion-selective gel or gel-compatible membranes may therefore be a next step in the development of this power generation scheme.

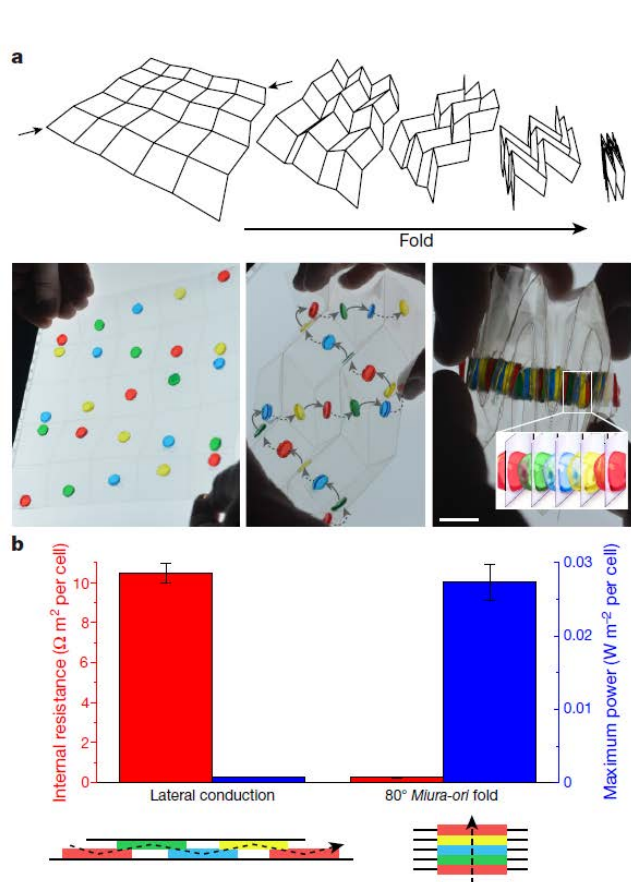


**Figure 28.** *Miura-ori* artificial electric organ. **a)** Schematic and photographs of *Miura-ori* folding. A single motion compresses a two-dimensional array of panels into a self-registered folded state where all panels overlap, generating a one-dimensional sequence. This morphology was used to generate flat and relatively large contact areas between a series of thin gel films, which conducted ions from gel to gel through holes in the supporting polyester substrate. Scale bar, 1 cm. **b)** Area-normalized internal resistance (red) and maximum power (blue) per tetrameric gel cell with 0.7-mm-thick gel films arranged either laterally, in a manner that approximates the relative geometry of the serpentine implementation, or in a *Miura-ori*-assembled stack (error bars show s.e.m.,  $n = 3$ ). The stack geometry imparts a 40-fold reduction in resistance and a corresponding 40-fold improvement in maximum power output.

Source	Thickness of repeating unit* (m)	Cross-sectional area of electric organ (m <sup>2</sup> )	Open-circuit voltage per repeating unit (V)	Internal resistance of repeating unit ( $\Omega$ m <sup>2</sup> )	Maximum power density generated by repeating unit (W m <sup>-2</sup> )
Live eels, anterior 6–10 cm of main organ (ref. 10) <sup>†</sup>	$(1.1 \pm 0.2) \times 10^{-4}$	$(2.3 \pm 0.6) \times 10^{-3}$	$0.11 \pm 0.01$	$(6.8 \pm 0.7) \times 10^{-4}$	$5.5 \pm 1.4$
Live eels, sections of main organ (ref. 11) <sup>‡</sup>	$10^{-4}$	$(3.4 \pm 0.5) \times 10^{-3}$	$0.12 \pm 0.01$	$(5.1 \pm 0.4) \times 10^{-4}$	$10.6 \pm 2.0$
Live eels, leaping (ref. 9) <sup>§</sup>	$10^{-4}$	$2.8 \times 10^{-3}$	0.16	$4.8 \times 10^{-4}$	13.6
Gel cells, this work, 80° fold	$2.8 \times 10^{-3}$	$8.5 \times 10^{-5}$	$0.17 \pm 0.01$	$0.27 \pm 0.02$	$0.027 \pm 0.002$

**Table 1.** Comparison of parameters from natural and artificial electric organ

Where applicable, values are presented as mean  $\pm$  s.e.m.

\*Repeating unit refers to an electrocyte in the eel's electric organ (refs 9,10,11) and to a tetrameric gel cell in this work.

†Parameters are averages of the farthest anterior measurements for each of the four eels from table 2 of ref. 10. Cross-sectional area is estimated from eels of corresponding length in Table 1 of ref. 11.

‡Parameters are averages of all measurements from Table 1 of ref. 11. Repeating unit thickness is an estimate reported in ref. 11. Open-circuit voltage values were calculated by multiplying reported electromotive force values by a factor of 0.77 (an average factor reported in ref. 11). Unit resistance and power density were estimated for each eel based on the approximation made in ref. 11 that the external resistance was approximately equal to the internal resistance of the system.

§Average of two experiments. Open-circuit voltage and short-circuit current extracted from highest position attained by each ascending eel, for which both parameters are shown in figure 4c of ref. 9.

Cross-sectional area estimated from eels of corresponding length in Table 1 of ref. 11, repeating unit thickness estimated from anterior voltage distributions reported in ref. 12. Assumptions: eel tilt angle, 70°; electric organ begins 20% of reported eel length from its front tip <sup>[10]</sup>, resistance in the water tank from Fig. 3 of ref. 9 is negligible.

#### 5.4. External power supply can recharge artificial electric organ

To prove that this system could be recharged, we connected it to an external power supply and drove a current which opposed the direction of the discharge current. In **Figure 29**, we show that for up to at least 10 discharge/recharge cycles, we were able to recover at least 90% of the initial capacity of the system.

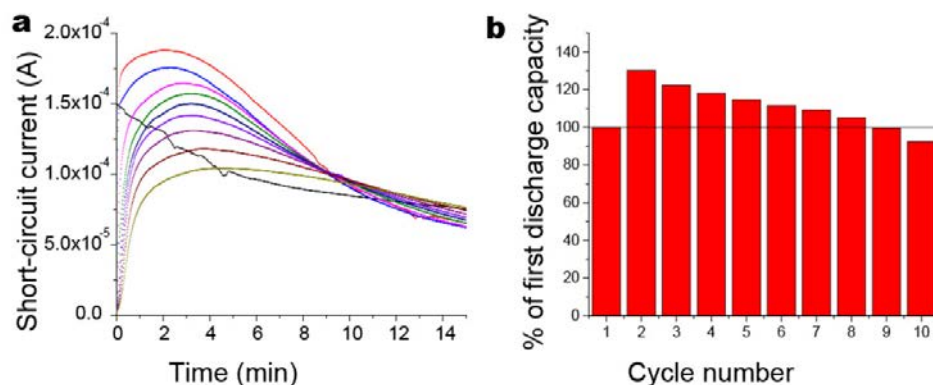


**Figure 29.** The artificial electric organ can be recharged. **a)** Current versus time recordings of ten discharges of a single tetrameric gel cell at short circuit following recharging. Initial discharge shown in black; subsequent discharges in the following order: red, blue, magenta, green, navy, purple, plum, wine, olive. **b)** Bar graph of normalized integrals of discharge curves.

## 5.5. Outlook

Hydrogels are moldable, flexible, and transparent – characteristics not typically associated with traditional energy storage devices. They can also be biocompatible; we envision a future for this project in which biological fluids of differing electrolyte concentrations serve as source streams that power wearable or implantable electronic devices such as diagnostic sensors. Another potential application is as a power source for existing pressure sensors or augmented reality displays in contact lenses,<sup>6,7</sup> which are commonly fabricated out of hydrogels.<sup>8</sup> As a first step towards this goal, we have created a trilayer hydrogel structure in the shape of a contact lens which is able to generate 80 mV (**Figure 30**).

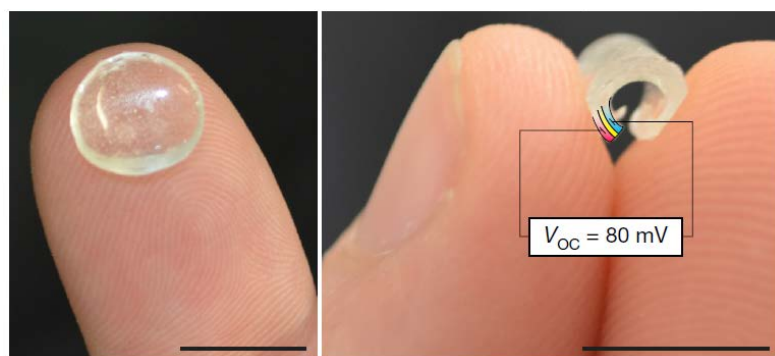


**Figure 30.** Flexible and transparent artificial electric organ prototype with the shape of a contact lens (left). The prototype is composed of a gel trilayer of high-salinity gel (indicated by a false-colored section in red), anion-selective gel (yellow), and low salinity gel (blue) with a total thickness of 1.2 mm that produced an open circuit voltage of 80 mV

A manuscript regarding this work has been published in *Nature*, **2017**, 552(7684), 214.

## References

- (1) Gotter, A. L.; Kaetzel, M. A.; Dedman, J. R. *Comp. Biochem. Physiol. A. Mol. Integr. Physiol.* **1998**, 119 (1), 225.
- (2) Weinstein, J. N.; Leitz, F. B. *Science* **1976**, 191 (4227), 557.
- (3) Jia, Z.; Wang, B.; Song, S.; Fan, Y. *Renew. Sustain. Energy Rev.* **2014**, 31, 91.
- (4) Schroeder, T. B. H.; Guha, A.; Lamoureux, A.; VanRenterghem, G.; Sept, D.; Shtein, M.; Yang, J.; Mayer, M. *Nature* **2017**, 552 (7684), 214.
- (5) Miura, K. *Inst. Space Astronaut. Sci.* **1985**, No. 618, 1.
- (6) Lingley, A. R.; Ali, M.; Liao, Y.; Mirjalili, R.; Klonner, M.; Sopanen, M.; Suihkonen, S.; Shen, T.; Otis, B. P.; Lipsanen, H.; Parviz, B. A. *J. Micromechanics Microengineering* **2011**, 21 (12), 125014.
- (7) Mansouri, K.; Medeiros, F. A.; Tafreshi, A.; Weinreb, R. N. *Arch. Ophthalmol.* **2012**, 130 (12), 1534.
- (8) Kopecek, J. *J. Polym. Sci. Part Polym. Chem.* **2009**, 47 (22), 5929.
- (9) Catania, K. C. *Proc. Natl. Acad. Sci.* **2016**, 113 (25), 6979.
- (10) Nachmansohn, D.; Cox, R. T.; Coates, C. W.; Machado, A. L. *J. Neurophysiol.* **1942**, 5 (6), 499.
- (11) Cox, R. T.; Coates, C. W.; Brown, M. V. *Ann. N. Y. Acad. Sci.* **1946**, 47 (4), 487.
- (12) Cox, R. T.; Rosenblith, W. A.; Cutler, J. A.; Mathews, R. S.; Coates, C. W. *Zoologica* **1940**, 25, 553.



## 6. Molecular Dynamics Simulations of Archaea-Inspired Lipids

Our work over the past five years has been to construct membranes with different lipids and simulate these systems to gain insight into how their molecular structure affects the biophysical properties of the membrane. All of this simulation work has been done together with experiment, and this has led to new and important insights. The following sections summarize some of the key findings resulting from these studies.

### 6.1. Simulation Details

All simulations were performed using charges, bond, and angle parameters derived from the CHARMM36 lipid and CHARMM36 CGenFF forcefield parameters. We first constructed 81-lipid models in order to equilibrate and area per lipid of each system. Following approximately 50 ns of equilibration, the 81-lipid system was replicated in a 3x3 array to produce the full 729-lipid membrane used for all subsequent simulations. The temperature was fixed at 300, 315 or 330 K, and temperature coupling was done using the Nose-Hoover chain method. The pressure was fixed at 1 atm in the direction normal to the membrane surface, and the Langevin piston was used to maintain the pressure. All the simulations were carried out using NAMD in explicit water using TIP3P water models and ions were added to neutralize the system (if needed) and maintain an ionic strength of 50 mM monovalent salt. We used with a 10-Å cut off for van der Waals with an 8.5 Å switching distance, and Particle Mesh Ewald for long-range electrostatics. All subsequent analysis was performed using R and VMD.

### 6.2. Self-Diffusion of Lipids

Since we performed equilibrium simulations, we can extract a number of equilibrium properties of the membrane, one of the most basic being the self-diffusion of lipids. Unlike liquids, the self-diffusion of lipids exhibits two different behaviors at short and long-time scales (Wohlert & Edholm, 2006). At short time scales, the lipids diffuse rapidly within an area equivalent to their area per headgroup and have a characteristic diffusion constant  $D_1$ . At longer times, the lipids begin to intercalate with one another and exhibit slower but long-range diffusion with a characteristic constant  $D_2$ . The mean-square displacement versus time is shown in **Figure 31** below, and the diffusion constants are summarized in the table.

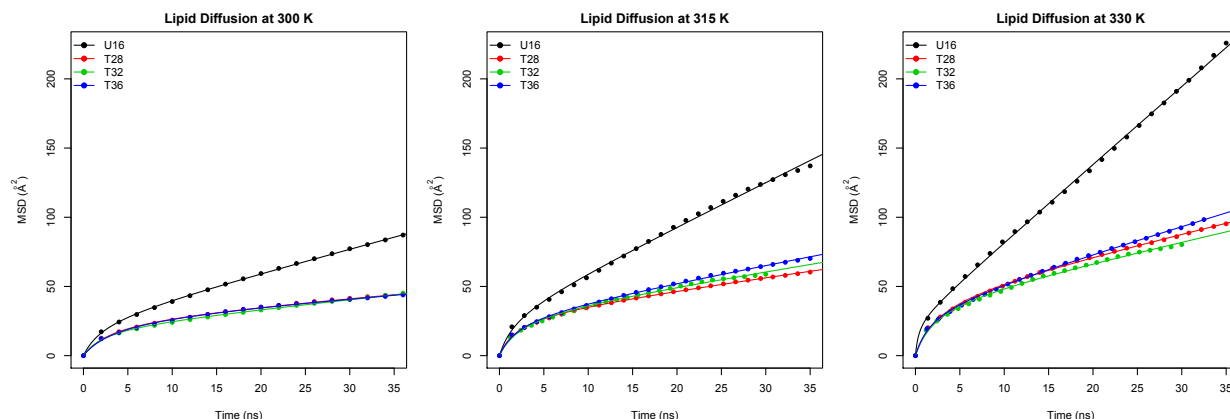


**Figure 31.** Examples of mean-square displacement (MSD) vs. time for U16, T28, T32 and T36 as a function of temperature. The y-axes are the same for each plot to highlight the increase in displacement at higher temperature.

Lipid	T (K)	$D_1 \pm \text{SE (95\% CI)}$ ( $\times 10^{-11} \text{m}^2/\text{s}$ )		$D_2 \pm \text{SE (95\% CI)}$ ( $\times 10^{-11} \text{m}^2/\text{s}$ )	
T28 (LER-A-146)	300	$2.03 \pm 0.10$	(1.83, 2.27)	$0.13 \pm 0.0035$	(0.121, 0.136)
	315	$3.65 \pm 0.15$	(3.35, 4.01)	$0.22 \pm 0.0044$	(0.213, 0.231)
	330	$4.38 \pm 0.24$	(3.91, 4.96)	$0.38 \pm 0.0091$	(0.36, 0.40)
T32 (LER-B-09)	300	$2.22 \pm 0.17$	(1.89, 2.65)	$0.16 \pm 0.0036$	(0.155, 0.171)
	315	$3.12 \pm 0.26$	(2.61, 3.84)	$0.26 \pm 0.013$	(0.225, 0.283)
	330	$4.47 \pm 0.35$	(3.79, 5.40)	$0.36 \pm 0.014$	(0.326, 0.391)
T36 (LER-B-10)	300	$1.88 \pm 0.09$	(1.69, 2.10)	$0.12 \pm 0.004$	(0.113, 0.13)
	315	$3.40 \pm 0.24$	(2.93, 4.00)	$0.3 \pm 0.0073$	(0.288, 0.32)
	330	$4.98 \pm 0.28$	(4.43, 5.65)	$0.49 \pm 0.0071$	(0.47, 0.50)
U16 (LER-B-86)	300	$2.99 \pm 0.14$	(2.71, 3.33)	$0.42 \pm 0.0026$	(0.418, 0.43)
	315	$4.42 \pm 0.84$	(2.95, 7.54)	$0.79 \pm 0.018$	(0.742, 0.828)
	330	$16.79 \pm 7.00$	(9.29, 70.1)	$1.41 \pm 0.012$	(1.38, 1.43)
POPC	300	$4.65 \pm 0.14$	(4.37, 4.96)	$0.65 \pm 0.0015$	(0.645, 0.651)

From looking at the measured diffusion constants, the increase we observe as a function of temperature is greater than the linear increase one would expect from  $D = kT/\zeta$  where  $kT$  is the thermal energy in the system and  $\zeta$  is the drag. This indicates that the drag  $\zeta$  decreases as a function of temperature, resulting in a higher rate of diffusion. Further, the change in the drag as a function in temperature is different for each lipid as a result of the altered structure in the membrane spanning part of the lipid. This is an important observation and is currently being pursued further.

### 6.3. Area per Lipid Headgroup

All of our simulations were performed at constant pressure, we observe fluctuations in the volume of our system ( $p$  and  $V$  are conjugate variables related through the fluctuation-dissipation theorem). The fluctuations in the plane of the membrane give rise to changes in the area per headgroup, a key metric for comparing lipids. **Figure 32** and the table below show the time course of fluctuations in our simulations and the corresponding values with their standard errors.

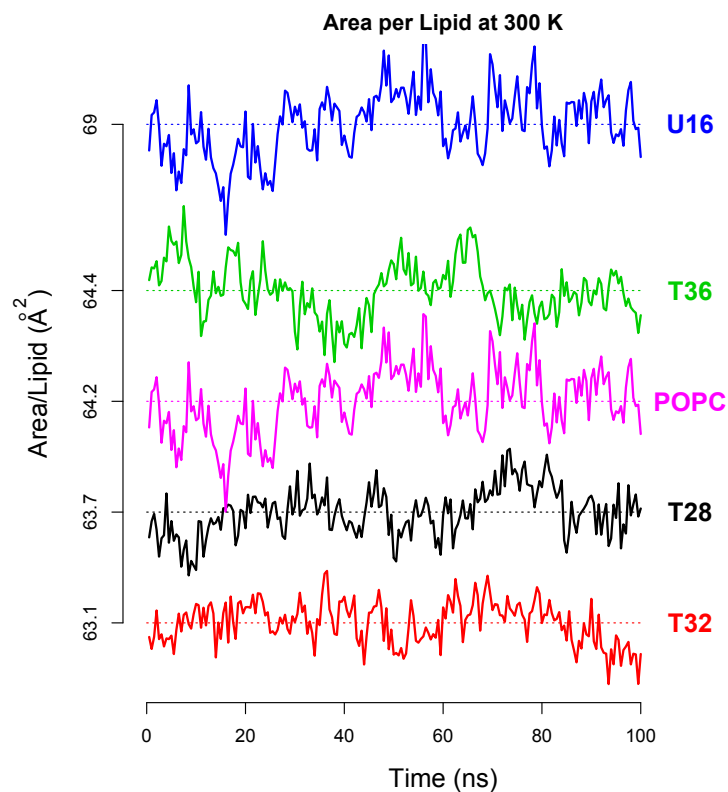


**Figure 32.** Fluctuations in the area per headgroup at 300 K. The absolute scale of the y-axis has been change so that the individual traces to not overlap. The mean values are shown on the left.

Lipid	Temperature (K)	Area/Lipid $\pm SE$ ( $\text{\AA}^2$ )	Var(Area/Lipid) $\pm SE$ ( $\text{\AA}^4$ )
POPC	300	$64.19 \pm 0.033$	$0.213 \pm 0.021$
T28	300	$63.72 \pm 0.015$	$0.047 \pm 0.005$
T32	300	$63.11 \pm 0.014$	$0.036 \pm 0.004$
T36	300	$64.43 \pm 0.018$	$0.063 \pm 0.006$
U16	300	$68.97 \pm 0.021$	$0.090 \pm 0.009$
T28	315	$65.40 \pm 0.019$	$0.070 \pm 0.007$
T32	315	$64.32 \pm 0.028$	$0.154 \pm 0.015$
T36	315	$65.51 \pm 0.019$	$0.075 \pm 0.007$
U16	315	$70.36 \pm 0.028$	$0.159 \pm 0.016$
T28	330	$67.18 \pm 0.023$	$0.101 \pm 0.010$
T32	330	$66.31 \pm 0.023$	$0.101 \pm 0.010$
T36	330	$67.09 \pm 0.021$	$0.087 \pm 0.009$
U16	330	$71.94 \pm 0.028$	$0.158 \pm 0.016$

The area per lipid headgroup is typically thought to be largely a function of the headgroup itself. In our case, all the headgroups are PC (phosphatidylcholine) and the absolute difference we see between lipids are not that significant compared to what is observed with other headgroups. One thing we do see is that the variance in the area per lipid does show more significant differences between lipids, and this is more clearly illustrated in **Figure 33** below.

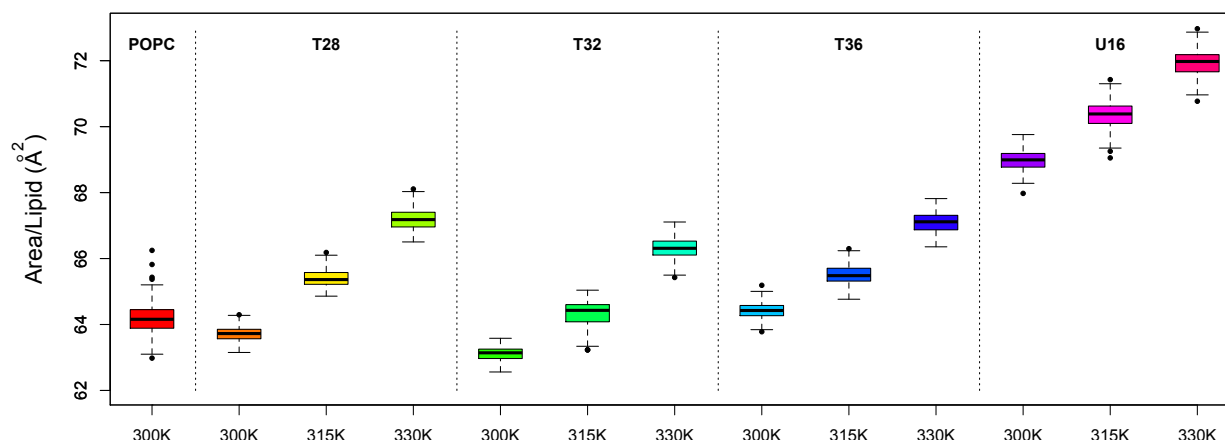


**Figure 33.** Boxplot showing the area per headgroup as a function of temperature. Just as we saw in the table above, the variance for the bilayer lipids (POPC and U16) are greater than for the tethered lipids.

The variance in membrane area is proportional to the lateral compressibility of the membrane ( $\kappa$ ), and that in turn has been hypothesized to be a first-order determinant of the permeability of the membrane (Nagle & Scott, 1978). Although the mean area increases as the temperature is goes up, due to membrane thinning and overall conservation of lipid density, the increase in variance is less pronounced and once again different for each lipid. These values will be compared to the permeability measurements in a later section.

#### 6.4. Membrane Thickness

Just like the area per headgroup, the membrane thickness is a primary metric of the system. The figures and table below show the thickness as a function of time and the mean values from our simulations.

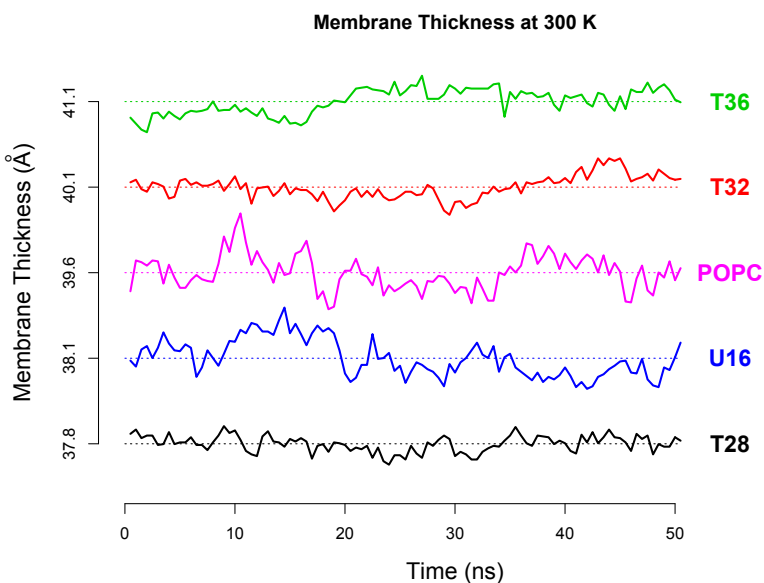


**Figure 34.** Membrane thickness for our lipids over time. Once again, the scale on the y-axis is shifted to separate the individual lipids.

Lipid	T (K)	Membrane Thickness $\pm SE$ (Å)
POPC	300	$39.61 \pm 0.020$
T28	300	$37.83 \pm 0.010$
T32	300	$40.11 \pm 0.013$
T36	300	$41.11 \pm 0.015$
U16	300	$38.11 \pm 0.022$
T28	315	$37.46 \pm 0.014$
T32	315	$39.73 \pm 0.011$
T36	315	$40.97 \pm 0.019$
U16	315	$37.81 \pm 0.024$
T28	330	$36.86 \pm 0.013$
T32	330	$39.09 \pm 0.015$
T36	330	$40.35 \pm 0.014$
U16	330	$37.88 \pm 0.027$

The boxplot below shows the distributions of membrane thickness for each lipid as a function of temperature. As one might expect, based on experimental observations in other systems, the membrane thins as the temperature is increased. Further, the mean thickness of the membrane does increase as the length of the tether is increased, but the increase is not equal to the absolute increase in tether length, indicating that chain disorder and tilt of the lipid tails take up some of this increase.

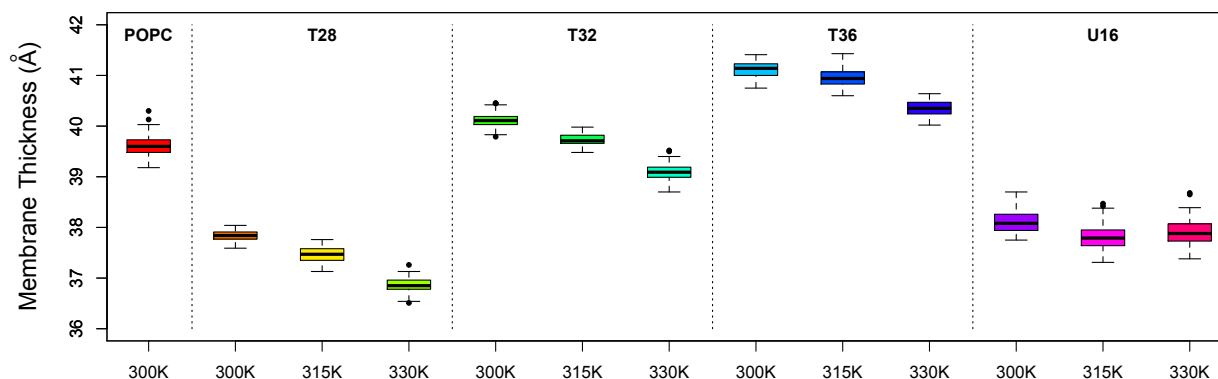


**Figure 35.** Boxplots of membrane thickness vs. temperature for our lipids. Note that as the temperature increase, all the membranes, but the tethered lipid membranes in particular, exhibit slight thinning.

## 6.5. Membrane Mechanics

The macroscopic mechanical properties of the membrane are a key determinant of their overall stability. **Figure 36** below depicts a membrane surface and how fluctuations in bending can be used to determine the mechanics of the material.

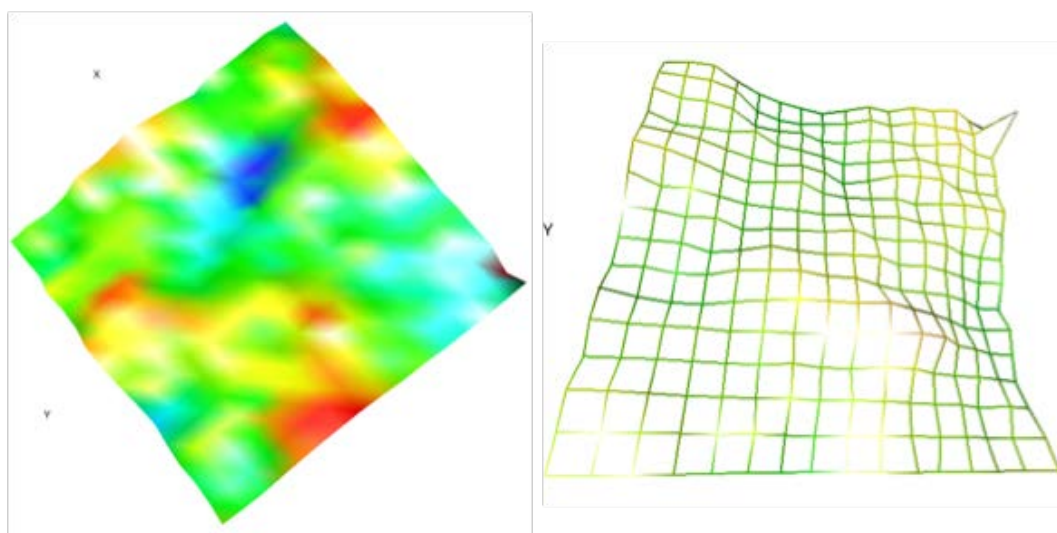


**Figure 36.** (Left) A false color image of a membrane surface showing the level of fluctuations. (Right) A numerically discretized grid used to determine the membrane bending as a function of wave number.

Using the methods from Watson et al. J. Chem Phys 2011, we can derive the bending rigidity of the membrane by analyzing the fluctuations in the surface as a function of the wave number ( $q_n$ ). **Figure 37** shows the results for our membranes at 300 K.

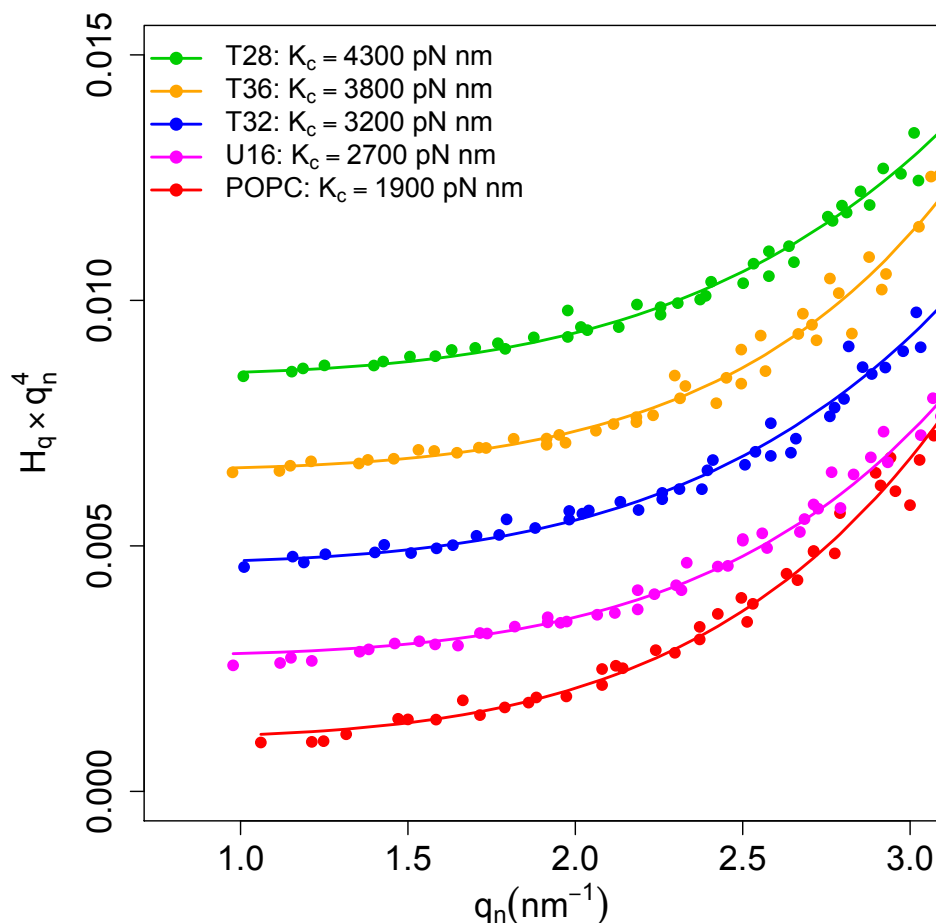


**Figure 37.** Analysis of the fluctuations in the membrane allows us to derive measures of the bending rigidity of the material.

Our tethered lipids all form stiffer membranes than POPC, indicating that they should have more mechanical stability. Too much rigidity can cause these materials to become brittle of course, so we will need to gauge this stiffness carefully through further simulation and experimental testing.

## 6.6. Lipid Order Parameters

The plots on the following page show the order parameters for the lipid tails. A high  $S_{CD}$  value indicates an ordered tail while a lower value shows more randomness. Interestingly, the unlinked acyl chains show nearly identical behavior that is independent of temperature and independent of the length of the tethered linker. As the length of the tether is increased, we see

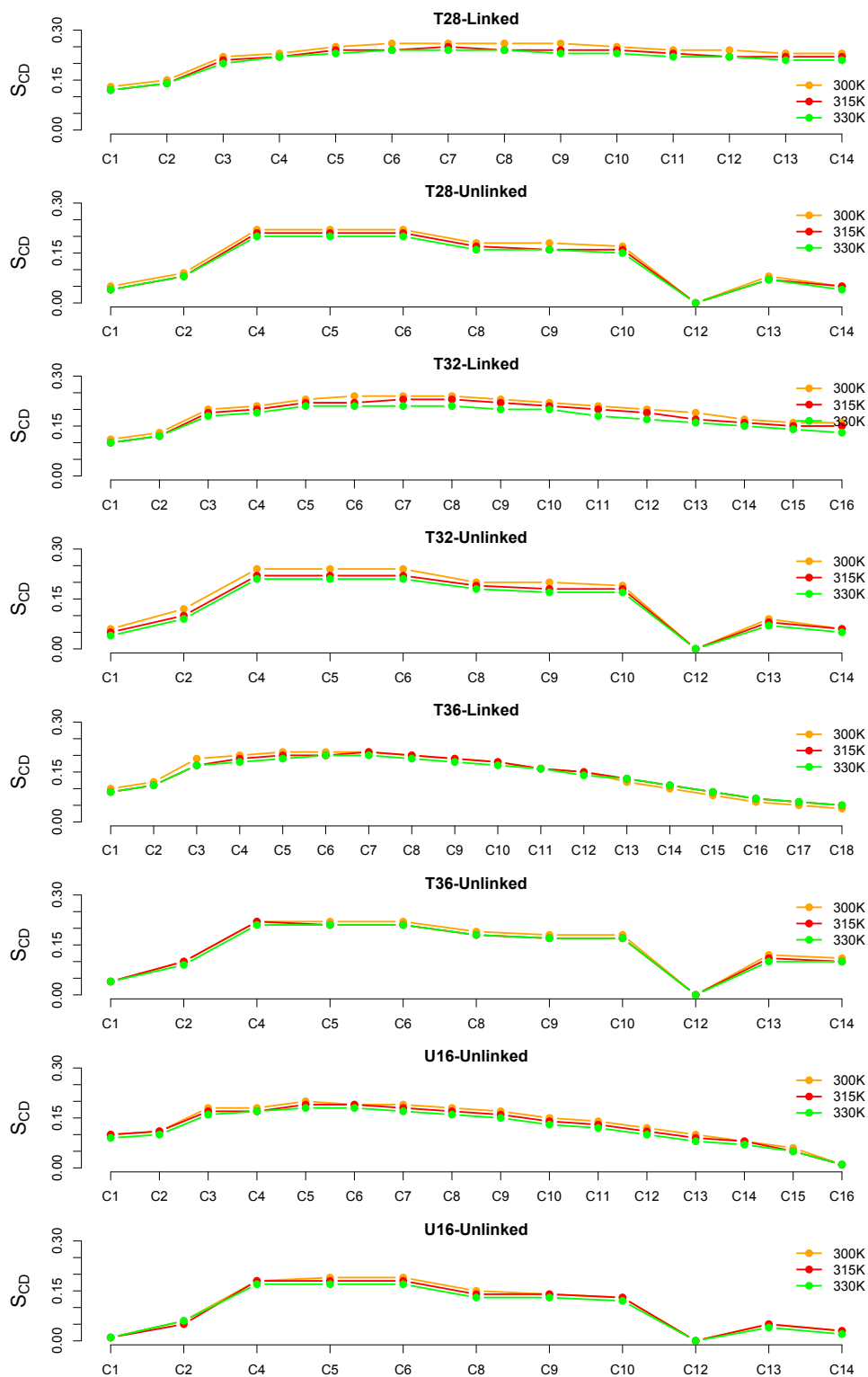


**Figure 38.** Order parameter values for our four lipids as determined through MD simulations.



an increase in the amount of disorder at the center of the membrane. For the longest tethered lipid (T36), the disorder approaches that of the untethered lipid (U16).

### 6.7. Simulations of unlinked, tethered and cyclic lipids

All of our computational and experimental work to this point has looked at the effects of introducing a single tethered alkyl chain that connects two headgroups. Many archaea feature cyclic lipids where both alkyl chain are covalently linked. Because of the significant challenges in synthesizing such molecules we have not explored such structures experimentally, however we felt it was worthwhile to examine their biophysical properties in simulations to see if they exhibited any promise.

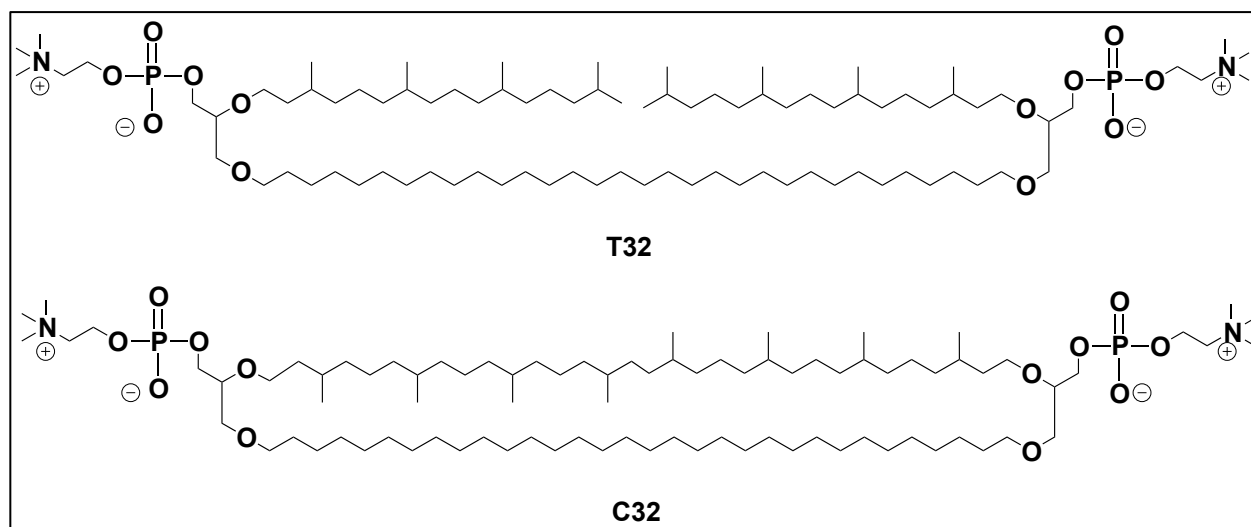


**Figure 39.** Structures for the singly tethered lipid (T32) and the fully cyclic equivalent (C32).

Just as our past work compared equivalent untethered (U16) and tethered (T32) lipids, we produced an equivalent lipid to T32 where the alkyl chains with the isoprenoid groups were also covalently linked (C32 – see **Figure 39**). We followed the identical protocol to previous simulations and generated a 729-lipid membrane and after equilibration, simulated the system for 100 ns.

The first and simplest quantities to characterize are the membrane thickness, the area per headgroup and the variance in the area per headgroup. We found previously that introducing a single tether increased the membrane thickness slightly (38.1 Å for U16 and 40.1 Å for T32) but led to a decrease in the area per lipid (69.0 Å<sup>2</sup> for U16 and 63.1 Å<sup>2</sup> for T32). Since the molecular mass is identical (2 x U16 = T32) and the density must be roughly constant since we are at constant pressure, we would expect the volume of the system to be conserved, and this is consistent with our results. Fluctuations around these mean values are more sensitive to the molecular structure, and we found that a single tether decreased the variance in the area per headgroup by a factor of 3 (0.090 for U16 and 0.036 for T32). In the case of C32, where both alkyl chains are covalently linked, the thickness is essentially identical to the T32 values, both in terms of the mean and the level of fluctuations (**Figure 40**).

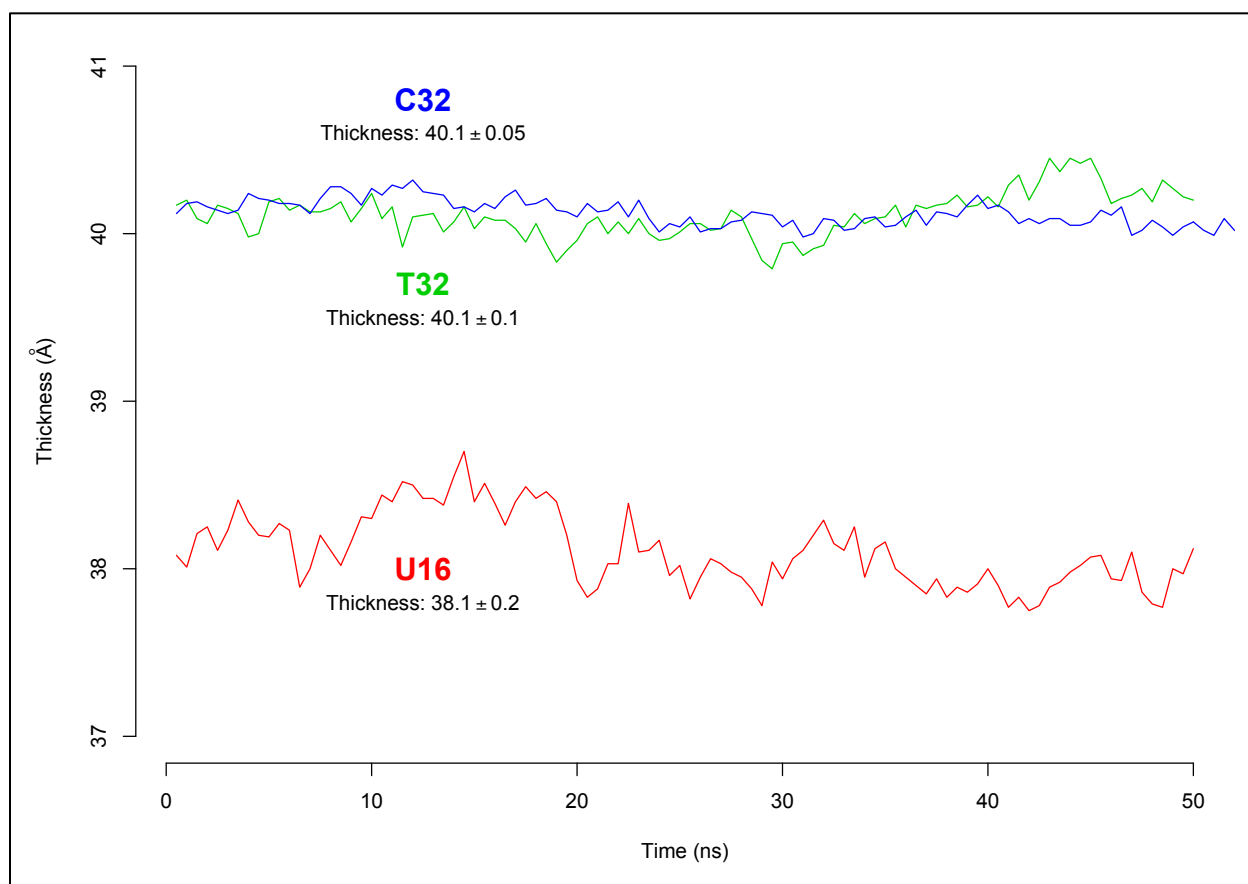


**Figure 40** Membrane thickness as a function of time for U16, T32 and C32 lipids.

If we look at the area per head group and its variance, we see that the fully-cyclic lipid has a slightly smaller mean area ( $62.1 \text{ Å}^2$ ) and the variance is again smaller by about 50% as compared to the single tethered lipid T32 (see **Figure 41**). The smaller area per lipid is perfectly logical since the removal of a free alkyl chain would decrease the degrees of freedom analogous, but opposite, to the case of entropic brushes (Israelachvili 1995). The second tether will further restrict the degrees of freedom and this can be characterized by the Schlitter entropy. In the case of U16, the untethered lipid, the entropy (for a lipid pair) is  $5565 \pm 17 \text{ J mol}^{-1} \text{ K}^{-1}$  and this decreases to  $5276 \pm 20 \text{ J mol}^{-1} \text{ K}^{-1}$  for T32, and further decreases to  $5038 \pm 22 \text{ J mol}^{-1} \text{ K}^{-1}$  for the cyclic lipid C32. This decrease in the entropy leads to a concomitant increase in the order parameters for both alkyl chains, indicating a lower level of fluctuations in the tails. This allows the lipids to pack more closely and will decrease the fluctuations in the overall area.

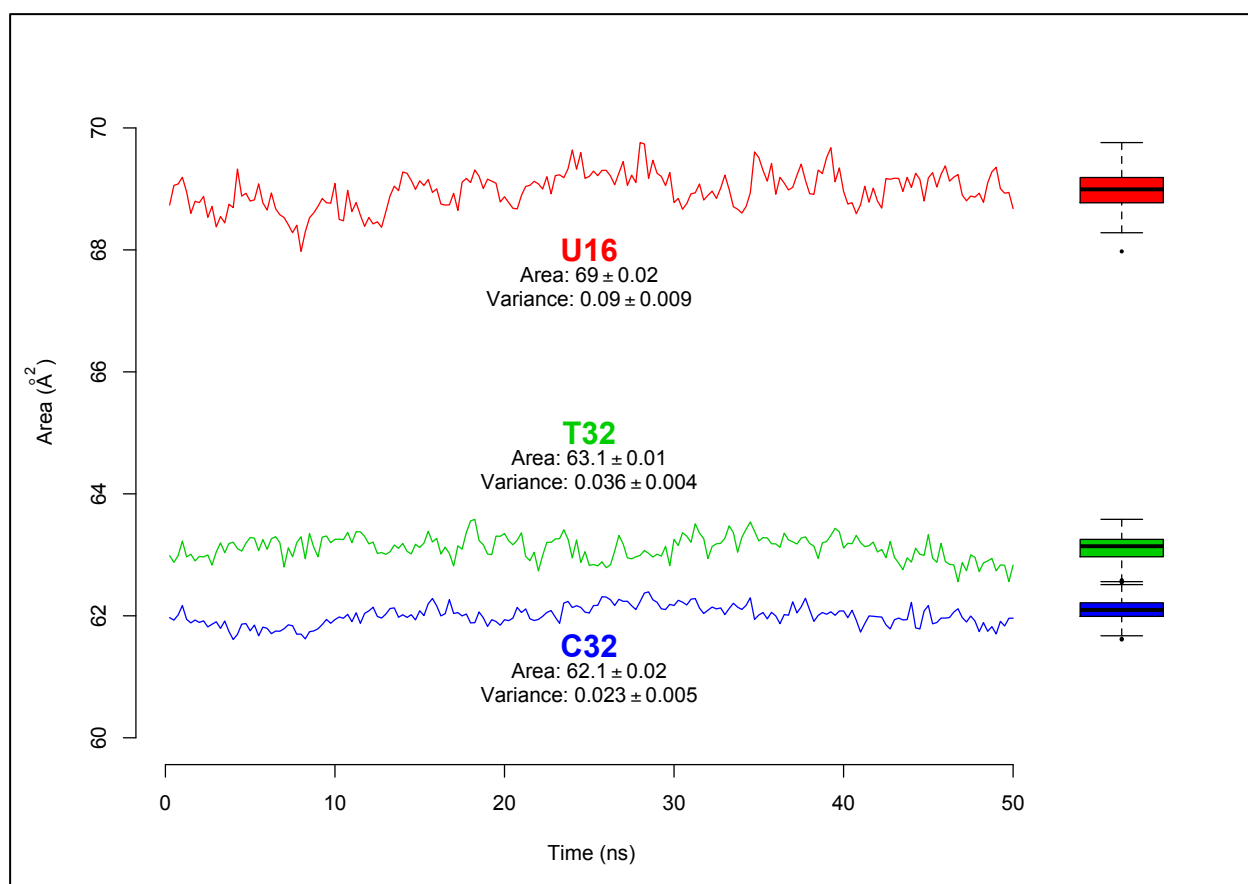


**Figure 41.** The area per lipid headgroup as a function of time for U16, T32 and C32. Introducing successive tethers across the membrane decreases the area and its variance.

The self-diffusion of lipids in the membrane is another key biophysical property of a membrane. As a reminder, lipids exhibit two distinct phases of diffusion – a fast, local diffusion where the head group moves within the area defined by the surrounding lipids, and slower, long-time scale diffusion where the lipids move between each other. Wohler and Edholm showed that these two effects could be expressed in a single equation for the mean-square displacement as a function of time (Wohler and Edholm 2006)

$$\langle x(t)^2 \rangle = \frac{4D_1 t r_o^2}{r_o^2 + 4D_1 t} + 4D_2 t$$

In the above equation, the  $D_1$  diffusion constant describes the short timescale, local movement while  $D_2$  is the more conventional, long timescale diffusion constant. As shown in the table below and the plot in **Figure 42**, C32 exhibits faster local diffusion than either U16 or T32, but its long-range diffusion is an intermediate value. Again, since both lipid tails are covalently linked, the drag within the membrane should be less than it would be for T32 or U16 since there will be less entanglement. However, C32 still requires the movement of two headgroups on each surface of the membrane and this makes it only marginally more mobile than T32. Taken

Lipid	Temperature (K)	$D_1 \pm \text{SE (95\% CI)}$ ( $\times 10^{-11} \text{m}^2/\text{s}$ )	$D_2 \pm \text{SE (95\% CI)}$ ( $\times 10^{-11} \text{m}^2/\text{s}$ )
U16	300	$2.99 \pm 0.14$ (2.71, 3.33)	$0.42 \pm 0.0026$ (0.418, 0.430)
T32	300	$2.22 \pm 0.17$ (1.89, 2.65)	$0.16 \pm 0.0036$ (0.155, 0.171)
C32	300	$4.87 \pm 1.10$ (3.22, 8.54)	$0.35 \pm 0.0028$ (0.344, 0.355)

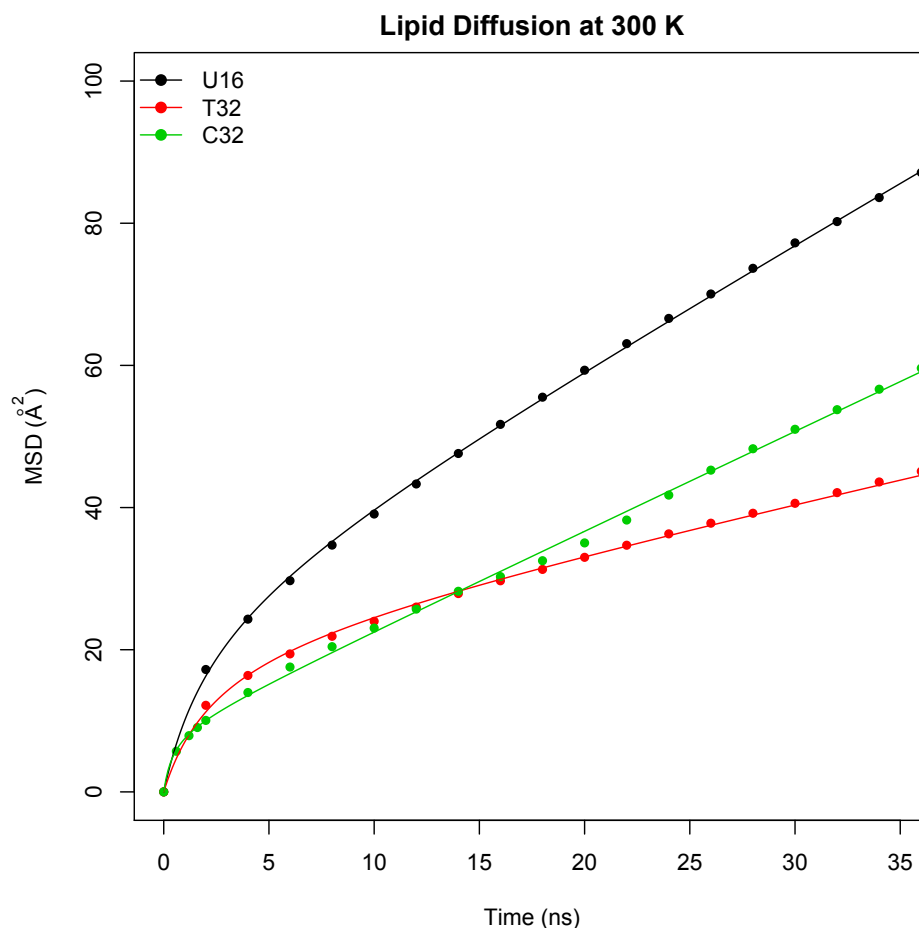


**Figure 43.** Mean-square displacement (MSD) as a function of time for the U16, T32 and C32 lipids. The values derived from the simulation are shown as circles and the lines represent the theoretical fit.

together, this suggests that a singly tethered lipid, such as T32, may be more optimal for applications where a lower rate of diffusion is beneficial.

One of our most intriguing findings of the past year was that the permeability of a membrane shows nearly perfect correlation with the number of waters observed in the hydrophobic core of the membrane. During the time course of our simulations, very few (if any) of these waters actually pass through the membrane, but the rate at which they can penetrate past the lipid headgroups appears to be the rate-limiting step in the overall permeation process. If we look at the number of observations of water that get between the ether oxygens of the headgroups on either side of the membrane, we see that U16 had 20 observations with 3 or more waters in the membrane, T32 had 25 observations over the same period of time, but C32 allowed 45 events with 3 or more waters (see **Figure 44**). This increased level of water penetration should

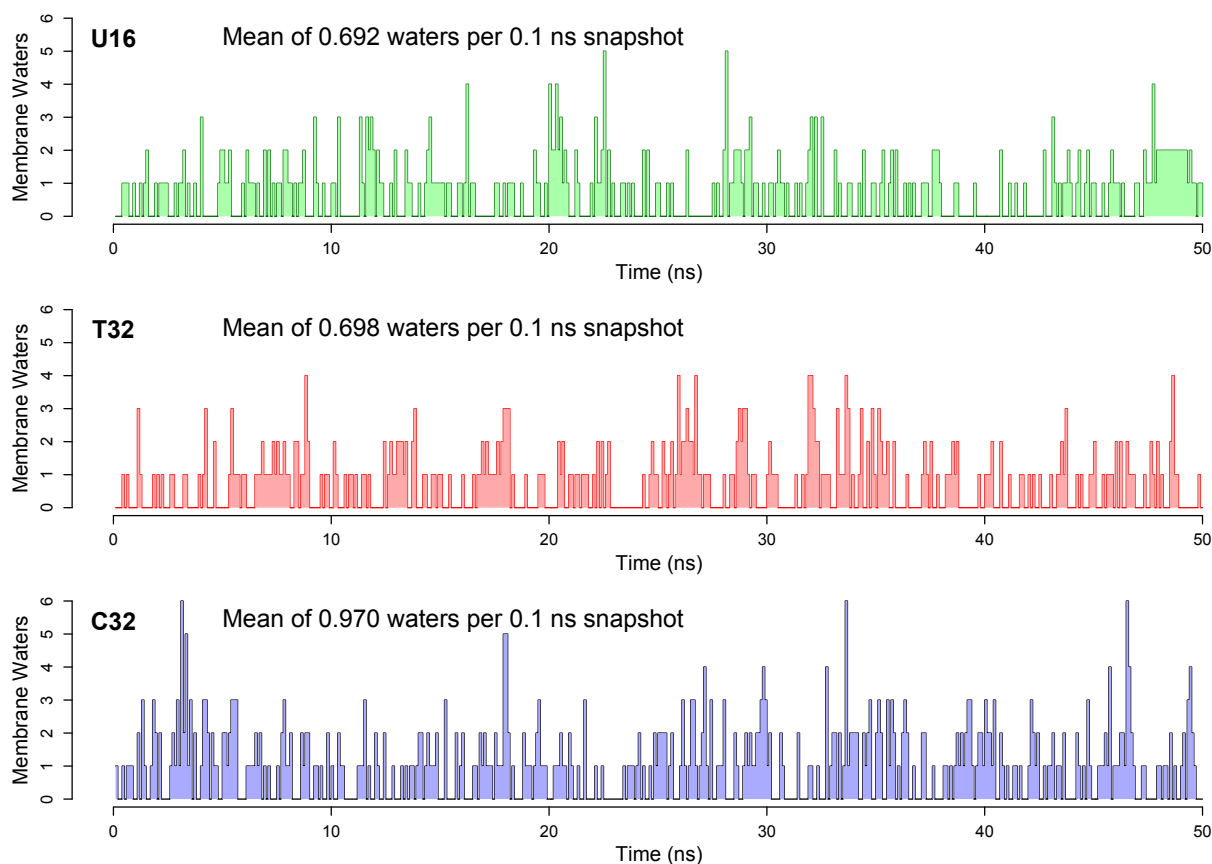


**Figure 44.** Occurrence of water in the membrane hydrophobic core for U16, T32 and C32 lipids.

correspond to a higher level of permeation, based on our earlier observations, and thus we might expect C32 to leak more than similar membranes of T32 or U16.

One final consideration is the mechanics of the C32 membrane. Treating a membrane using continuum mechanics requires us to average out all the molecular details, considering the surfaces of the membrane, etc. There are multiple theoretical treatments that attempt to make this connection with atomistic simulations, but Frank Brown's group (UCSB) has consistently produced the most self-consistent level of theory.

In the case where the surface tension is small, they derive a formula for the fluctuations in membrane height ( $H_q$ ) as a function of the water vector  $q$  (Watson, Penev et al. 2011):

$$\langle |H_q|^2 \rangle = \frac{k_B T}{2} \left( \frac{1}{K_c q^4} + \frac{1}{K_\theta q^2} + \frac{1}{K_\lambda} \right)$$

where  $k_B T$  is the thermal energy,  $K_c$  is the bending modulus,  $K_\theta$  is the tilt modulus, and  $K_\lambda$  is the protrusion modulus. As shown in the plot and table in **Figure 45**, the membrane bending modulus for each lipid is essentially unchanged, however the tilt modulus decreases as we introduce tethers, indicating that it is easier to reorient a lipid relative to the membrane normal. In a similar fashion, it becomes more difficult for one surface of the membrane to protrude as tethers are formed. Since the headgroups define the membrane surface, it is logical that covalent links between headgroups on either side of the membrane will limit how much one side can protrude with respect to the other.

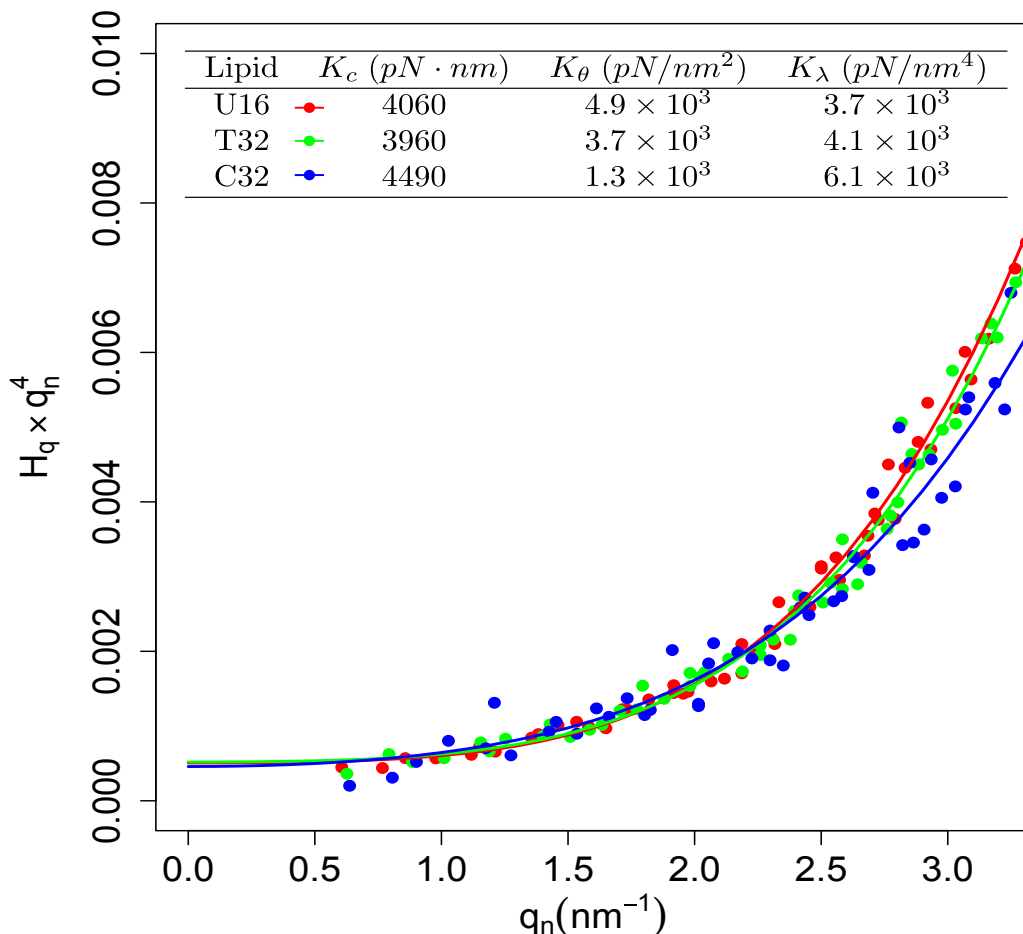


**Figure 45.** Membrane height fluctuations as a function of wave number for U16, T32 and C32 lipids. The lines are fit to the theoretical results from Watson et al. 2011.

In summary, the C32 lipid exhibits some intriguing biophysical properties that may make it useful for particular applications, however we would conclude that its properties are not novel enough to warrant any attempt to synthesize these molecules at this point. Further theoretical work is ongoing in collaboration with Frank Brown (UCSB) and Fred MacKintosh (Vrije Universitat Amsterdam) to understand the membrane mechanics of U16, T32 and C32 lipids.

## 6.8. Tethered lipids and lipid folding

In studying tethered lipids we have consistently worked under the hypothesis that these lipids span the entire membrane with headgroups on opposite sides. This idealized picture may indeed be true, or mostly true, but even with a covalent link there is the possibility that individual lipids could adopt a “U” conformation where both headgroups would end up one side of the membrane.

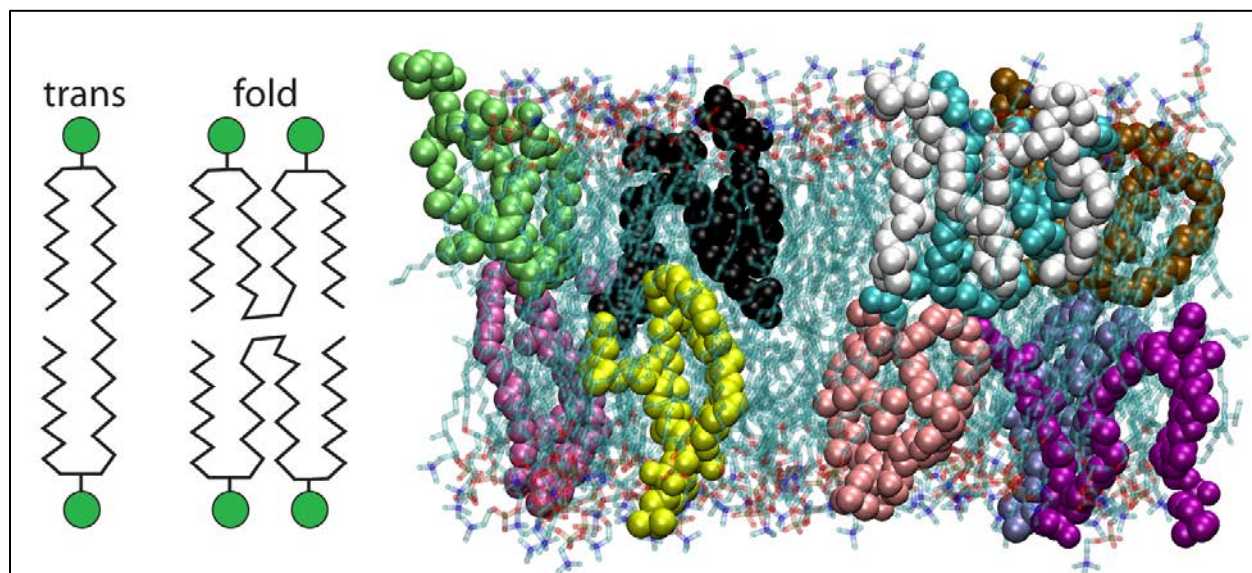


**Figure 46.** A membrane constructed of T32 lipids where 1 out of every 8 are folded such that the headgroups reside on the same side of the membrane. The schematic on the left shows the two possible configurations. Folded lipids are rendered as van der Waals spheres on the right and each lipid is colored individually.

To test the potential effects of these folded lipids, we constructed a membrane where 12.5% of the T32 lipids were folded and the remainder were in the trans configuration (see **Figure 46**). Folded lipids were always produced in pairs such that the number of headgroups was the same on the two sides of the membrane, and the full membrane (again 729 lipids) was equilibrated and simulated using the identical parameters and protocols from before.

The membrane with folded lipids (hereafter referred to as T32F) exhibited perfect stability and the folded species behaved exactly as the trans lipids. The basic membrane parameters such as thickness, area and area fluctuations were largely unchanged from the pure T32 trans membrane. This may be due to the fact that we only considered 12.5% folded lipids, but since the physical chemistry is still the same, it seems unlikely that this would be the case.

When we look at the self-diffusion properties of each membrane species, the results are more intriguing. As shown in **Figure 47**, we now observe three distinct regimes in the mean-square displacement plot. Just as before, we see a short time scale where the lipids explore their local area, a longer time scale where they move between other lipids, but now we observe a third time scale where the lipids begin to encounter the other species (i.e. folded lipids meet trans lipids and vice versa). The theory we applied earlier fits the first two time scales well since it

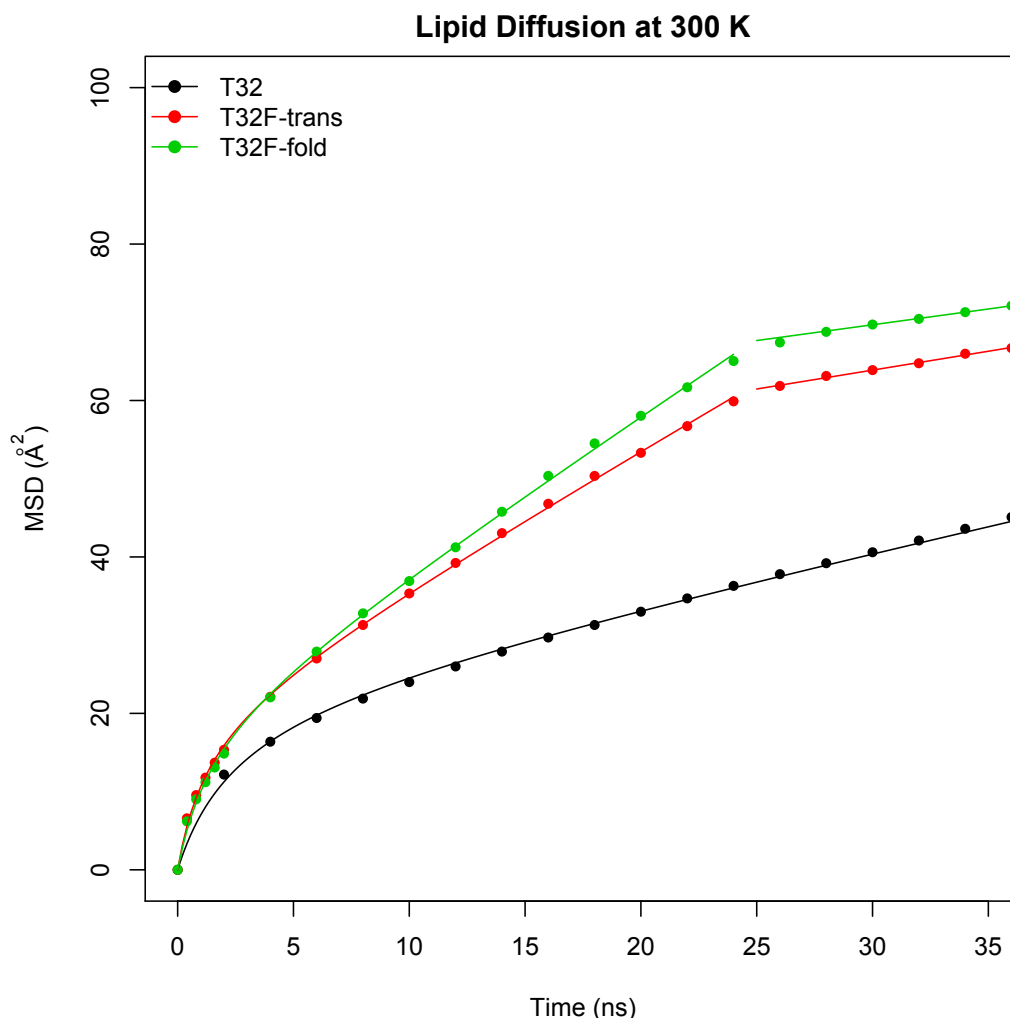


**Figure 47.** Mean-square displacement of lipids for both trans and folded lipids in the case of the T32F membrane. The MSD for T32 is included for comparison.

describes a single lipid type, but there is no theoretical expression for the third regime since it involves multiple lipid species. The long-time scale behaviors are nearly identical with diffusion constants of  $0.065 \times 10^{-11} \text{ m}^2/\text{s}$  for the trans lipids and  $0.055 \times 10^{-11} \text{ m}^2/\text{s}$  for the folded lipids. One might expect the mobility of the folded lipids to be higher given their conformation, however their movement still requires the movement of two headgroups and the drag of the lipid tails is nearly identical, despite the folded structure.

The fact that we see such clear separation of these three different diffusive behaviors stems in large part from the fact that these lipids show phase separation from each other. If the lipids remained well mixed, the MSD behavior of an individual species would show only the short- and long-timescale behaviors of a single lipid. As can be seen in **Figure 48**, the folded lipids in the T32F simulation quickly pair up across the membrane (in 1-5 ns) and move in unison (trans lipids are shown in blue with the folded lipids in red). Over longer time scales, these lipids pairs form lateral connections with other folded lipid pairs, first forming long chains and then forming phase separated domains. We see modest domain formation in our large membrane simulation



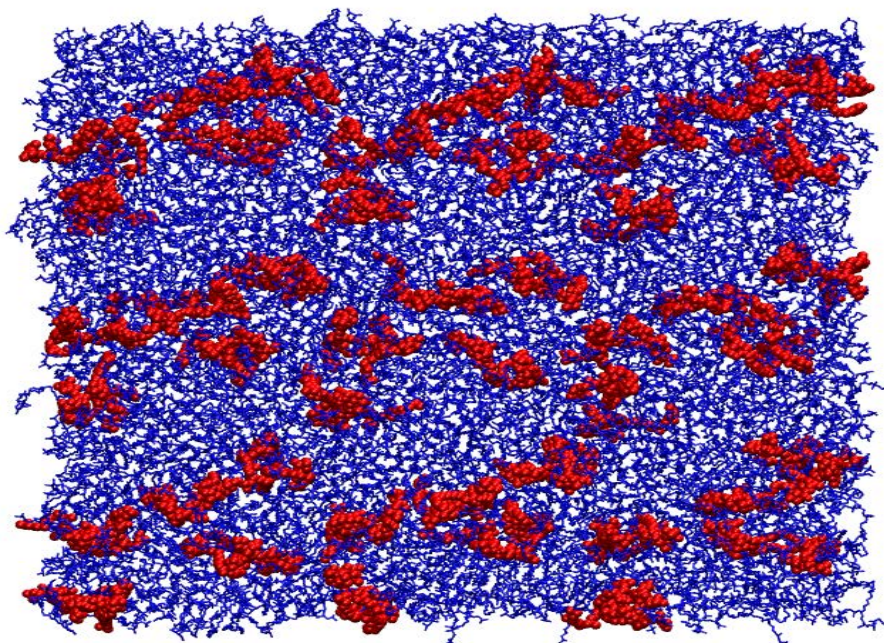


**Figure 48.** The T32F membrane with trans (blue) and folded (red) lipids. The folded lipids cluster to form lipid domains.

(729 lipids) since this simulation is only up to 100 ns. However, for a smaller system of 81 lipids, we can run much longer simulations (currently up to about 1 microsecond) and this system shows good domain formation, even though there are only 10 folded lipids, 5 on each membrane interface.

In terms of water penetration, the T32F membrane shows nearly identical results to the fully-trans, T32 membrane (**Figure 49**). Water entry rates are well described by a Poisson distribution in each case with nearly the same rate. The number of observations with 3+ waters is identical for these two cases, with 25 events over 50 ns for each membrane. Finally, we looked at the membrane mechanics for the T32F membrane. Just as with the water penetration results, we observed no significant difference between T32 and T32F.

Taken together, these results suggest that the presence of folded lipids in the T32 membrane would have observable effects in terms of lipids diffusion and domain formation, but the leakage kinetics and membrane mechanics would largely be indistinguishable from the idealized case where all lipids span the membrane.

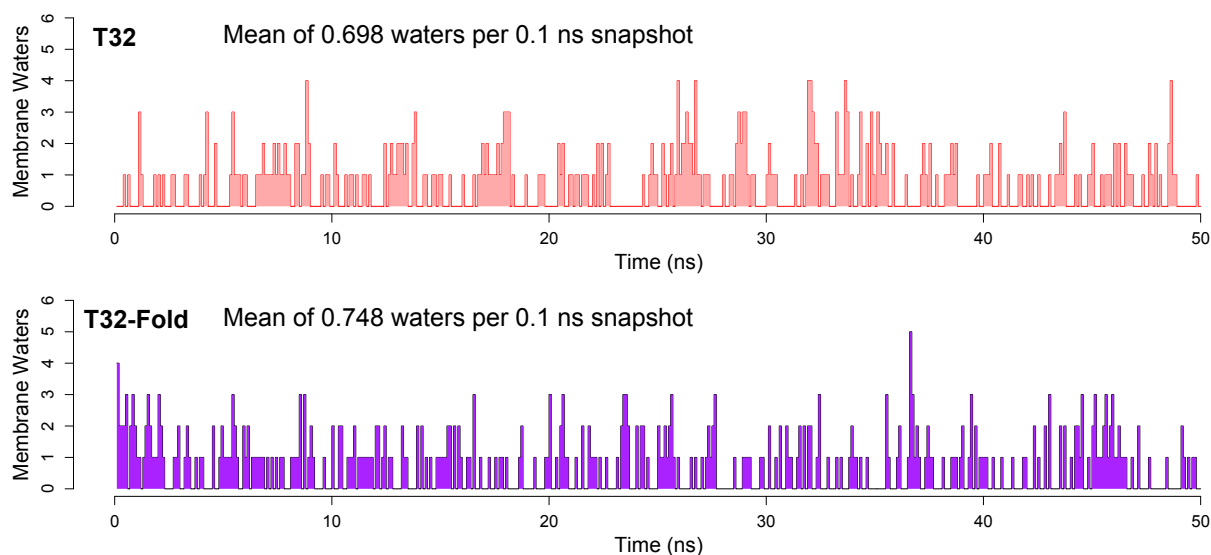


**Figure 49.** Water penetration into the T32 and T32F membranes. The overall Poisson rates are nearly the same and each simulation showed 25 events with 3+ waters in the hydrophobic core.

## 6.9. Effects of rings on membrane biophysics

Apart from the covalent linkages that span the membrane, archaeal lipids also commonly feature rings in the lipid tails. As shown in **Figure 50** below, we constructed two lipids with single rings, one with a cyclopentane ring (CP1) and one with a single cyclohexane ring (CH1).

The addition of a ring within the hydrophobic core should increase the packing of the lipids, but one might imagine the difference would be relatively subtle. If we again use the T32 membrane as a comparison, we see that the area per lipid is shifted modestly. T32 had an area per lipid of  $63.1 \text{ \AA}^2$  and CP1 and CH1 has areas of  $65.1 \text{ \AA}^2$  and  $63.0 \text{ \AA}^2$  respectively. Although the areas are fairly close in value, the variance in area are about 3-fold smaller for both the CP1 and CH1 membranes.

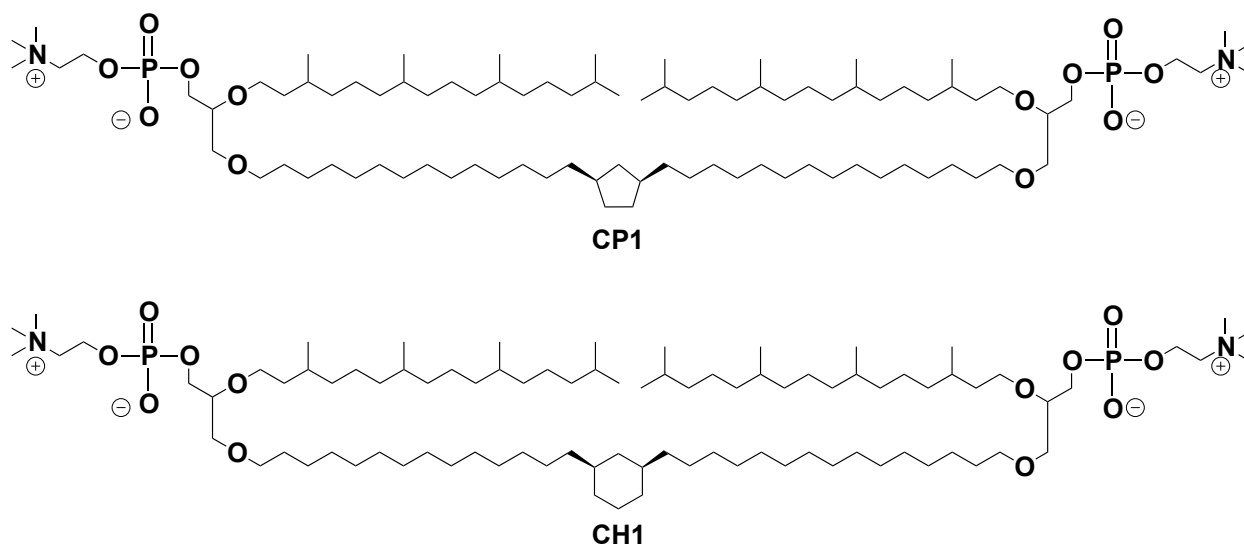


**Figure 50.** Lipids with cyclopentane (CP1) and cyclohexane (CH1) rings.

The smaller variance in area per lipid would indicate a material with a larger isothermal compressibility, and we might also expect the lipid mobility to be decreased. When we look at the diffusion behavior for the CP1/CH1 lipids we see that they are both much less mobile than the T32 lipid, but they are very similar to each other (**Figure 51**). Although we do not show the fluctuation plots, the membranes of CP1 and CH1 are also stiffer than T32, each with bending moduli in the 5000-6000 pN nm range as compared to the 3960 pN nm value for T32.

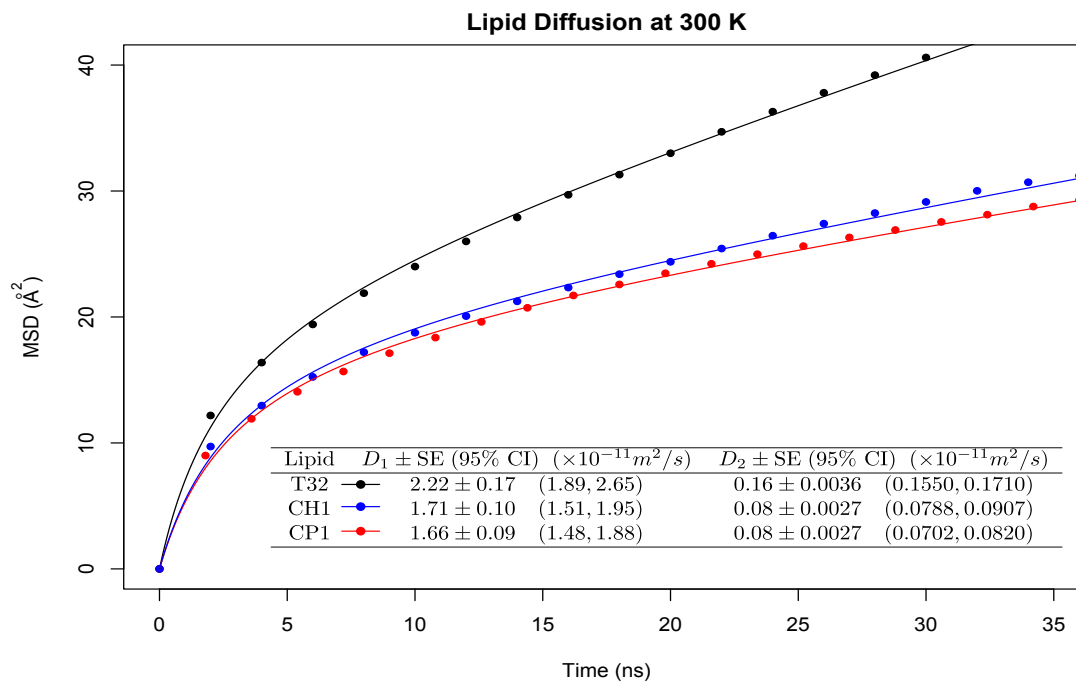


**Figure 51.** Mean-square displacement versus time for T32, CP1 and CH1 membranes.

Water penetration is also significantly decreased for the CP1 and CH1 membranes. As shown in **Figure 52**, the number of observations with 3+ waters are about 20% lower than for T32. In our T32 simulations we saw 25 events over a 50 ns span while CP1 and CH1 show 20-22 events over the same time period. This should correspond to a lower permeation rate, and this is consistent with experimental studies from the Yang group.

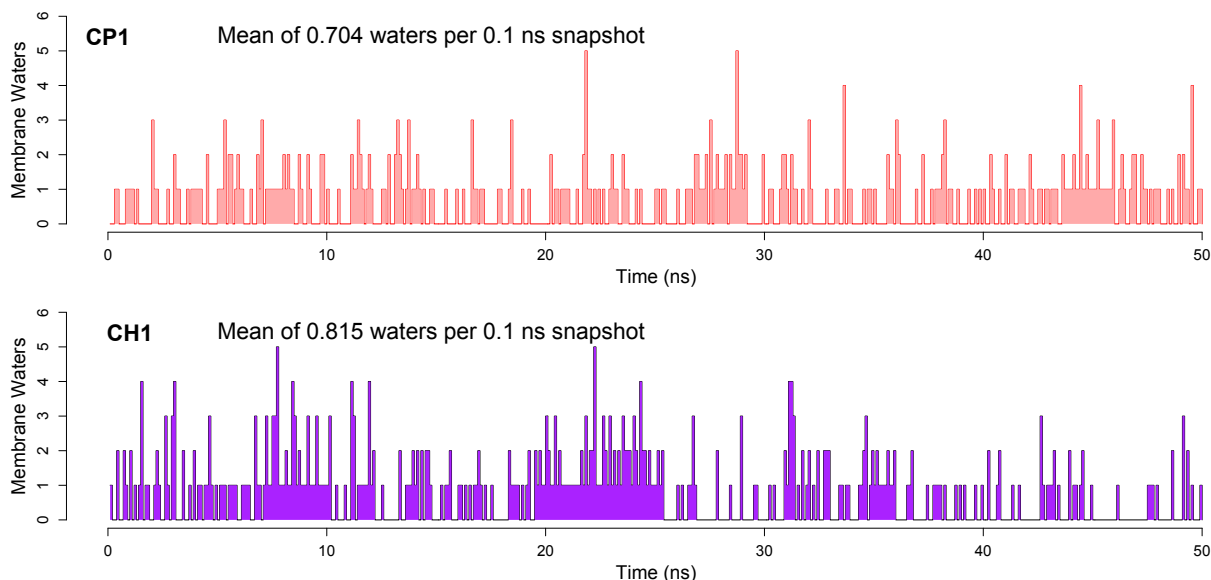


**Figure 52.** Water penetration into the hydrophobic core of the CP1 and CH1 membranes.

The Gianneschi group has synthesized a number of other novel lipids with triazole rings within the lipid core. We looked at one structure with two triazole groups (DTZ) in the lipid tails (**Figure 53**). This structure is a deviation from lipid molecules we have simulated. The parameters for the triazole groups have been developed for several drugs and other small molecules and we were able to adopt parameters from there. The initial membrane assembly was normal and the system was well behaved in the heating stages, however during the

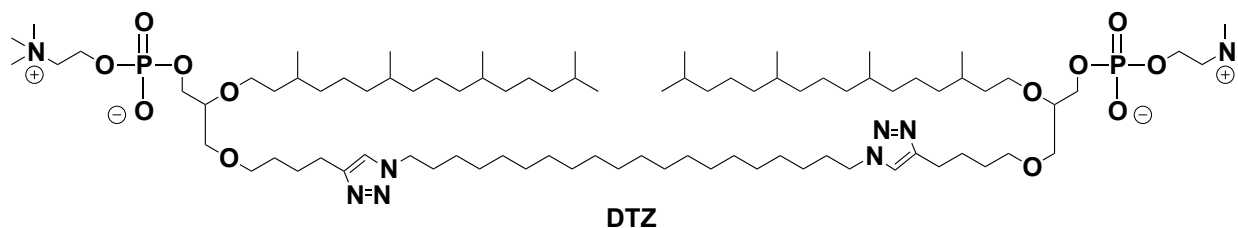


**Figure 53.** The chemical structure of the di-triazole lipid (DTZ).

equilibration and production runs the membrane appeared quite unstable. The area per lipid was similar to other lipids at  $65.3 \text{ \AA}^2$ , but the variance in the area was higher than any other lipid we have seen thus far ( $0.225 \text{ \AA}^4$ ). These large fluctuations result in significant water penetration into the hydrophobic core of the membrane and result in instability. As **Figure 54** shows the water penetration for an 81-lipid system (i.e. 9 times smaller than our other membranes).

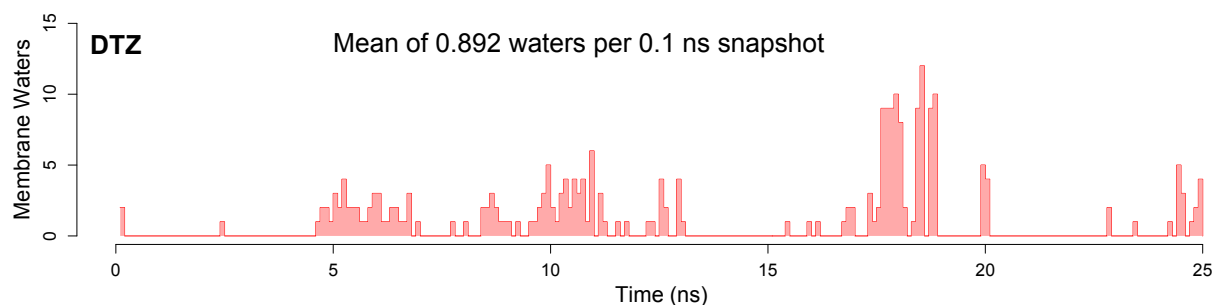


**Figure 54** Water penetration into an 81-lipid DTZ membrane. The maximum number of waters per area is about 25-30 times larger than for any other membrane we have studied.

Despite this smaller area, the rate of water entry and the maximum number of waters is 2-3 times higher observed for any other membrane. Given these results, it would seem that these lipids may not perform well in experimental studies.

#### 6.10. Simulation Studies of the GcGTPC-CH Lipid

The hybrid tetraether lipids described in section 3.3 were found to have exceptional with no observable leakage. In order to determine the molecular basis of this phenomena, we built membrane models using the GcGTPC-CH lipid to see how its structure and/or dynamics give rise to this function.

##### Area per Headgroup

Following the requisite heating and equilibration steps, we simulated a 729-lipid membrane (roughly  $200 \times 200 \text{ \AA}^2$ ) for more than 100 ns. As with all previous simulations, these were performed with 1 atm pressure coupling in the direction normal to the membrane and constant tension in the plane of the membrane. CHARMM36 parameters were available for cholesterol, so construction of the parameters files for the hybrid lipid were fairly straight-forward.

The area per headgroup is one of the more basic parameters to characterize. Previous theoretical work, most notably by Nagle, has opined that the permeability of a membrane is related to the area per headgroup (the “picket fence” model) or alternatively to the variance in the area per headgroup. When we look at the results for the GcGTPC-CH lipid and compare it to “standards” such as POPC (which has the same headgroup) we see that the area per headgroup is essentially identical, but the variance differs significantly (**Figure 55**).

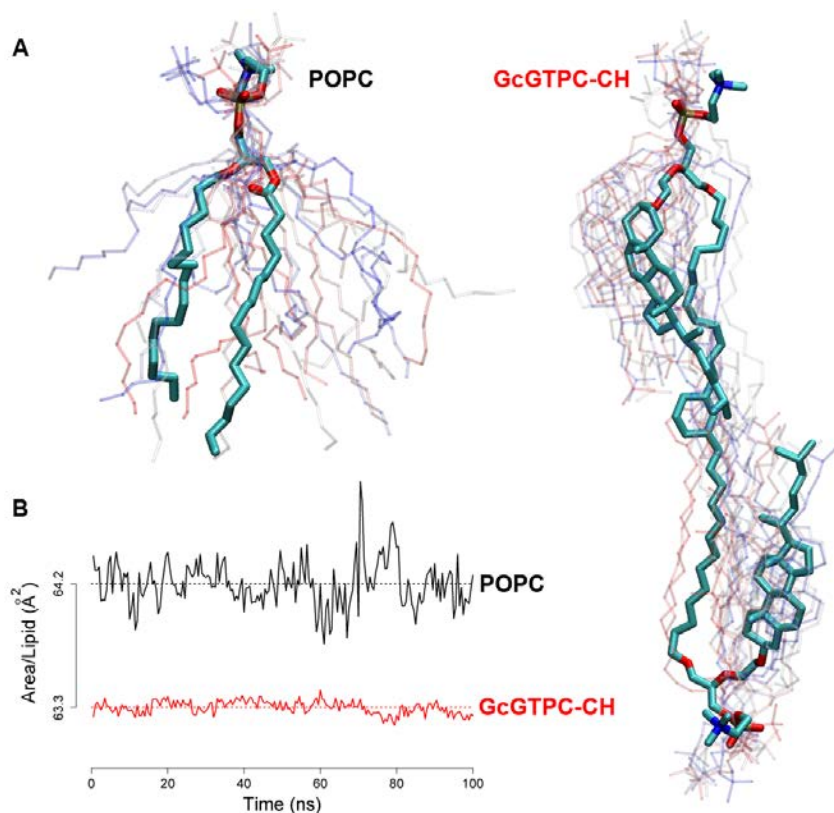


**Figure 55.** (A) Snapshots of POPC and GcGTPC-CH lipids from their respective simulations. (B) The corresponding area per lipid for these same two lipids. The areas only differ by 1-2%, but the variances differ by a factor of about 15.

Although POPC is a useful reference, a better comparison is with our family of tetraether lipids. In the table below we show the area per headgroup as well as the variance in the area per headgroup, each with their associated standard errors.

Lipid	Area/Lipid $\pm$ SE ( $\text{\AA}^2$ )	Var(Area/Lipid) $\pm$ SE ( $\text{\AA}^4$ )
POPC	$64.19 \pm 0.033$	$0.213 \pm 0.021$
T28	$63.72 \pm 0.015$	$0.047 \pm 0.005$
T32	$63.11 \pm 0.014$	$0.036 \pm 0.004$
T36	$64.43 \pm 0.018$	$0.063 \pm 0.006$
U16	$68.97 \pm 0.021$	$0.090 \pm 0.009$
<b>GcGTPC-CH</b>	$63.34 \pm 0.006$	$0.017 \pm 0.001$

**Table 3.** Area per lipid and the variance in the area per lipid for our collection of tetraether lipids, including the hybrid GcGTPC-CH.

The areas are all similar to each other and this is reasonable considering that the headgroups are identical. However, again we see that the variance in the area per lipid decreases with decreasing permeability, suggesting that this factor (or equivalently the isothermal compressibility) is a stronger determinant of overall permeation. Our experimental results suggest this is not a simple linear relationship, but the overall trend is clear.

## Lipid Diffusion

The self-diffusion of lipids in the membrane is another key property and provides insight into the material properties of the membrane. As a reminder, lipids exhibit two distinct phases of diffusion – a fast, local diffusion where the head group moves within the area defined by the surrounding lipids, and slower, long-time scale diffusion where the lipids move between each other. Wohler and Edholm showed that these two effects could be expressed in a single equation for the mean-square displacement as a function of time (Wohler and Edholm 2006)

$$\langle x(t)^2 \rangle = \frac{4D_1 t r_o^2}{r_o^2 + 4D_1 t} + 4D_2 t$$

In the above equation, the  $D_1$  diffusion constant describes the short timescale, local movement while  $D_2$  is the more conventional, long timescale diffusion constant. As shown in Table 10 and Figure 35, GcGTPC-CH has similar local diffusion properties, but the increased drag from the cholesterol moieties clearly slows down the long-range diffusion by a significant factor.

Lipid	$D_1 \pm \text{SE (95\% CI)}$ ( $\times 10^{-11} \text{m}^2/\text{s}$ )	$D_2 \pm \text{SE (95\% CI)}$ ( $\times 10^{-11} \text{m}^2/\text{s}$ )
T28	$2.43 \pm 0.12$ (2.18, 2.75)	$0.163 \pm 0.0055$ (0.151, 0.175)
T32	$2.80 \pm 0.11$ (2.57, 3.07)	$0.187 \pm 0.0028$ (0.181, 0.193)
T36	$2.05 \pm 0.17$ (1.73, 2.52)	$0.145 \pm 0.0114$ (0.116, 0.169)
U16	$3.43 \pm 0.19$ (3.06, 3.90)	$0.447 \pm 0.0051$ (0.436, 0.458)
POPC	$4.70 \pm 0.17$ (4.37, 5.09)	$0.651 \pm 0.0031$ (0.645, 0.657)
<b>GcGTPC-CH</b>	$2.36 \pm 0.12$ (2.13, 2.64)	$0.022 \pm 0.0015$ (0.019, 0.026)

**Table 4.** The local and long-range diffusion constants for POPC and a selection of our tetraether lipids, including GcGTPC-CH.



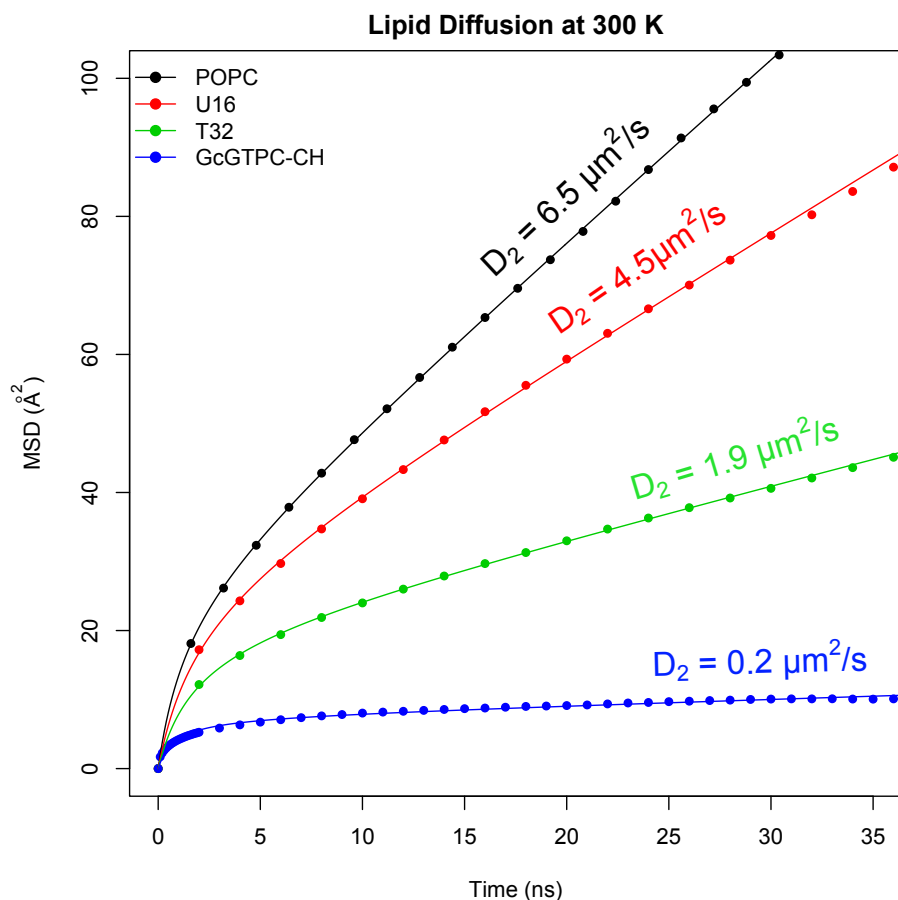


**Figure 56.** The mean-squared displacement (MSD) for POPC and some of the tetraether lipids. The GcGTPC-CG lipid exhibits limited diffusion due to the tremendous drag in the membrane.

## Water Penetration

One of our most interesting finding last year was the fact that the frequency of water penetration into the membrane. It is important to note that this is *penetration* and not *permeation*, however the rate of water entry should give some rough measure of the partition coefficient, and this is a key determinant of permeability.



We determined empirically that the number of observations of three or more waters in the hydrophobic core of the membrane correlated extremely well with the measured permeation coefficient. **Figure 57** shows observations of membrane waters over 50 ns of simulation time.

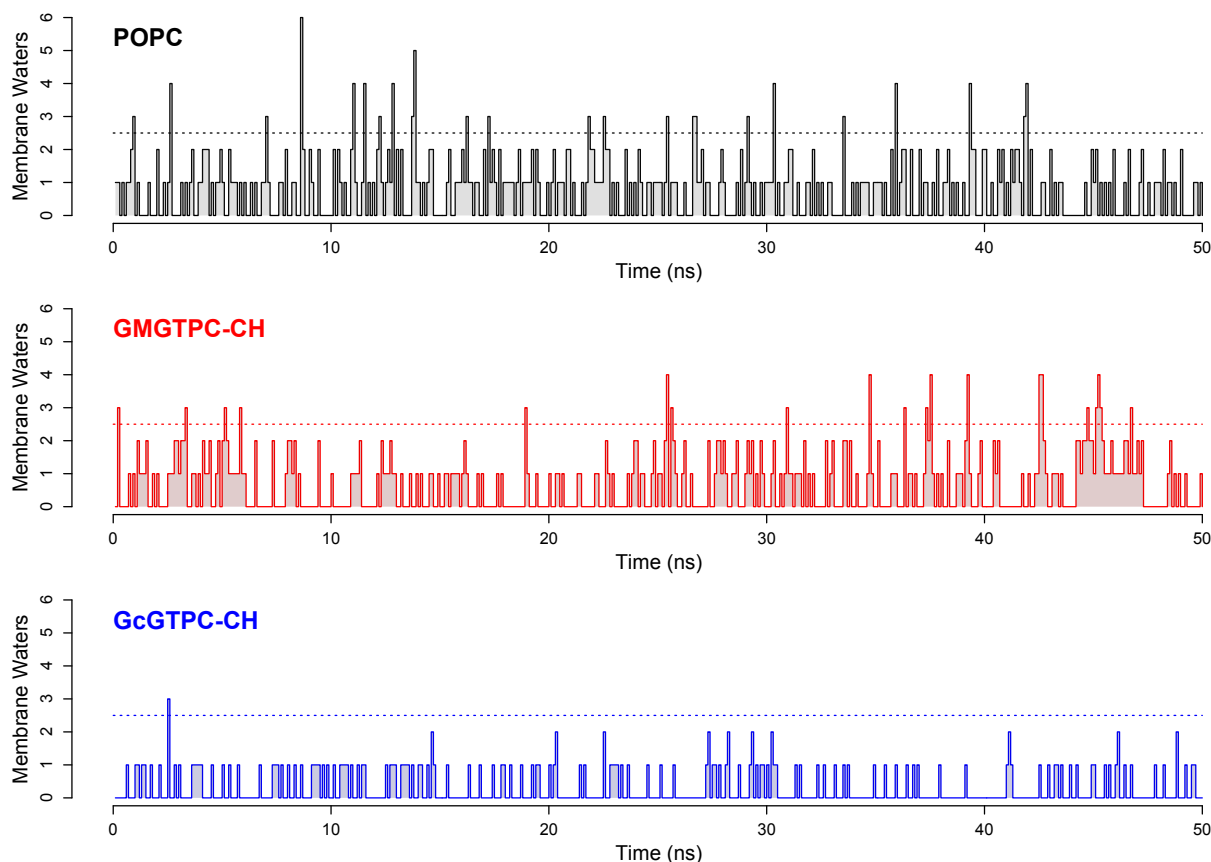


**Figure 57.** Observations of waters in the hydrophobic core of membranes constructed of POPC, GMGTPC-CH and GcGTPC-CH lipids.

POPC has a larger permeation coefficient and clearly allows more water into the core. A tethered lipid with a central cyclohexane ring admits fewer waters, however the cholesterol hybrid lipid (GcGTPC-CH) has only a single event over the 50 ns.

### Lipid Dynamics

When we compare the conformation dynamics of a single lipid within the membrane, we gain a much better sense of the dynamics that occurs within the hydrophobic core. **Figure 58** shows the range of conformations for a single lipid in the membrane. POPC clearly has the greatest range of motion and GcGTPC-CH has the least. The configurational entropy for these two lipids differs by a factor of about  $\sqrt{5}$ , consistent with the observation that the conformational space is roughly 5 times less for GcGTPC-CH (considering two molecules of POPC and one of

GcGTPC-CH). This increased order within the membrane introduces an additional entropic barrier to permeation (discussed in our 2015 report).

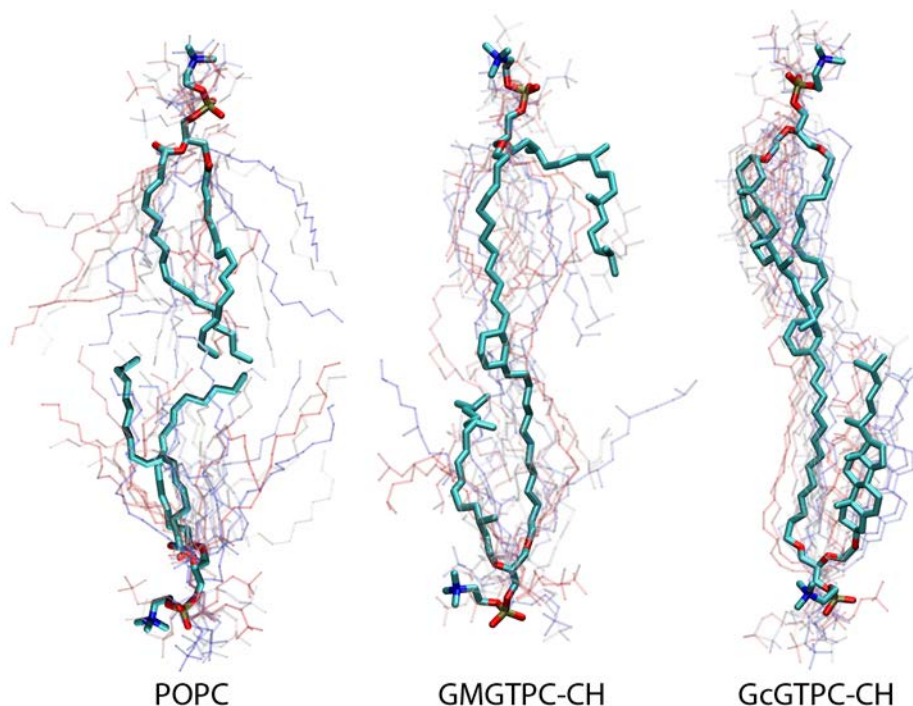


**Figure 58.** Conformational dynamics of POPC, GMGTPC-CH and GcGTPC-CH lipids. These are 20 individual snapshots taken at 5 ns intervals along the simulation.

## Summary

The hybrid GcGTPC-CH lipid has a number of interesting and interrelated biophysical properties. It exhibits a large lateral isothermal compressibility, as evidenced by the small variance in the area per headgroup, it has a very small long-range lateral diffusion constant, and it admits very few waters into the hydrophobic core of the membrane. The exact relationship between these parameters is not clear, but the combination is clearly linked to low permeation. Future work will hopefully be able to use these results to develop a more complete theoretical basis for permeation that explains a wider range of lipid structures.

## References

- Israelachvili, J. N. (1995). Intermolecular and Surface Forces. London, Academic Press.
- Watson, M. C., E. S. Penev, P. M. Welch and F. L. Brown (2011). "Thermal fluctuations in shape, thickness, and molecular orientation in lipid bilayers." J Chem Phys **135**(24):

244701.

Wohlert, J. and O. Edholm (2006). "Dynamics in atomistic simulations of phospholipid membranes: Nuclear magnetic resonance relaxation rates and lateral diffusion." J Chem Phys **125**(20): 204703.

## 7. Self-powered, photovoltaic-based ion sensing

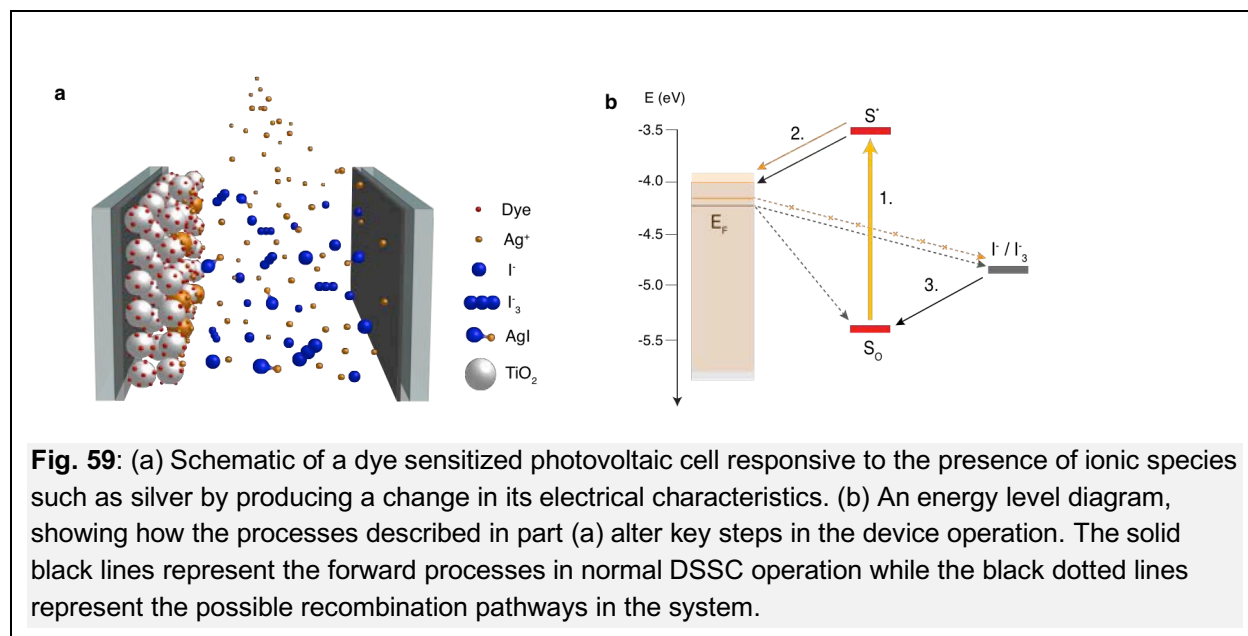
### 7.1. Dye-sensitized photovoltaic device-based platform

#### 7.1.1. Motivation

Since its inception, dye-sensitized solar cell (DSSC) technology has demonstrated adequate stability, low cost and ease of fabrication while being able to maintain competitive power conversion efficiencies for some applications. This platform is particularly compatible with detecting species in solution, because rapid charge transport in high efficiency DSSCs occurs in a liquid or gel electrolyte. Although some sensors incorporating solar cells as separate power modules have been previously demonstrated, such devices are typically complex and costly. Our approach allows for highly reproducible ion sensing to be achieved using a compact, low-cost device that powers its own operation.

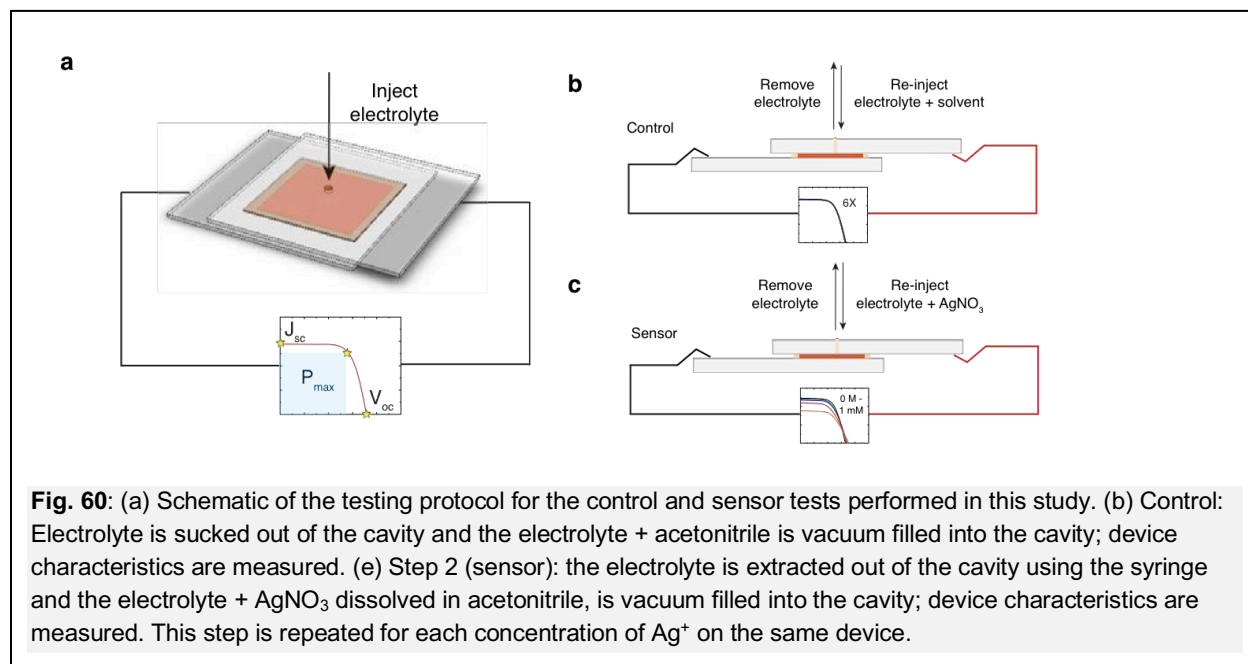
#### 7.1.2. Concept

We developed a sensing scheme in which the presence of ionic analytes disrupts (or triggers) the flow of electrical current between two electrodes, with the electromotive force ultimately provided by absorbed ambient light. For the proof-of-concept demonstration, we examine a ‘turn off’ type mode of operation where the presence of  $\text{Ag}^+$  ions shuts off photocurrent production in a classical dye-sensitized solar cell structure consisting of cis- bis(isothiocyanato)bis(2,2'-bipyridyl-4,4'-dicarboxylato)-ruthenium (II) sensitizing dye (N3) and the iodide/triiodide redox shuttle. In this scheme, the device operates optimally to begin with and then sees a photocurrent drop in response to a detection event, such as adsorption of the analyte on to an electrode or quenching of the dye excited state. (**Fig. 59(a)** and **(b)**) The ionic species can also be generated using an auxiliary release mechanism so as to allow for indirect detection of biological analytes.

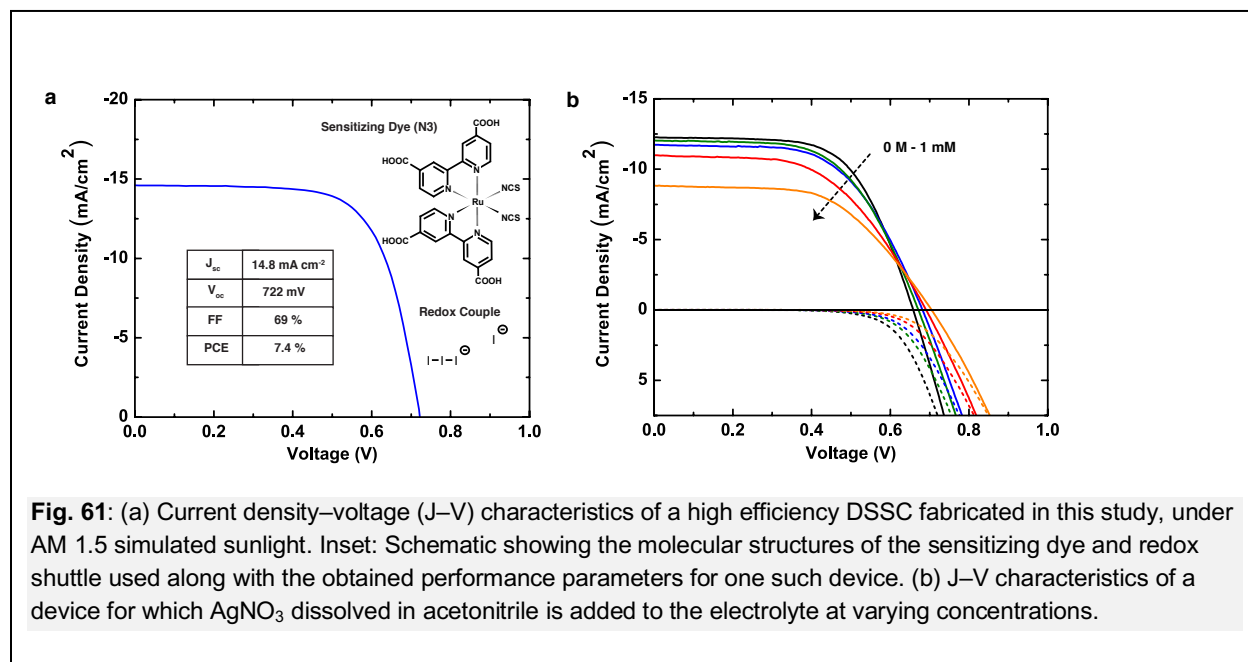


### 7.1.3. Main Results & Conclusions

**Sensing Protocol:** After the devices were assembled the electrolyte was introduced into the cavity formed between the two glass substrates through a 0.5 mm diameter hole in the counter electrode, using a vacuum syringe. We then performed identical tests on two sets of devices – a) Control devices, wherein a fixed volume of pure solvent was added to the device in addition to the electrolyte and b) Sensors, wherein silver nitrate dissolved in acetonitrile was injected into the device in addition to the electrolyte, at concentrations ranging from 1 nM to 10 mM. (**Fig. 60**)



The electrical characteristics and impedance spectra for each of these two sets of devices are then measured under 1 sun illumination and in the dark as seen in **Fig. 61**.



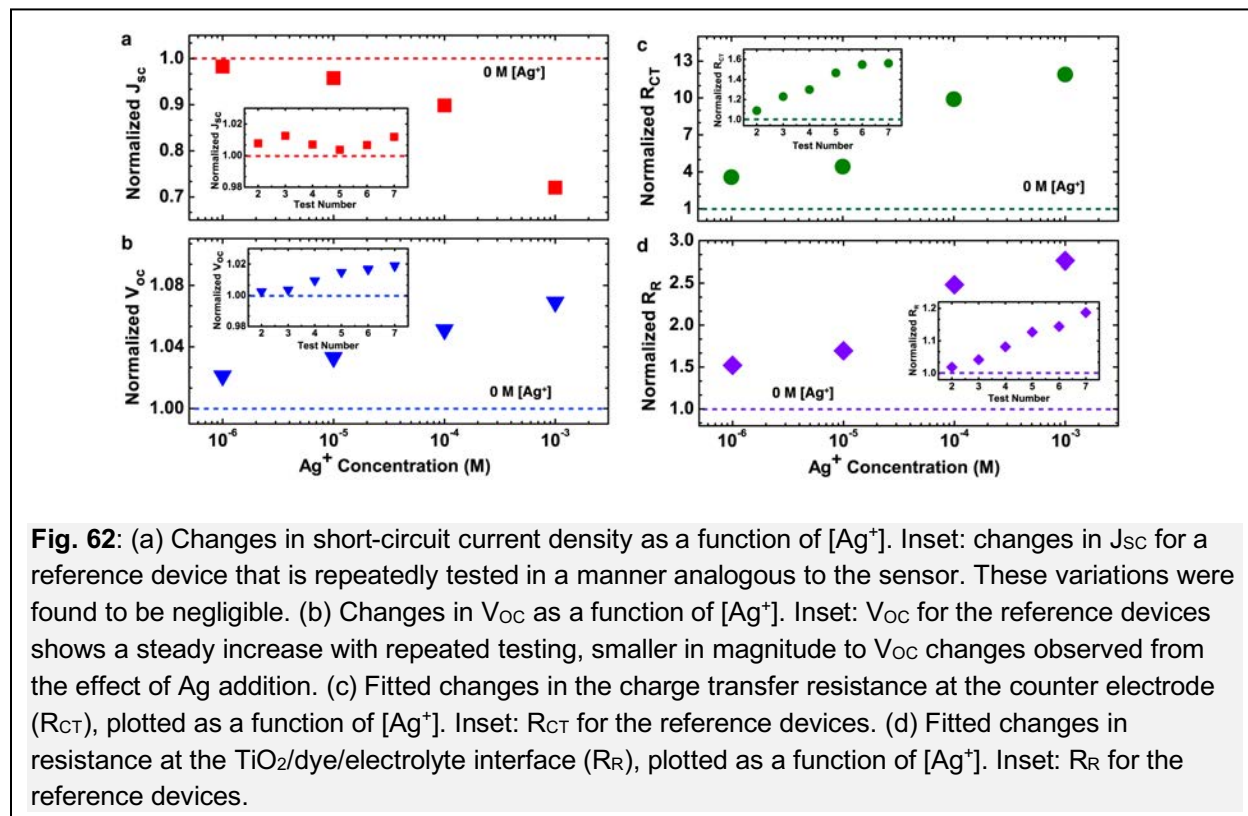
#### 7.1.4. Electrical Characterization

The changes in device response in the presence of  $\text{Ag}^+$  are shown in **Fig. 62**. The practical utility of this scheme is manifested in the observation that the power conversion efficiency of the device never drops below 70% of its original value, thus ensuring that sufficient power is generated to modulate the intensity of an external circuit element even when a very high concentration of the analyte is present in the electrolyte. The  $J_{sc}$  and  $V_{oc}$  obtained from these measurements were plotted as a function of  $\text{Ag}^+$  concentration. A distinct drop in  $J_{sc}$ , accompanied by a steady increase in  $V_{oc}$  was observed for concentrations of  $\text{Ag}^+$  ranging between 1  $\mu\text{M}$  and 1 mM. Concentrations of  $\text{Ag}^+$  below 1  $\mu\text{M}$  did not cause an appreciable change in the device characteristics, while concentrations greater than 1 mM caused the device to become resistive.

#### 7.1.5. Electrochemical Impedance Measurements

We also performed electrochemical impedance spectroscopy (EIS) measurements and fitted the obtained data to an equivalent circuit model to obtain the resistances corresponding to electron recombination at the  $\text{TiO}_2/\text{dye}/\text{electrolyte}$  interface ( $R_R$ ), and to charge transfer through the counter electrode ( $R_{CT}$ ). As **Fig. 62(c)** and **(d)** show, there is a dramatic increase in both of these parameters with the addition of  $\text{Ag}^+$ , attributable to the formation of electrodeposited silver clusters and/or the reduction of silver iodide precipitate on the  $\text{TiO}_2$  electrode to metallic silver.

under illumination. In both cases, charge transport is inhibited and the precipitate may render some dye sites inactive, while also blocking electron recombination at the  $\text{TiO}_2/\text{dye}/\text{electrolyte}$  interface.



#### 7.1.6. SEM/EDX Measurements

Energy-dispersive X-ray spectroscopy (EDS) was performed on the  $\text{TiO}_2$  electrode following the  $\text{Ag}^+$  sensing experiments, confirming the formation of silver clusters, as seen in **Fig. 63**. Furthermore, optical microscopy and scanning electron microscopy of the  $\text{TiO}_2$  electrode revealed that a large proportion of the silver clusters are concentrated directly underneath the electrolyte-filling hole, due to the larger concentration driving force and a thinner boundary layer directly below the injection site. The limit of detection may be significantly improved by concentrating light in this region of the device, or by replacing the glass support for the counter electrode with a porous membrane that would eliminate the need for a filling hole, thereby allowing the analyte to interact homogeneously with the entire device area.

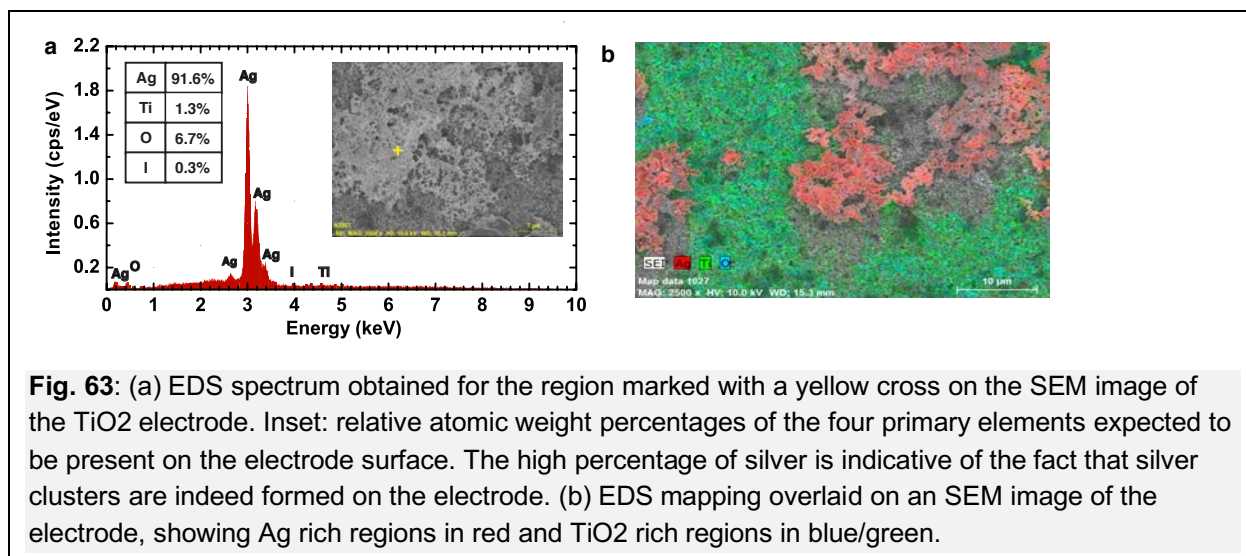


**Fig. 63:** (a) EDS spectrum obtained for the region marked with a yellow cross on the SEM image of the TiO<sub>2</sub> electrode. Inset: relative atomic weight percentages of the four primary elements expected to be present on the electrode surface. The high percentage of silver is indicative of the fact that silver clusters are indeed formed on the electrode. (b) EDS mapping overlaid on an SEM image of the electrode, showing Ag rich regions in red and TiO<sub>2</sub> rich regions in blue/green.

## 7.2. Chemiluminescence (CL) based sensing

### 7.2.1. Motivation:

Chemiluminescence (CL) based sensing, wherein a chemical reaction involving an analyte of interest results in light emission, is applicable to enzyme detection, DNA sequencing, treatment diagnostics, environmental monitoring and a wide range of other chemical and biological assays where high sensitivity and selectivity are essential requirements. [1 - 3] In comparison with other types of commonly used sensing techniques, CL based sensors do not require an external light source [4] and have a high potential for miniaturization and integration with microfluidic flow cells. Although a considerable amount of research has been dedicated to the development of CL-based chemistry in recent years, the hardware used to collect the CL signal has typically been a sophisticated, high-responsivity detector such as a photomultiplier tube (PMT) or a camera equipped with a charge couple detector (CCD) focal plane sensor [5, 6]. Indeed there have been demonstrations of more compact detectors such as those based on hydrogenated amorphous silicon (a-Si:H) [7] and organic polymers [8], that have shown performance metrics comparable to those obtained with PMTs. We demonstrate a simple setup that is compatible with any kind of CL assay and photodetector. When applied to the detection of fluoride (F<sup>-</sup>) ions in conjunction with a standard Si photodetector, a 100 nM detection limit was observed, with substantially higher performance possible. (Sub-nM detection was also observed for a limited number of experiments, currently being verified.)

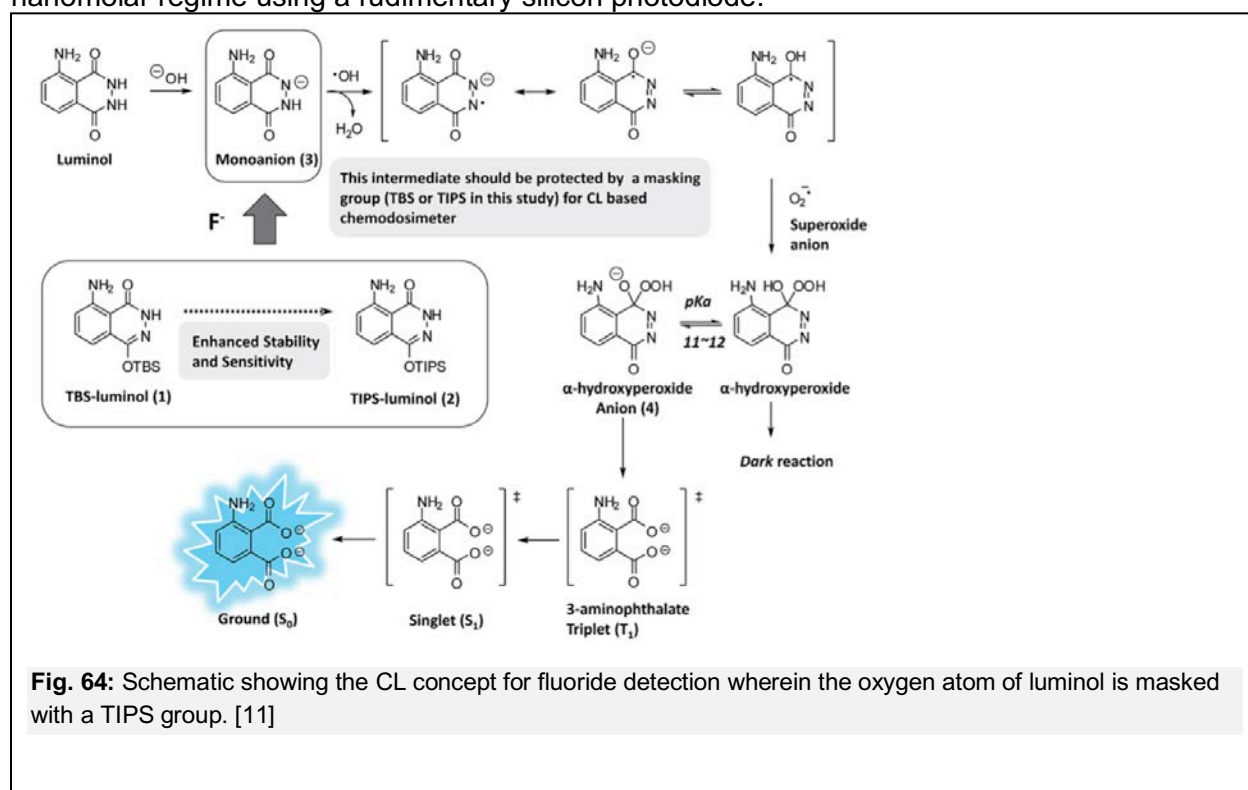
### 7.2.2. CL assay for Fluoride detection:

One of the key problems associated with CL based detection protocols is the complexity of the chemical reaction itself. Most CL protocols use luminol, a well-known chemical that emits light when oxidized. The target analyte is typically labeled with a semiconducting nanoparticle or quantum dot [9, 10] that engages in chemiluminescence based resonant energy transfer



(CRET) with the luminol. This step is often inefficient and limits the intensity of the CL signal. Recently, a new type of CL based sensory system with a built-in self-signaling feature that bypasses the CRET step was demonstrated. [11] This was accomplished by incorporating a masking group to luminol that efficiently suppresses its CL in the absence of an analyte. The masking group is selected such that it can selectively be removed only by the target analyte and this restores the CL signal. This concept was used to detect fluoride anions in an aqueous environment and a detection limit of 18 nM was established by masking luminol with a triisopropylsilyl (TIPS) moiety as shown in **Figure 64**. The fluoride ion removes the TIPS making group from the oxygen atom of luminol and allows the conversion of luminol to its monoion adduct. The reaction then proceeds as expected, emitting bright blue light.

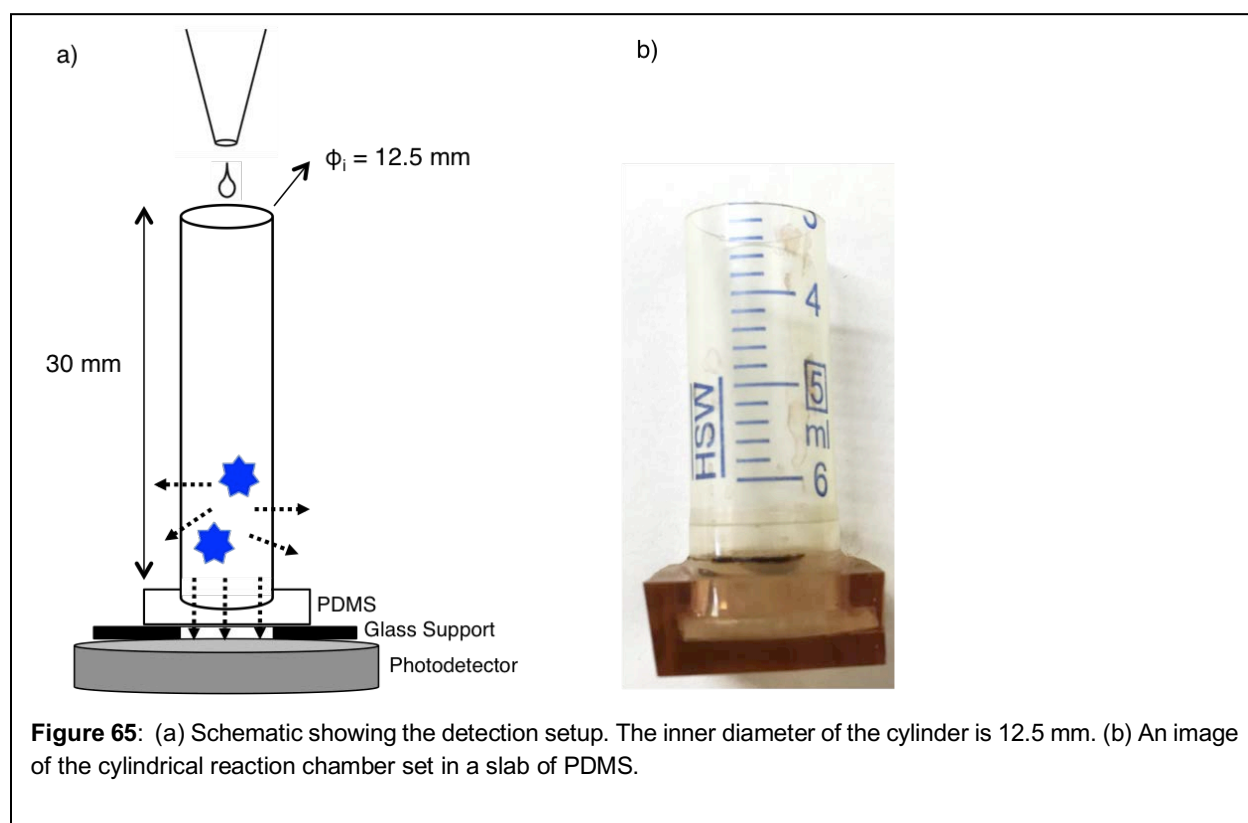
Sensitive detection of fluoride is critical to a large number of applications ranging from water treatment to chemical warfare agents [12, 13], but the detection limit of 18 nM demonstrated using the aforementioned CL assay, is the best reported so far [14 – 17], and falls short of many application requirements. There is clearly a need for further sensitivity enhancement, and the result demonstrated here can be further improved upon to reach detection limits in the single nanomolar regime using a rudimentary silicon photodiode.



### 7.2.3. Detection setup & Sensing protocol:

The photodetector used in this study was a model 818 silicon photodetector from Newport that has a typical responsivity value of 0.25 A/W at 430 nm, the wavelength overlapping with the peak of CL of luminol. The active area of the detector was 1 cm<sup>2</sup>. A chamber into which the solutions containing the analyte and the TIPS-luminol were introduced was placed directly atop the photodetector.

The reaction chamber is comprised of a cylindrical tube having an inner diameter of 12.5 mm and an outer diameter of 13 mm, constructed from a polypropylene syringe barrel with an open top and a sealed bottom. This cylinder is set in a 7 mm thick slab of polydimethylsiloxane (PDMS) and placed atop a 1" x 1" glass slide. The glass slide is masked off with black electrical tape to minimize stray reflections expect for a 15 mm x 15 mm square opening in the center, that is aligned with the bottom of the cylinder. This assembly is then placed directly onto the photodetector as shown in **Figure 65**. No index matching fluid was used. The collection efficiency of the setup estimated to be 0.35% is discussed further in Section 4.5. This is expected given that a considerable amount of light leakage occurs through the transparent sidewalls and the top opening.



Experiments to detect fluoride ions were performed as per the procedure described in Ref. 11. A solution consisting of 400  $\mu\text{L}$  of each of the following three compounds –  $\text{Co}(\text{NO}_3)_2$  ( $5 \times 10^{-4}$  M),  $\text{H}_2\text{O}_2$  ( $2 \times 10^{-2}$  M) and  $\text{Na}_2\text{CO}_3/\text{NaHCO}_3$  (0.1 M) – in de-ionized water was first added to the reaction chamber. Subsequently, a 200  $\mu\text{L}$  solution containing only TIPS-luminol ( $1.7 \times 10^{-3}$  M) in tetrahydrofuran (THF) was added to the DI water solution in the reaction chamber. This is done to establish a baseline for our tests, since it is known that some light emission can be expected from the unmasked luminol impurities present in the TIPS-luminol solution even in absence of the target analyte. The photodetector current resulting from the CL signal is recorded in 10

millisecond steps for 450 seconds using an Agilent 4156B semiconductor parameter analyzer. This time duration for signal integration was chosen since our data indicates that the TIPS-Luminol emission does not decay completely up until 350 – 400 seconds after initial injection. We note that THF is chosen as a solvent primarily due to the poor solubility of TIPS-luminol in water but this may potentially be improved via chemical modification of the compound or by introducing additional steps to the assay.

#### 7.2.4. Main Results & Conclusions:

Once a baseline has been established, the sensing test is repeated, this time with a solution containing 100  $\mu\text{L}$  TIPS-luminol ( $3.4 \times 10^{-3}$  M in THF) and 100  $\mu\text{L}$  of varying concentrations of tetrabutylammonium fluoride (TBAF) in THF as a source of fluoride ions. When this solution is added to the water mixed solution of cobalt nitrate, hydrogen peroxide and sodium carbonate/sodium bicarbonate, light emission of varying intensities is observed as expected.

**Figure 66** shows the measured photodetector current as a function of time for the entire duration of the CL emission, with the start of the measurement coinciding with the injection of the TIPS-luminol into the reaction chamber. This is important since, based on our data, the emission intensity typically peaks within the first 10 seconds of injection for most cases. Note that the numbers in the legend correspond to the concentration of  $\text{F}^-$  in the droplet, without accounting for dilution upon the introduction of the droplet into the chamber.

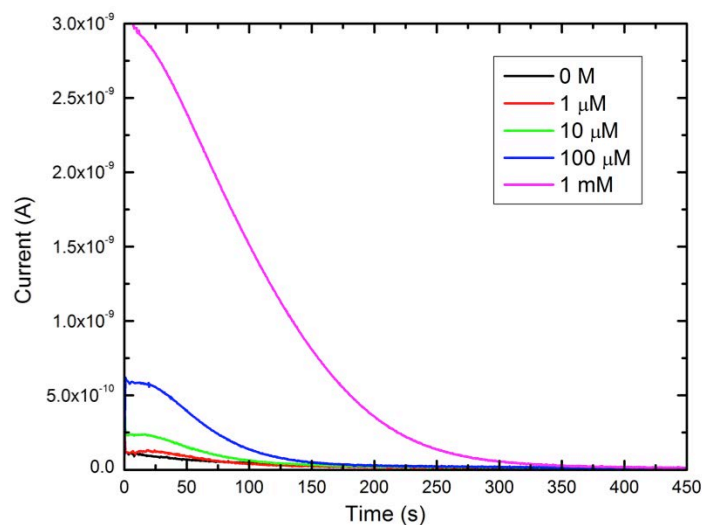


**Figure 66:** Photodetector current as function of time corresponding to the CL signal from the presence of fluoride ions.

The photodetector current was then integrated over the duration of the CL emission; subtracting from it the background, we obtained the contribution from the emission signal from TIPS-luminol alone. It is important to note that since mixing typically occurs by diffusion and is not instantaneous, the concentration of  $\text{F}^-$  in the reaction chamber, relative to the volume of fluid in which the contents of the droplet are dispersed, is much higher at the start of the test than at the

end. To address this discrepancy, we plot the charge collected by the photodetector both as a function of  $F^-$  concentration in the droplet and as a function of the  $F^-$  concentration in the solution as shown in **Figure 67**. Since detection limits are typically reported after accounting for dilution, the detection limit in our case would be 100 nM.

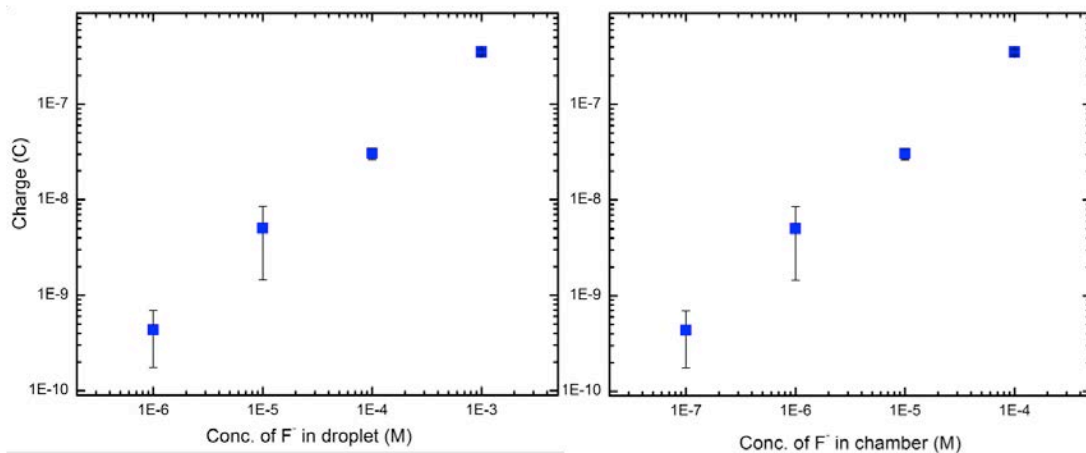


**Figure 67:** Total charge collected by the photodetector over the duration of CL emission as a function of fluoride ion concentration (a) in the droplet (b) in the solution. The error bars for the two highest concentration data points are too small to be seen on this plot.

Since the concentration of  $F^-$  in the droplet is smaller than that of TIPS-Luminol,  $F^-$  is the rate limiting reagent and the total number of photons emitted can be calculated as follows:

$$N_e = V\phi[F^-]N_A$$

where,  $V$  is the volume of the droplet that contains TBAF i.e. 0.1 ml,  $\phi$  is the quantum yield of TIPS-Luminol (assumed to be 1%, similar to that of Luminol),  $[F^-]$  is the concentration of TBAF in the droplet that is introduced into the reaction chamber along with the TIPS-Luminol and  $N_A$  is Avogadro's constant. The calculation assumes that every fluoride ion successfully unmaskes one TIPS-Luminol molecule and is consumed in this reaction. The optical collection efficiency of the reaction chamber may then be estimated as the ratio of the number of photons incident on the photodetector to the total number of photons emitted, for a given concentration of  $F^-$  as shown in **Figure 68**. This results in an average optical collection efficiency of 0.35% for the setup.

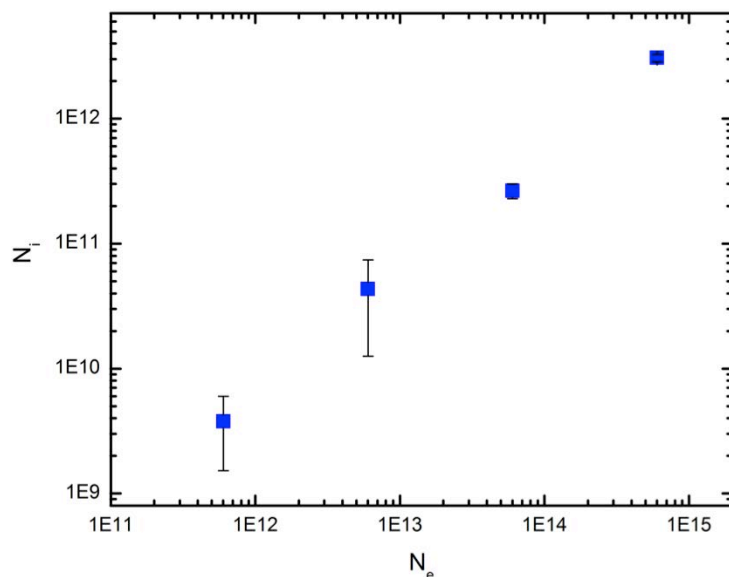


**Figure 68.** Total number of photons emitted ( $N_e$ ) vs. the total number of photons incident on the photodetector ( $N_i$ ) for increasing concentrations of  $F^-$  from left to right.

The recently demonstrated best detection limit of 18 nM by M. S. Kwon et al. – an order of magnitude lower than that realized with our setup – was measured using a high-sensitivity multi-mode PMT (PTI model 914) that has a responsivity of  $10^5$  A/W at 430 nm, six orders of magnitude higher than the responsivity of the silicon photodetector used in this study. This suggests that improvements in the collection efficiency of the reaction chamber should result in detection limits that are in the low nanomolar range. Alternatively, a high responsivity photodetector such as an avalanche photodiode may be integrated with the setup demonstrated here to achieve even better results.

To improve the collection efficiency of the reaction chamber, we used an optical concentrator akin to a miniaturized integrating sphere that may be constructed by bonding together two parabolic multifaceted reflectors bonded together as shown in **Figure 69**. The collection efficiency of this type of reaction chamber is ~50%, two orders of magnitude higher than that of the setup demonstrated previously. This allows for the detection of fluoride ions down to single nanomolar concentrations without the use of a high responsivity detector. In addition to fluoride ions, this setup can also be used to detect very small concentrations of ferricyanide ( $[Fe(CN)_6]^{3-}$ ) ions in solution using a luminol based chemiluminescence assay. We previously reported that concentrations of ferricyanide ions down to 1 nM can be detected using the simple cylindrical holder setup using this assay and we believe that this result can be improved upon using the optical concentrator design.

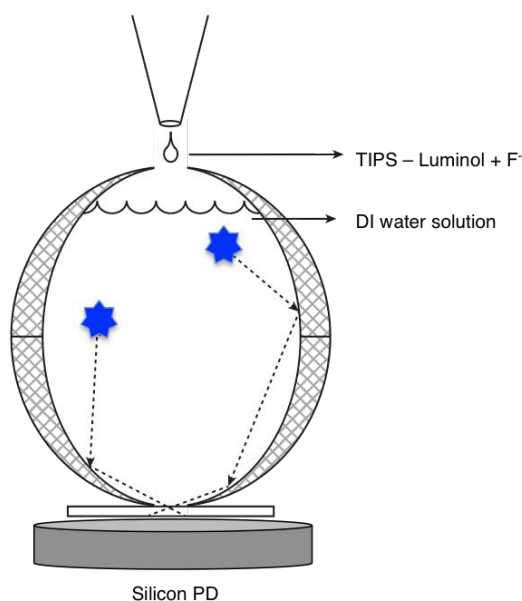


**Figure 69:** Schematic showing the miniaturized optical concentrator concept.

The setup discussed above can be the basis for radically improving the performance of point-of-care diagnostic devices and other medical applications, which require miniaturization and monolithic integration of the chamber and detector components with microfluidic flow cells. One proposed method to realize this is by molding a hemi-spherical concentration chamber out of PDMS or polymethylmethacrylate (PMMA), coated with a reflective film using microscale patterning techniques [18] such as soft lithography. [19] This component may then be integrated with a flexible organic photodetector, shown in **Figure 70**, to realize a compact, disposable device that can be cheaply fabricated.

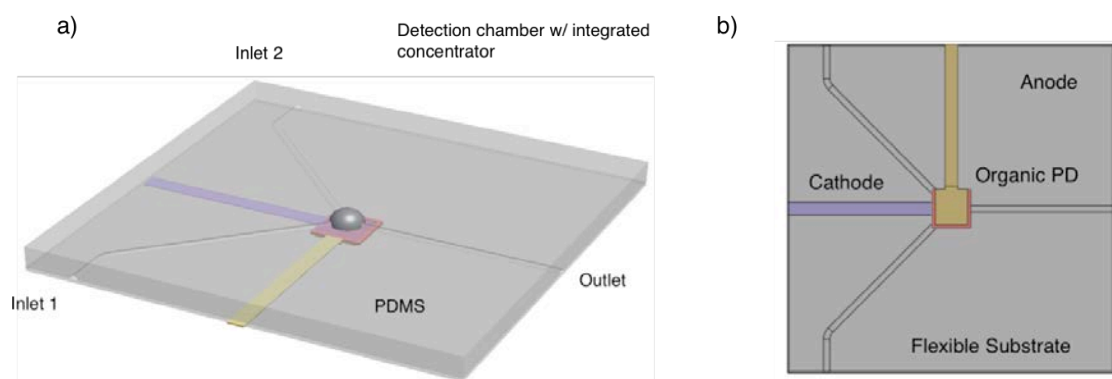


**Figure 70:** Schematic of a proposed monolithic sensor that incorporates a miniaturized optical concentrator (a) Top view (b) Bottom view showing a flexible organic photodetector.

### 7.2.5. Summary:

In summary, a simple and inexpensive chemiluminescence based scheme for fluoride ion detection was demonstrated. The detection limit obtained was  $\sim 100$  nM, while the range extends across four orders of magnitude. The setup developed is compatible with all kinds of CL based assays and detectors, making it highly applicable to a wide range of chemical and biological applications. Future work may involve improving the optical collection efficiency of the reaction chamber as well as the development of a monolithic device.

### 7.3. Improving photodetector quantum efficiency

Previously, our integrated sensor design relied on a polymer-based organic photovoltaic device as the photodetector. The device exhibited  $\sim 4.5\%$  power conversion efficiency, with spectral coverage extending only to  $\sim 650$  nm wavelength. We identified several small molecular compounds whose absorption spectra (**Fig. 71**) and energy levels allowed us to develop a solar cell having the structure: ITO/5nm  $\text{MoO}_3$ /10nm TPTPA/10nm DBP/8nm SubNc/10nm  $\text{Cl}_6\text{SubPc}$ /36nm  $\text{C}_{60}$ /10nm BCP/100nm Ag, with absorption beyond 700 nm, external quantum efficiency above 50% for most of its absorption range, and power conversion efficiency of 7.3% (**Fig. 72**). This is a remarkable level of performance for a small-molecular, planar heterojunction solar cell, whose composition is particularly stable and amenable for long-term operation.

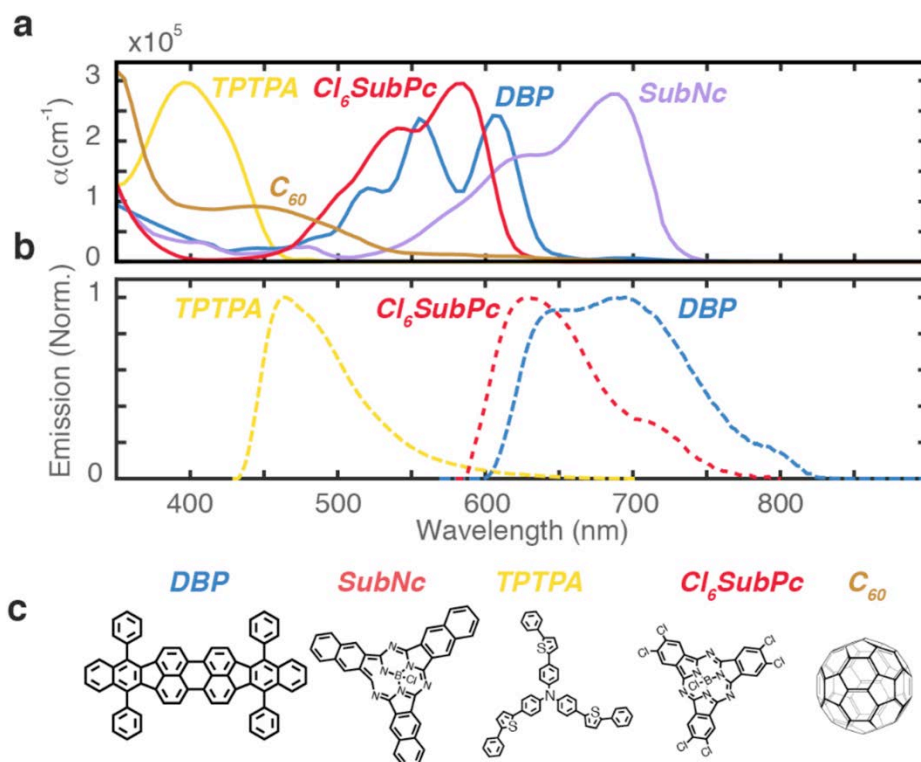


**Figure 71:** a) Absorption and b) emission spectra of all the active materials used in this study. c) Molecular structures of TPTPA, DBP, SubNc,  $\text{Cl}_6\text{SubPc}$ , and  $\text{C}_{60}$ .



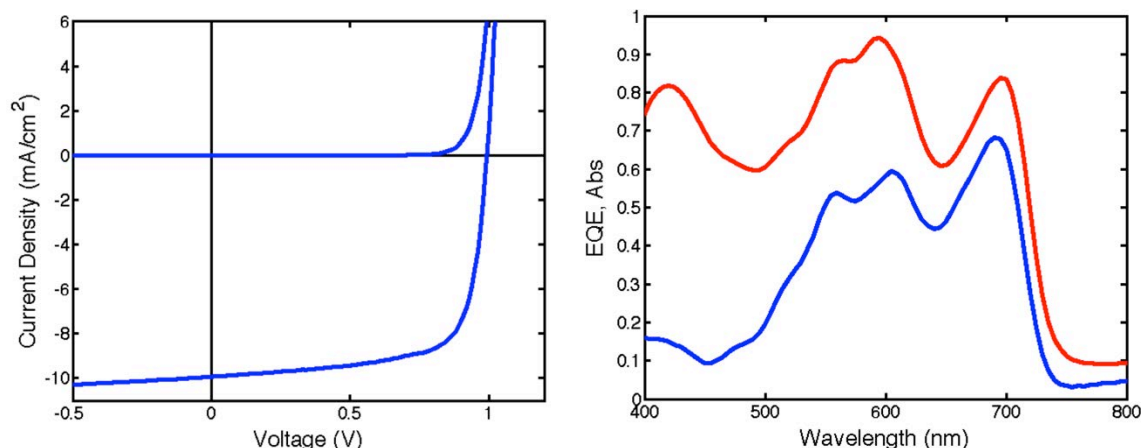


**Figure 72:** (left) Dark and AM1.5-illuminated current-voltage characteristic of thin-film, organic photovoltaic device having the structure ITO/5nm MoO<sub>3</sub>/10nm TPTPA/10nm DBP/8nm SubNc/10nm Cl<sub>6</sub>SubPc/36nm C<sub>60</sub>/10nm BCP/100nm Ag, exhibiting  $J_{sc} = 10 \text{ mA/cm}^2$ ,  $V_{oc} = 1 \text{ V}$ ,  $FF = 72\%$ ,  $PCE = 7.3\%$ ,  $J_{MPP} = 8.4 \text{ mA/cm}^2$ ,  $V_{MPP} = 0.76 \text{ V}$ .

We also developed a solar cell based on lead phthalocyanine (PbPc), template on layers of MeO-TPD and copper iodide (CuI), with absorption extending to 1200 nm (**Fig. 73**). The substantial spectral coverage extending beyond 750 nm suggests that creating a tandem cell with the 7.3% efficient cell above can further boost efficiency and enhance autonomous operation of the sensor.

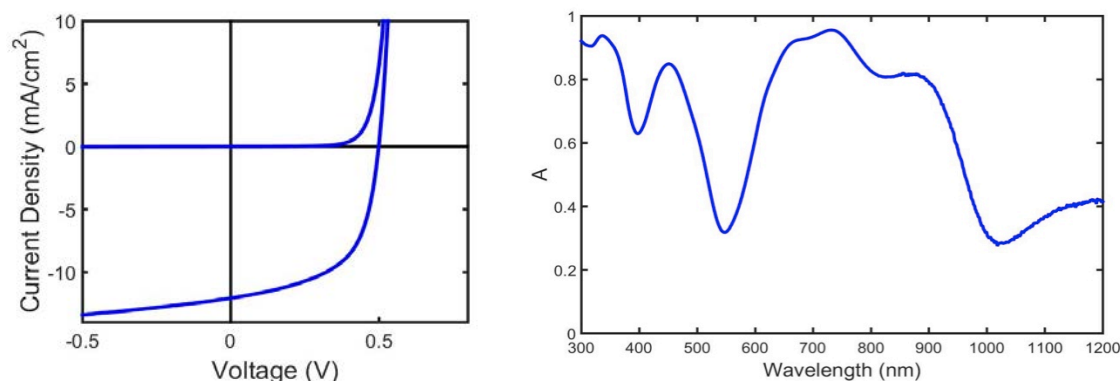


**Figure 73:** (left) Dark and AM1.5-illuminated current-voltage characteristic for a small molecular organic photovoltaic device having the layer structure: ITO/5nm MeO-TPD/1nm CuI/30nm PbPc/50nm C<sub>60</sub>/10nm BCP/100nm Ag, exhibiting  $J_{sc} = 10.4 \text{ mA/cm}^2$ ,  $V_{oc} = 0.49 \text{ V}$ ,  $FF = 57\%$ ,  $PCE = 2.95\%$ ,  $J_{mpp} = 7.68 \text{ mA/cm}^2$ ,  $V_{mpp} = 0.38 \text{ V}$ .

#### 7.4. Kirigami- and Origami-inspired structures for autonomous signal transduction

Advances in a different project (co-sponsored by the National Science Foundation and the Air Force through the EFRI ODISSEI program), are potentially useful in developing novel, active membranes that can be used for sensing (signal transduction) and mechanical actuation in the



presence of ions. **Figure 74** shows a kirigami structure made by laser-cutting Kapton, an aerospace-qualified plastic stable in extreme environments (e.g. >450°C, acidic, basic, aqueous or organic solvents, etc.). Upon stretching a cut sheet in a direction perpendicular to the cuts, such as the one shown in Fig. 11, buckling occurs in the transverse direction. The cut regions open up and tilt in proportion to the stretch. The Poisson ratio of the structure (ratio of axial to transverse strains) can be engineered **via** the cut geometry, as can the mechanical properties.

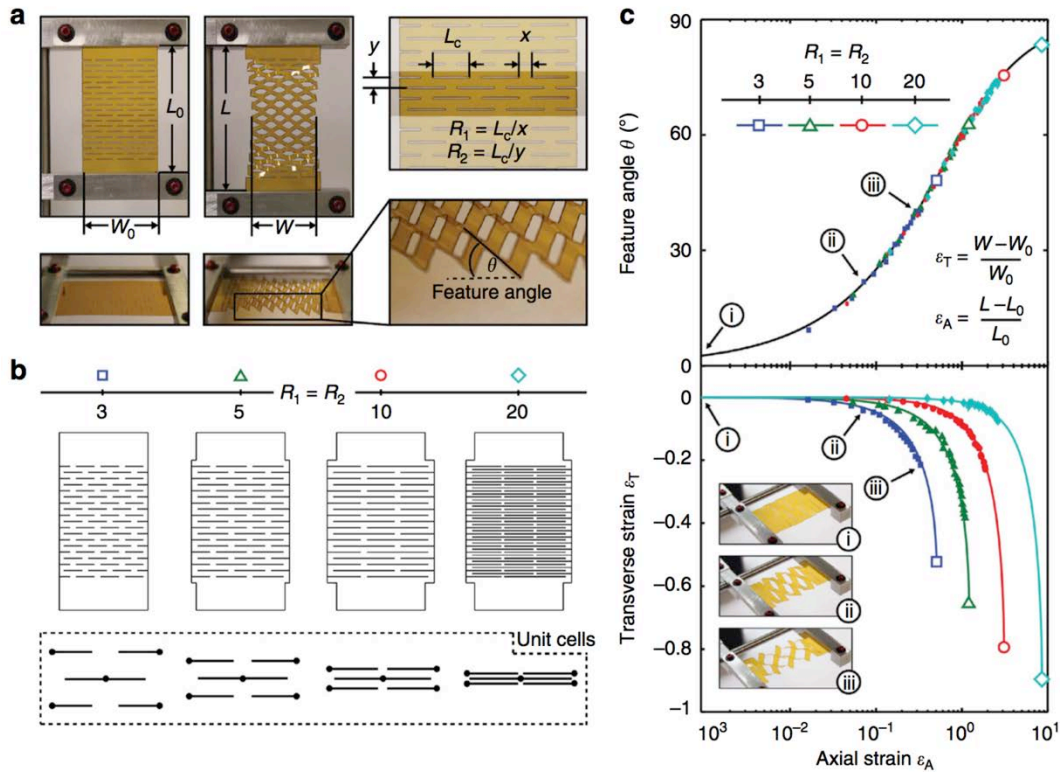


**Figure 74:** Kirigami cut geometry and geometric system response. (a) Response of a Kapton kirigami structure to stretching in the axial direction ( $\epsilon_A$ ) is accompanied by a decrease in sample width ( $\epsilon_T$ ) and a change in feature angle ( $y$ ). Also shown are the geometric parameters that define the kirigami structure, namely the cut length ( $L_c$ ) and spacing between cuts in the transverse ( $x$ ) and axial ( $y$ ) directions, which can be expressed in terms of the dimensionless parameters,  $R_1$  and  $R_2$ . (b) Schematics of four kirigami structures, where  $R_1 = R_2 = 3, 5, 10$  and  $20$ , along with their corresponding units cells. (c)  $\epsilon_T$  and  $y$  versus  $\epsilon_A$  for several kirigami structures where  $R_1 = R_2 = 3, 5, 10$  and  $20$  (b). Theoretical predictions per equations (1) and (2) are shown by solid lines, while the closed symbols represent experimental data from a 50 mm-thick Kapton sample of the appropriate geometry. While larger  $R_1$  and  $R_2$  enable increased axial strains and correspondingly larger transverse strains, the change in feature angle is independent of cut geometry. (From: “Dynamic kirigami structures for integrated solar tracking.” Aaron Lamoureux, Kyusang Lee, Matthew Shlian, Stephen R. Forrest, & Max Shtein, *Nature Communications* **2015** – DOI: [10.1038/ncomms9092](https://doi.org/10.1038/ncomms9092), [20] partially funded by NSF 1240264 under the Emerging Frontiers in Research and Innovation (EFRI) program, as well as this grant)

## 7.5. Electric Organ of Eel

In the previous report, we proposed an architecture of an artificial analog of the electric organ of eel, reproduced below:

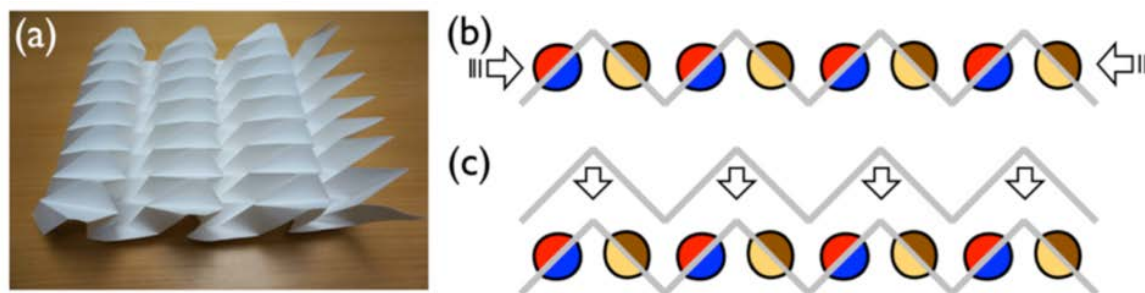
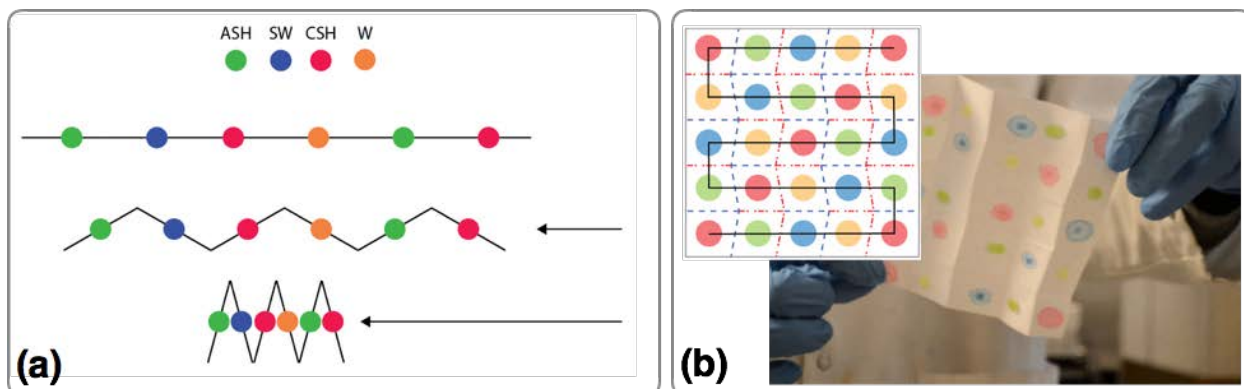


Figure 55 (a) example of a paper sheet folded in a modified *Miura ori* pattern that has one degree of freedom and a negative Poisson ratio (courtesy of collaborator Matthew Shlian). We are interested in exploring the use of this and similar shapes for the creation of massive arrays of charged droplets to realize artificial electric organs with superior discharge characteristics that match and exceed the response found in nature.

Subsequently, *Shtein* and *Mayer* labs collaborated to develop a variation on this concept and architecture, as shown below for a 1-dimensional array (**Fig. 75a**) and subsequently for a 2-dimensional array (**Fig. 75b**):



**Figure 75:** (a) 1-dimensional analog of electric organ of eel; ASH: anion selective hydrogel, SW: salt water, CSH: cation selective hydrogel, W: water. The total voltage produced in this configuration scales as  $n/4$ , where  $n$  is the number of folds in the structure. (b) 2-dimensional version of the pattern in (a) that uses the *Miura ori* fold to achieve  $n^2$  scaling of voltage due to the 2-dimensional nature of the pattern. The *Miura ori* folding pattern has 1 degree of freedom, allowing for all of the junctions to be formed (contacted) simultaneously.

The potential advantage of these structures relative to the earlier “string-of-pearls” architecture involving droplets is that the performance is no longer limited by the series resistance, that scales rapidly and linearly with the number and volume of droplets in a string. Instead, now

series resistance can be reduced by orders of magnitude by forming films of ion selective membranes and ion reservoirs, with multiple parallel connections between them formed through the substrate.

Initial iterations involved the use of conventional paper (not infrequently used as a separator material in batteries), but the water in the hydrogel wicked laterally through the paper, pulling moisture away from the surface of hydrogel and increasing its resistance at the surface. Wicking through the paper to make ionic contact was sub-optimal and poorly controlled. A hydrophobic marker was used to add a hydrophobic coating to confine the spread of moisture, and perforations were (manually) added to shut liquid through the substrate.



**Figure 76:** Manually perforated and patterned accordion fold pattern containing hydrogels. Despite patterning a hydrophobic rim around the hydrogel areas.

We subsequently used a laser cutter to create a denser array of smaller perforations, as shown in **Fig. 77**, which allowed for better control of coating of the perforations, with less hydrogel required for smaller perforations, which also allowed for thinner hydrogels.

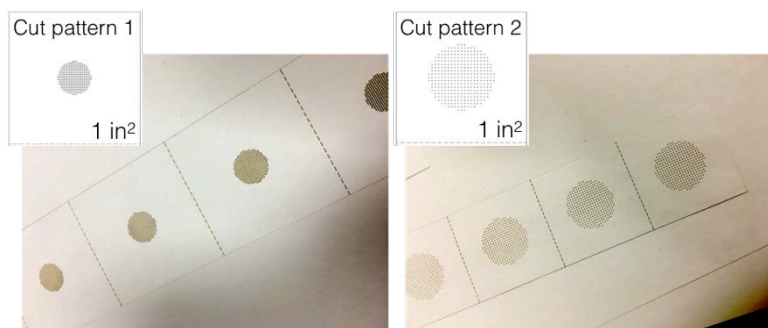


**Figure 77:** Laser-cut perforations in paper (accordion fold) at different perforation density.

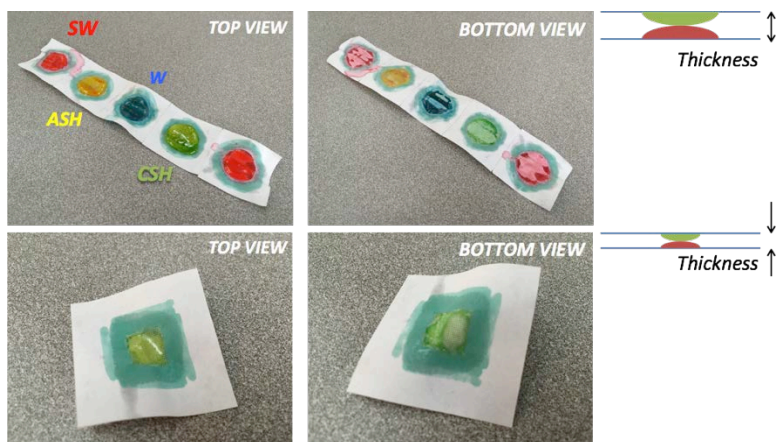


**Figure 78:** Hydrogels

Nevertheless, lateral spreading of moisture and drying of the hydrogel were still observed, due to wicking through the substrate. Using a hydrophobic substrate instead can prevent uncontrolled spreading of the aqueous solutions, yet permeable to allow for ionic communication between the components, and easily foldable to allow simultaneous contacting over a large scale / large number of junctions. We used Tyvek (commercially available hydrophobic, non-woven plastic) and made controlled perforations using a laser cutter for ion transport and for folding (**Fig. 79**).

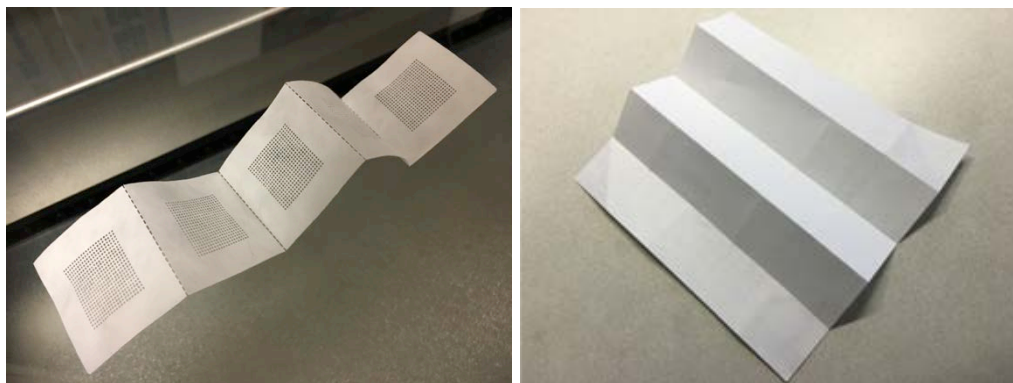


**Figure 79:** (left) accordion fold and (right) Miura ori fold using hydrophobic Tyvek, with laser-cut perforations (on the left) to control the amount of hydrogel used per junction.

## 7.6. Biomimetic phototropic and phototactic surfaces

As Lauder group and others has shown (see Figure MS6 from Wen, *et al.*, J. Exper. Biol. (2014) **217**, 1656), the skin of marine animals, here sharks, contains multi-scale features – “denticles” (**Fig. 80**)– that can modify the hydrodynamic drag, depending on the Reynolds number. These



and analogous constructs (e.g. “riblets”) have also been of interest for air vehicle applications, where modulation of drag could be used for improving flight performance and enable drag steering. Of interest to this project is the possibility of combining these surface structures with energy harvesting and stimulus-sensing capability to enable autonomic and distributed, stimulus-reactive behavior.

Having developed highly scalable kirigami structures whose periodicity can be controlled over a large range through global strain, as well as incorporation of solar energy harvesting capability with this form factor (Lamoureux, et al., Nature Comm. (2015) **6**, 8092), we began covering air foils with kirigami shapes cut from flexible polyimide foils (**Fig. 81**). When stretched over the air foil, despite being made from ~100 micrometer thick, flexible plastic, the kirigami sheets exhibit remarkable stability in the wind tunnel even beyond 10 m/s air speed. Furthermore, the drag coefficient,  $C_D$ , can be controlled by extent of global strain on the kirigami sheet in statistically significant and substantial ways (**Fig. 82**).

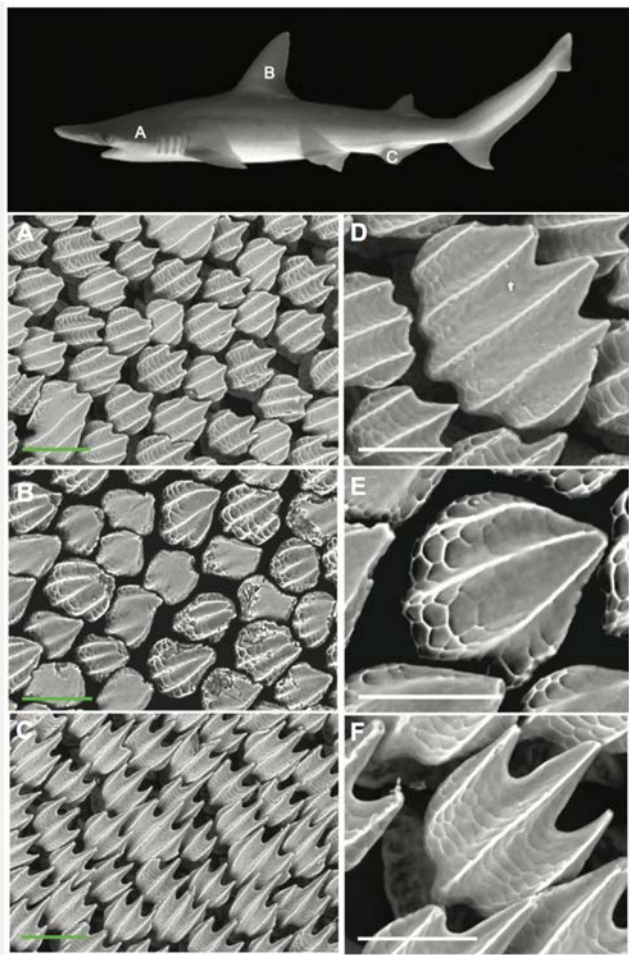
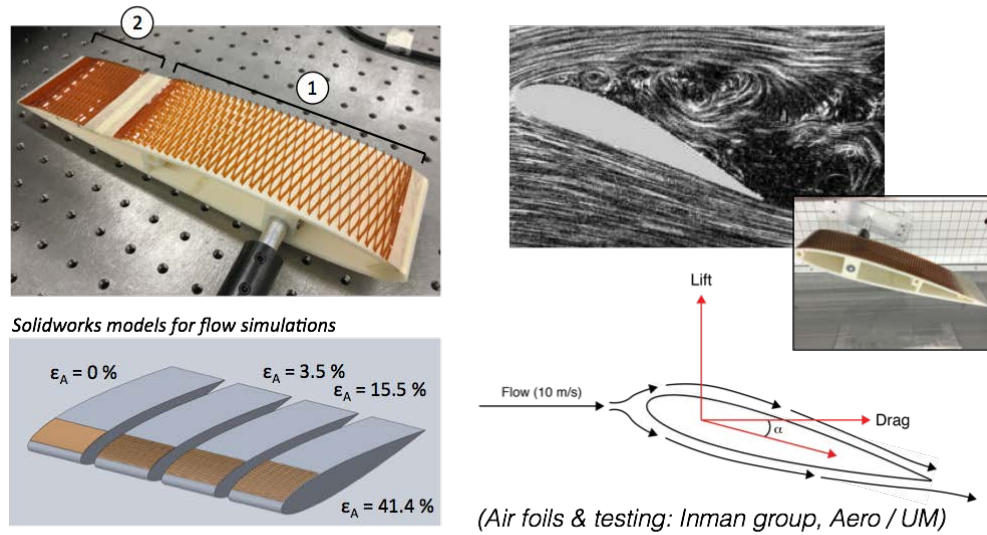


**Figure 80:** from Wen, et al., J. Exper. Biol. (2014) 217, 1656), the skin of marine animals, here sharks, contains multi-scale features – “denticles” – that can modify the hydrodynamic drag, depending on the Reynolds number

- 1) Leading edge – dynamic drag control enabling moment and drag steering
- 2) Trailing edge – static surface texture to minimize flow separation and decrease overall drag



**Measure lift and drag as a function of kirigami strain ( $\epsilon_A$ ) and angle of attack ( $\alpha$ )**

**Figure 81:** laser cut kirigami shapes stretched over an air foil, along the leading and trailing edges. The leading edge surface modification is expected to enable dynamic drag force control for drag steering, whereas the surface modification of the trailing edge can be used to reduce flow separation and, for some length scales and Reynolds numbers, reduce drag.

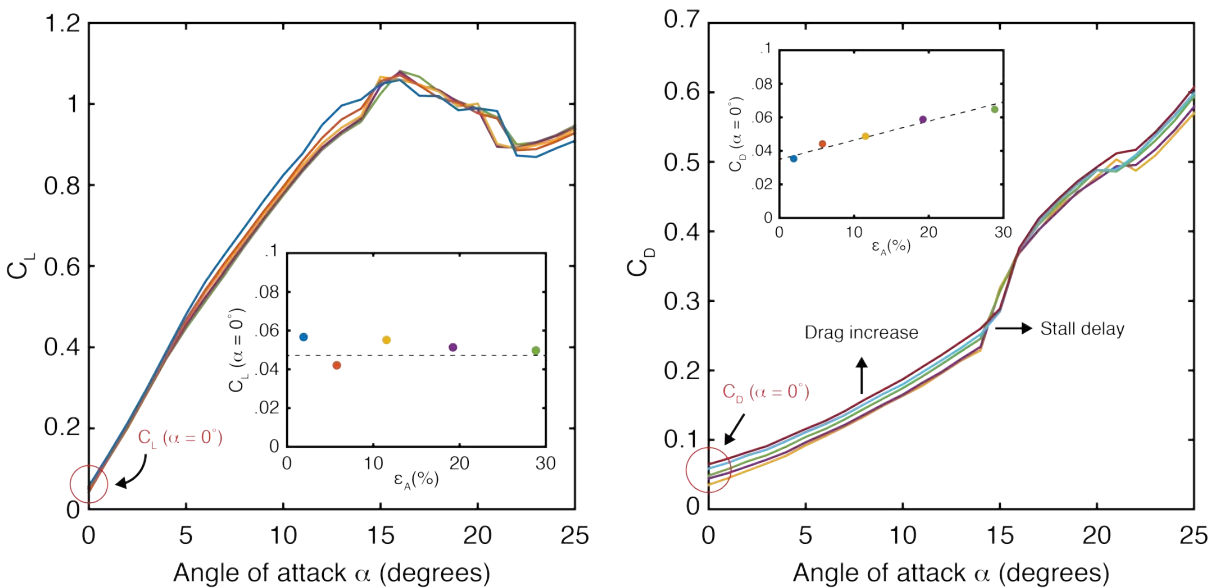


**Figure 82:** (left) Plot of the experimentally measured lift coefficient,  $C_L$ , as a function of the angle of attack for kirigami structures stretched over the air foil, showing that intrinsic lift is not modified at zero degrees. (right) Plot of the experimentally measured drag coefficient,  $C_D$ , as a function of angle of attack for the same structure, indicating that drag increases can be achieved as a function of kirigami strain, as well as delay of the stall condition. These findings indicate some of the most statistically significant modifications in  $C_D$  and  $C_L$  observed for surface modifications.

## 7.7. Circular kirigami-based springs & tunable antennas

We previously described a means of phototropic actuation of a kirigami shape:

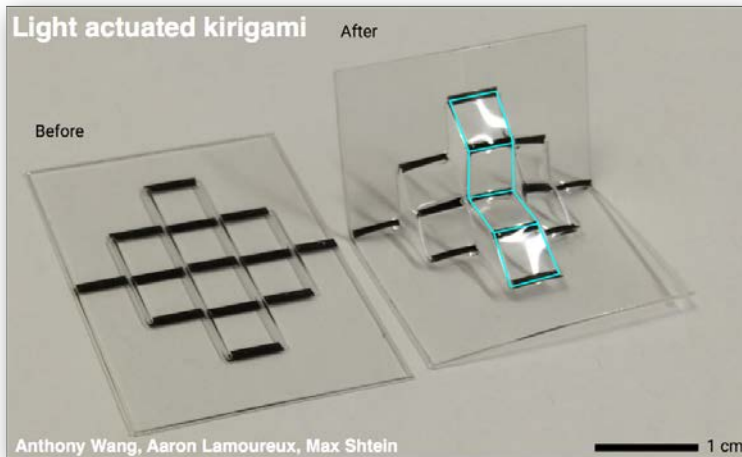


**Figure 83:** Photo-actuated kirigami, where the overall force and stroke are controlled through a combination of the absorber and kirigami patterns, and force multiplication is possible by engaging multiple light-triggered actuators in unison, analogous to actuation performed by muscle tissue.

We anticipated that these structures could be realized with different shapes and different functional properties, but all would depend on the geometric and mechanical properties for determining the spatial distribution of intrinsic material properties, which in turn program the auxetic behavior. We speculated that combining these actuations with functional surfaces, for example, can enable autonomic constructs relevant to the DoD / Air Force applications, such as in air vehicle-mounted antennas for communications and reconnaissance.

To address the antenna application, we developed a circular kirigami pattern that can be combined with photo- and electro-strictive materials to achieve beam forming, beam steering, gain and input impedance control *via* out-of-plane deformation. A schematic of the kirigami design is shown in **Figure 84a**, where the linear cut pattern is symmetric about a center axis (z-direction). The electrical pathway for the antenna is formed using a patterned conductive film – gold (Au) is shown in this example. This structure may be mounted to a coaxial cable to provide signal and ground as shown in **Figure 84b**. This deformation of this kirigami structure may be controlled as a function of out of plane deformation as shown in finite element models in **Figure 84c**. Additional work is currently underway using the experimental setup shown in **Fig. 84b**, including mechanical testing to determine the optimal materials for actuation, followed by electromagnetic testing in collaboration with the Grbic group in Electrical Engineering.

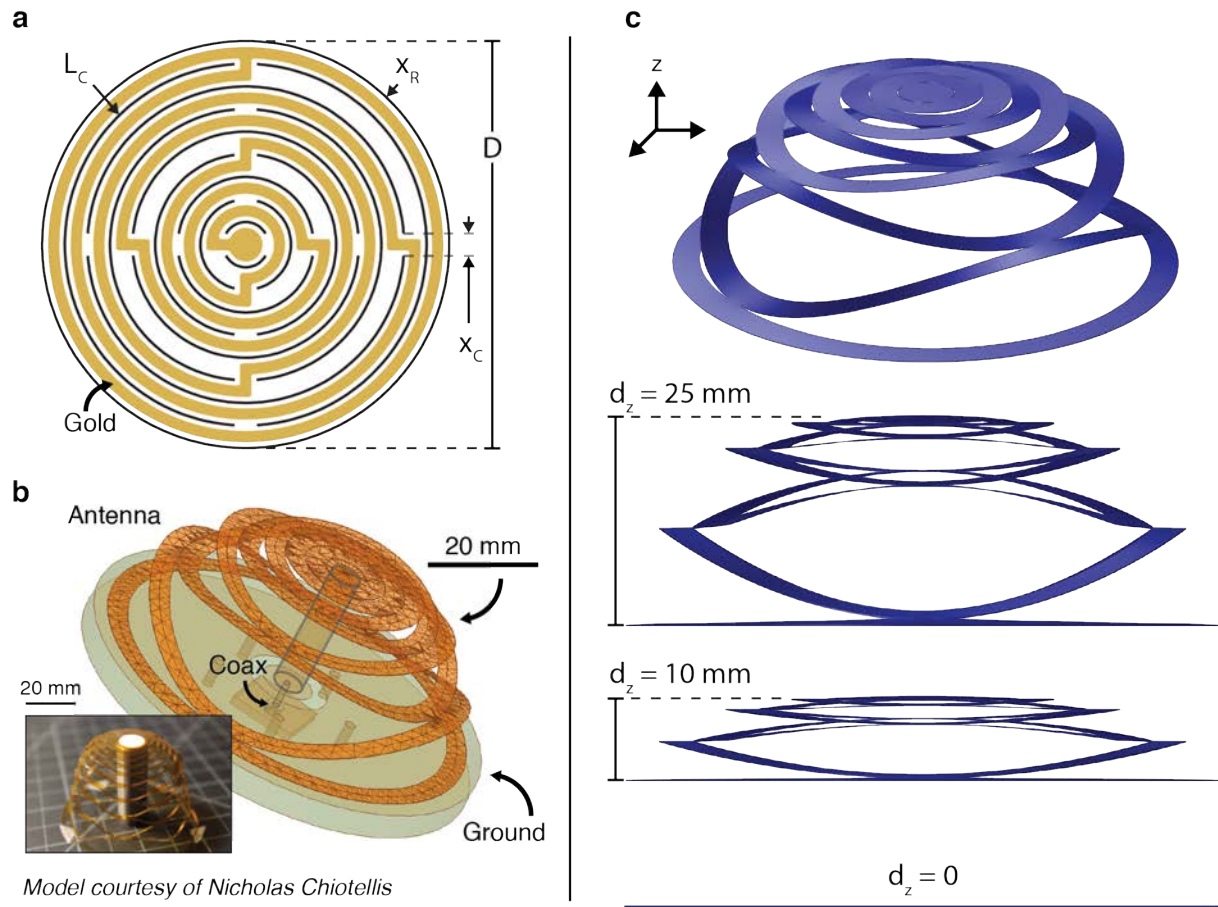


**Figure 84** (a) Schematic of antenna design, consisting of axially-symmetric linear pattern and electrical contacts. (b) Experimental setup to measure antenna response. Also shown is a prototype antenna made from Kapton® film. (c) COMSOL modeling of kirigami response, shown as a function of  $z$ -axis deflection (0 to 25 mm). [A. Lamoureux, PhD thesis 2017]

While work is underway to characterize the electromagnetic properties of the construct shown in **Fig. 84**, we potentially can generalize its auxetic behavior to other functional applications better, if we can predict its geometric response, regardless of the material from which it's made, and for an arbitrary cut structure.

The geometric and mechanical response of *linear* kirigami patterns is now much better understood, in large part due to our work on the topic, with beam theory applicable to these systems. However, predicting the cross-plane deformation behavior of a *circular* kirigami structure is considerably more difficult, as the evolving surface is highly contoured in multiple dimensions. In one approach, we examined the behavior of the circular kirigami pattern shown in **Fig. 85**, recognizing that this surface behaves as a spring. In our first order analysis, we analyzed the relationship between the cross-plane force and cross-plane deflection ( $d_z$ ) as that of a spring, characterized by a spring constant,  $k^{total}$ . We analyzed and tested a number of



samples, arriving at an empirically tested, predictive model for how  $k^{total}$  depends on the geometry of the cuts, as defined in **Fig. 85**, and the intrinsic properties of the material from which the sheet is made.

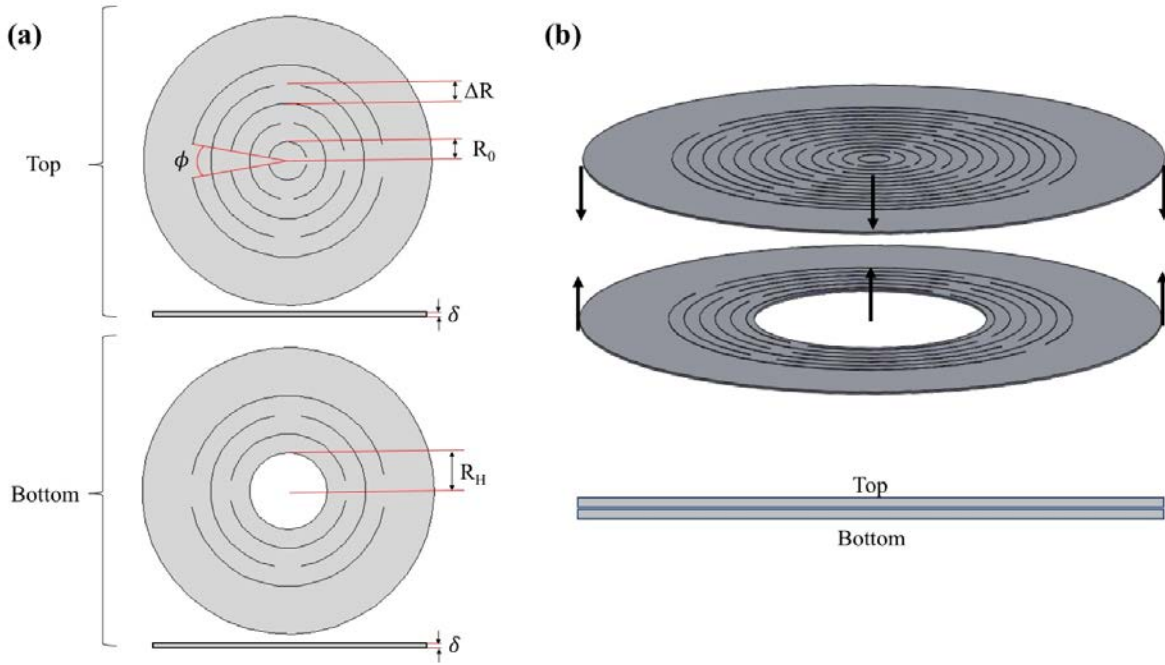


**Figure 85: Kirigami pattern geometry and assembly.** (a) The geometric parameters that define both kirigami patterns are inner radius ( $R_0$ ), radial spacing ( $\Delta R$ ), angular spacing ( $\phi$ ), and thickness ( $\delta$ ). In the case of the bottom pattern, the one additional parameter is the hole radius ( $R_H$ ). The top and bottom patterns are identical, apart from the central hole in the bottom pattern. (b) The patterns are placed one on top of the other with the pattern with the hole on the bottom.

Treating each “ring” of the circular kirigami pattern as multiple leaf springs connected in parallel, and adding up the behavior of the concentric rings of varying radius  $r$ , we obtain the predictive relation between the applied cross-plane force and cross-plane deflection, viz a vis  $F = -k \cdot d_z$ :

$$k^{total} = \frac{1}{\sum_{i=1}^n \frac{1}{2B \left( J_A + \frac{B}{G} J_B \right)}} \quad (\text{Eq. 1})$$

Where

$$J_A = \int_0^L \left( -y \frac{-dy/dx}{\sqrt{1 + \left(\frac{dy}{dx}\right)^2}} - (r-x) \frac{1}{\sqrt{1 + \left(\frac{dy}{dx}\right)^2}} \right)^2 ds$$

$$J_B = \int_0^L \left( y \frac{1}{\sqrt{1 + \left(\frac{dy}{dx}\right)^2}} - (r-x) \frac{-dy/dx}{\sqrt{1 + \left(\frac{dy}{dx}\right)^2}} \right)^2 ds$$

(Eqs. 2 & 3)

and variables  $x$  and  $y$  are parametrized for a circular geometry:

$$x = r \cos(t) \quad y = r \sin(t) \quad (\text{Eqs. 4 \& 5})$$

Mechanical testing initially consisted of clamping the circular kirigami shape at its perimeter and suspending weights from the center, as shown in **Fig. 86**. Force was simply that given by the suspended weight, with deflection visually indicated.

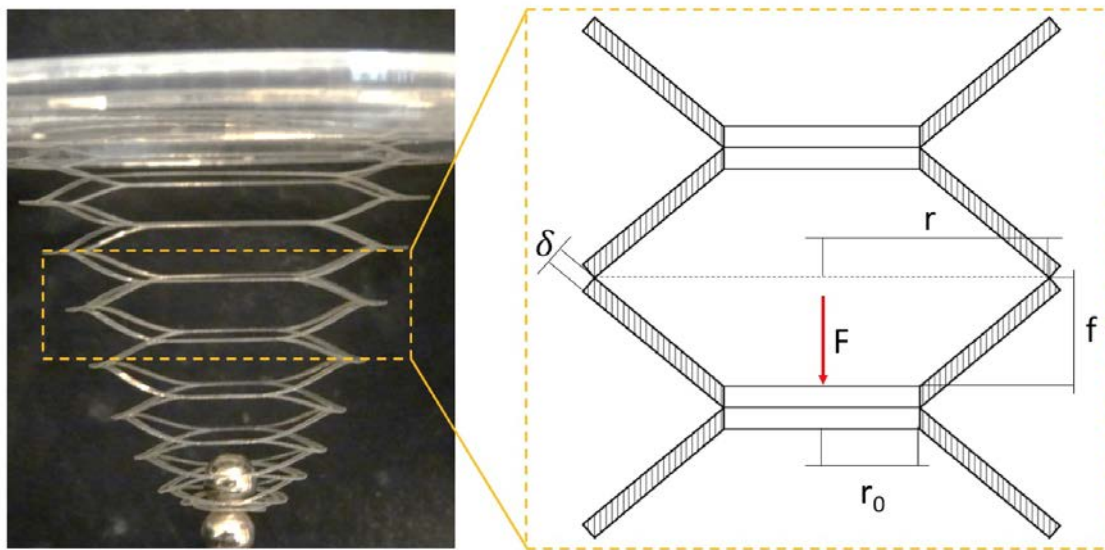


**Fig. 86: Photo & diagram of connected spring system resulting from circular kirigami pattern.** The spring system can be represented by a simplified geometry, pictured from the side after a cross-plane deflection (left panel). The parameters that define the spring behavior of the kirigami pattern are the inner radius ( $r_0$ ), outer radius ( $r$ ), thickness ( $\delta$ ), force ( $F$ ), and deflection ( $f$ ), as indicated (right panel).

We tested a total of 10 pairs of kirigami patterns, with the thickness of the sheet varying as a function of the radius by stacking two circular kirigami disks, one of which had a cutout. The cutout radius was varied from 0 to 23 mm, as shown in **Fig. 87**.

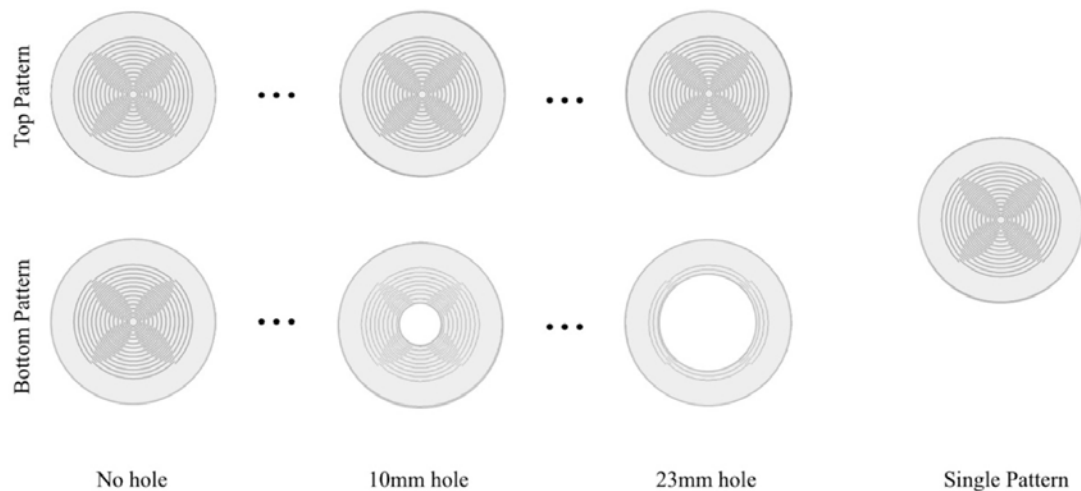


**Figure 87: Patterns tested.** There were ten pairs of patterns tested in total, three of which are shown here. The top pattern was identical in each case, while the bottom patterns differed only in the size of their central hole. Additionally, a single pattern with no hole was tested alone.

The resulting data, processed to show the effective spring constant (averaged over multiple samples), are shown in **Fig. 88**, with the prediction of *Eq. (1)* plotted as a solid line, using physical property values for the sheet material:  $E = 3.7 \text{ GPa}$ ,  $G_0 = 2.0 \text{ GPa}$ , and  $\delta = 0.10 \text{ mm}$ , and offsetting the theoretical model up by 0.8 due to clamping constraints. Deviations between the prediction and measurements are currently attributed to non-linear behavior for larger deflections obtained with larger hole radii.

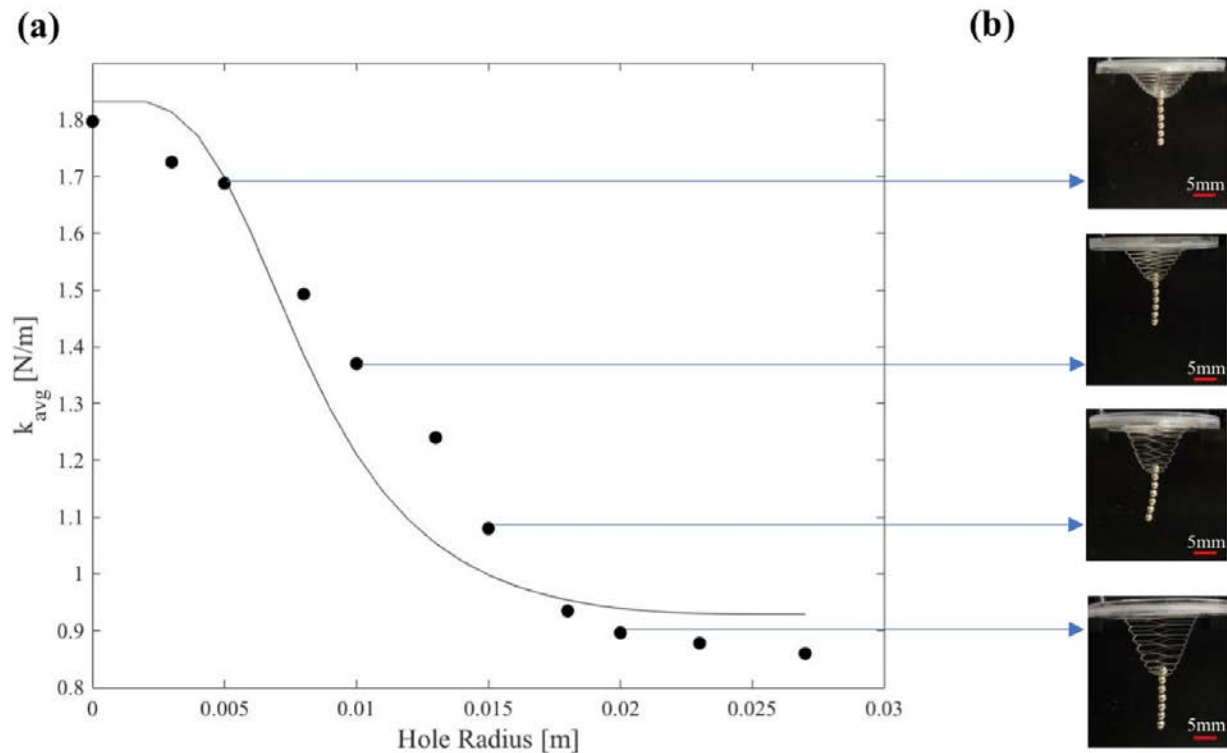


**Figure 88: Spring behavior of kirigami patterns.** (a) Average spring constant ( $k_{avg}$ ) versus hole radius ( $R_H$ ). The data exhibit a negative logistic trend. (b) Each pair of kirigami patterns was weighted in the center using ball-bearing magnets. The deflection from the equilibrium position was measured for each pair of patterns using five, six, and seven ball bearings, and the average spring constant for these three measurements was calculated.

## 7.8. Significance and follow-on work:

These findings are significant in several ways.

- 1) The simple circular kirigami structure examined above can in principle map to any curved surface element, obtainable from a planar starting sheet. This is important for producing complex 3-dimensional shapes even from membranes that are non-stretchy intrinsically. This opens the possibility of designing biomimetic, morphing structures from organic and inorganic, engineered materials regardless of their tensile strength.
- 2) The beam theory-based analysis of circular leaf springs can be extended (performed by our group but not shown here) to elliptical shapes, further broadening the gamut of surface curvatures that can be reproduced using a collection of in-lane cuts.
- 3) The predictive model we developed allows for subsequent multi-functional design *in silico* of dynamically tuned antennas and other structures by mapping material properties such as complex refractive indexes, mass, hardness, permeability, etc. to the geometry,

to predict the co-dependence of mechanical and other properties.

- 4) The manner in which 2-dimensional membranes are evolved into 3-dimensional shapes using the kirigami construct involves varying the size of the openings between sheet elements. When implemented in extremely thin sheets on a micro- or nano-scopic scale, this allows for controllably varying the permeability of the membrane. One application is in engineering the relationship between mechanical properties and permeability that mimics that of *archaea* lipid-based membranes. Another application is in autonomously regulating filters or dams for transport of chemical signals or nutrients in flows (e.g. in implantable devices).

We are in the process of writing a manuscript and a patent application based on these findings and applications.

## **8. Suported personnel**

Geoffray Leriche, PhD, Synthetic Organic Chemistry, Postdoctoral fellow

Young-Hun Kim, Materials Science and Engineering, Ph.D. student

Takaoki Koyanagi, Synthetic Organic Chemistry, Ph.D. student

Valentina Paolucci, Physical Chemistry, Visiting Ph.D. student from the University of Copenhagen

Aziz Fennouri, Ph.D., Nanotechnology, Postdoctoral fellow

Thomas Schroeder, Chemical Engineering, Ph.D. student

Anirvan Guha, Physics, Ph.D. student

Jonathan List, Ph.D., Physics, Postdoctoral fellow

Karthik Diraviyam, Biomedical Engineering, Postdoctoral Fellow

Hoon Sim, Biomedical Engineering, Postdoctoral Fellow

Kanika Agrawal, Materials Science and Engineering, Ph.D. student

Matthew E. Sykes, Materials Science and Engineering, Ph.D. student

Aaron Lamoureux, Materials Science and Engineering, PH.D. student

Olga Shalev, Materials Science and Engineering, PH.D. student

Siddharth Borsadia, PH.D. student

Anthony Wang, Materials Science and Engineering, undergraduate student

Kevin Greenman, undergraduate student

Carlos Sastre, undergraduate student

## 9. Collaborations

Differential Scanning Calorimetry (DSC) measurements are necessary to measure the liquid - crystalline phase transitions temperature of each synthetic lipid. Since DSC measurements are not directly available in the grant's network, we started a collaboration with **Prof. Gregory Holland** at San Diego State University (Department of Chemistry and Biochemistry) in 2014. We are still collaborating with **Prof. Gregory Holland** for DSC measurements but also for  $^2\text{H}$  NMR spectroscopy. These NMR studies should help us to determine the conformation of our bipolar phospholipids in membranes.

We are still collaborating with **Prof. Mu-Ping Nieh** at University of Connecticut to study lipid exchange of membrane spanning lipids using bicelles. In 2016, we sent two lipids **U16** and **T32** to get initial data and know whether bipolar lipids form bicelles. We are currently in a process of synthesizing more lipids in order to confirm the preliminary results.

The use of the regenHU BioFactory 3D bioprinter for the printing of gel battery systems was made possible by a collaboration with **Prof. Barbara Rothen-Rutishauser** and **Prof. Alke Fink** at the Adolphe Merkle Institute.

**Daniel Inman Group** (UM Aerospace) – air foil testing in the wind tunnel

**Stephen Forrest Group** (UM Electrical Engineering) – GaAs solar cell integration with kirigami substrates

**Jinsang Kim Group** (UM Materials Science and Engineering) – chemiluminescent molecule design

**Anthony Grbic Group** (UM Electrical Engineering) – antenna applications of circular and other kirigami patterns

**Greg Amidon Group** (UM Pharmacology) – dissolution kinetics of small molecular organic compounds

**Geeta Mehta Group** (UM MSE / BME) – bioavailability and transport across cell membranes of small molecular organic compounds

**Anna Schwendeman Group** (UM Pharmacology) – bioavailability of small molecular organic compounds

**Roy Clarke** (UM Physics) – structural characterization of patterned small molecular organic films

## 10. Publications

1. Agrawal, K. L., M. E. Sykes, K. H. An, B. Frieberg, P. F. Green, and M. Shtein. 2013. Influence of exciton lifetime on charge carrier dynamics in an organic heterostructure. *Appl Phys Lett* 102.
2. Majd, S., E. C. Yusko, J. Yang, D. Sept, and M. Mayer. 2013. A Model for the Interfacial Kinetics of Phospholipase D Activity on Long-Chain Lipids. *Biophys J* 105:146-153.
3. Mayer, M., and J. Yang. 2013. Engineered Ion Channels as Emerging Tools for Chemical Biology. *Accounts Chem Res* 46:2998-3008.
4. Agrawal, K. L., and M. Shtein. 2014. Self-powered ion detectors based on dye-sensitized photovoltaics. *Nanoscale* 6:11019-11023.
5. Thompson, M. P., L. M. Randolph, C. R. James, A. N. Davalos, M. E. Hahn, and N. C. Gianneschi. 2014. Labelling polymers and micellar nanoparticles via initiation, propagation and termination with ROMP. *Polym Chem-Uk* 5:1954-1964.
6. Bell, N. C., S. J. Doyle, G. Battistelli, C. L. M. LeGuyader, M. P. Thompson, A. M. Poe, A. Rheingold, C. Moore, M. Montalti, S. Thayumanavan, M. J. Tauber, and N. C. Gianneschi. 2015. Dye Encapsulation in Polynorbornene Micelles. *Langmuir* 31:9707-9717.
7. Cole, C. M., R. J. Brea, Y. H. Kim, M. D. Hardy, J. Yang, and N. K. Devaraj. 2015. Spontaneous Reconstitution of Functional Transmembrane Proteins During Bioorthogonal Phospholipid Membrane Synthesis. *Angew Chem Int Edit* 54:12738-12742.
8. Horger, K. S., H. Y. Liu, D. K. Rao, S. Shulda, D. Sept, S. V. Ambudkar, and M. Mayer. 2015. Hydrogel-assisted functional reconstitution of human P-glycoprotein (ABCB1) in giant liposomes. *Bba-Biomembranes* 1848:643-653.
9. Lamoureux, A., K. Lee, M. Shlian, S. R. Forrest, and M. Shtein. 2015. Dynamic kirigami structures for integrated solar tracking. *Nat Commun* 6.
10. Shyu, T. C., P. F. Damasceno, P. M. Dodd, A. Lamoureux, L. Z. Xu, M. Shlian, M. Shtein, S. C. Glotzer, and N. A. Kotov. 2015. A kirigami approach to engineering elasticity in nanocomposites through patterned defects. *Nat Mater* 14:785-+.
11. Koyanagi, T., G. Leriche, D. Onofrei, G. P. Holland, M. Mayer, and J. Yang. 2016. Cyclohexane Rings Reduce Membrane Permeability to Small Ions in Archaea-Inspired Tetraether Lipids. *Angew Chem Int Edit* 55:1890-1893.
12. Koyanagi, T., G. Leriche, A. Yep, D. Onofrei, G. P. Holland, M. Mayer, and J. Yang. 2016. Effect of Headgroups on Small-Ion Permeability across Archaea-Inspired Tetraether Lipid Membranes. *Chem-Eur J* 22:8074-8077.



13. Lee, K., C. W. Chien, B. Lee, A. Lamoureux, M. Shlian, M. Shtein, P. C. Ku, and S. Forrest. 2016. Origami Solar-Tracking Concentrator Array for Planar Photovoltaics. *Acs Photonics* 3:2134-2140.
14. Schroeder, T. B. H., G. Leriche, T. Koyanagi, M. A. Johnson, K. N. Haengel, O. M. Eggenberger, C. L. Wang, Y. H. Kim, K. Diraviyam, D. Sept, J. Yang, and M. Mayer. 2016. Effects of Lipid Tethering in Extremophile-Inspired Membranes on H<sup>+</sup>/OH<sup>-</sup> Flux at Room Temperature. *Biophys J* 110:2430-2440.
15. Veccharelli, K. M., V. K. Tong, J. L. Young, J. Yang, and N. C. Gianneschi. 2016. Dual responsive polymeric nanoparticles prepared by direct functionalization of polylactic acid-based polymers via graft-from ring opening metathesis polymerization. *Chem Commun* 52:567-570.
16. Fennouri, A., S. F. Mayer, T. B. H. Schroeder, and M. Mayer. 2017. Single channel planar lipid bilayer recordings of the melittin variant MelP5. *Bba-Biomembranes* 1859:2051-2057.
17. Koyanagi, T., K. J. Cao, G. Leriche, D. Onofrei, G. P. Holland, M. Mayer, D. Sept, and J. Yang. 2017. Hybrid Lipids Inspired by Extremophiles and Eukaryotes Afford Serum-Stable Membranes with Low Leakage. *Chem-Eur J* 23:6757-6762.
18. Lee, J., Y. H. Kim, F. T. Arce, A. L. Gillman, H. Jang, B. L. Kagan, R. Nussinov, J. Yang, and R. Lal. 2017. Amyloid beta Ion Channels in a Membrane Comprising Brain Total Lipid Extracts. *Acs Chem Neurosci* 8:1348-1357.
19. Leriche, G., J. L. Cifelli, K. C. Sibucão, J. P. Patterson, T. Koyanagi, N. C. Gianneschi, and J. Yang. 2017. Characterization of drug encapsulation and retention in archaea-inspired tetraether liposomes. *Org Biomol Chem* 15.
20. Paolucci, V., G. Leriche, T. Koyanagi, and J. Yang. 2017. Evaluation of tetraether lipid-based liposomal carriers for encapsulation and retention of nucleoside-based drugs. *Bioorg Med Chem Lett* 27:4319-4322.
21. Schroeder, T. B. H., A. Guha, A. Lamoureux, G. VanRenterghem, D. Sept, M. Shtein, J. Yang, and M. Mayer. 2017. An electric-eel-inspired soft power source from stacked hydrogels. *Nature* 552:214-218.
22. Shalev, O., S. Raghavan, M. Mazzara, N. Senabulya, P. D. Sinko, E. Fleck, C. Rockwell, N. Simopoulos, C. M. Jones, A. Schwendeman, G. Mehta, R. Clarke, G. E. Amidon, and M. Shtein. 2017. Printing of small molecular medicines from the vapor phase. *Nat Commun* 8.
23. Yusko, E. C., B. R. Bruhn, O. M. Eggenberger, J. Houghtaling, R. C. Rollings, N. C. Walsh, S. Nandivada, M. Pindrus, A. R. Hall, D. Sept, J. L. Li, D. S. Kalonia, and M. Mayer. 2017. Real-time shape approximation and fingerprinting of single proteins using a

nanopore. Nat Nanotechnol 12:360-367.

24. Schroeder, T. B. H., J. Houghtaling, B. D. Wilts, and M. Mayer. 2018. It's not a bug, it's a feature: Functional materials in insects. Adv. Mater. In press.